Root Water Uptake –

Exploring the Role of Root System Architecture and Root-Soil
Interactions with X-ray Computed Tomography

Dissertation

zur Erlangung des

Doktorgrades der Agrarwissenschaften (Dr. agr.)

der

Naturwissenschaftlichen Fakultät III

Agrar- und Ernährungswissenschaften,

Geowissenschaften und Informatik

der Martin-Luther-Universität Halle-Wittenberg

vorgelegt von

Herrn Dipl.-Biol. Koebernick, Nicolai

Geb. am 25.09.1978 in Wuppertal

Table of contents

1 Introduction

1.1 Root system architecture and plant uptake capacity

About 850 million people are presently undernourished and feeding an estimated additional 2.3 billion people by 2050 will require an increase of global food production by 70 % (FAO 2009, FAO 2012). While modern agriculture has been very successful in increasing crop yields, it has done so by dramatically increasing the input of fertilizer, pesticides, and water. Current agricultural practices produce extensive environmental damage, contributing to the degradation of land, pollution, and the overuse of resources - agriculture accounts for 85 % of global freshwater use (Foley et al., 2005).

Considering the growing scarcity of resources, it will be a central challenge for agriculture to increase crop production while simultaneously reducing resource input and minimizing environmental damage (Tilman et al. 2011). The need to enhance the efficiency of resource acquisition of agroecosystems has brought increasing attention to the "hidden half" (Eshel and Beeckman, 2013) of plants, the root system, which is the main site of resource capture (Lynch, 1995; Lynch, 2007; Pierret et al., 2007; White et al., 2013).

Root system architecture

The plant root system is adapted for the efficient foraging for water and nutrients in soil. Supplies of these resources are often limited and variable in both space and time. Strong gradients of nutrient and water availability commonly occur with soil depth in the field. These gradients often present conflicting limitations to plant productivity. For example, nutrient supply is usually higher in topsoil but water content is lower and more variable over time in topsoil than in subsoil. The efficiency of nutrient and water uptake is therefore largely determined by the spatial and temporal configuration of the root system, or root system architecture (RSA). RSA describes the spatial distribution of roots in soil, commonly represented by root biomass or length as a function of soil depth, and the connection of individual root axes to each other, i.e. the topology of the root system. RSA is very complex (Figure 1.1) and highly variable in time, as root growth, branching, and eventually root senescence constantly change the configuration of the root system. This results from the interplay of an intrinsic genetic program and a plethora of external biotic and abiotic constraints. RSA therefore differs between plant species and genotypes, but there is also considerable variability within plant genotypes grown under different environmental conditions, or even within a single root system (Lynch, 1995). RSA is affected by soil compaction, macroporosity, nutrient and water status,

soil aeration, temperature, and plant developmental status. In addition, root activity strongly affects the structure and the physical and chemical properties of the soil in their vicinity, the rhizosphere (Hinsinger et al., 2009).
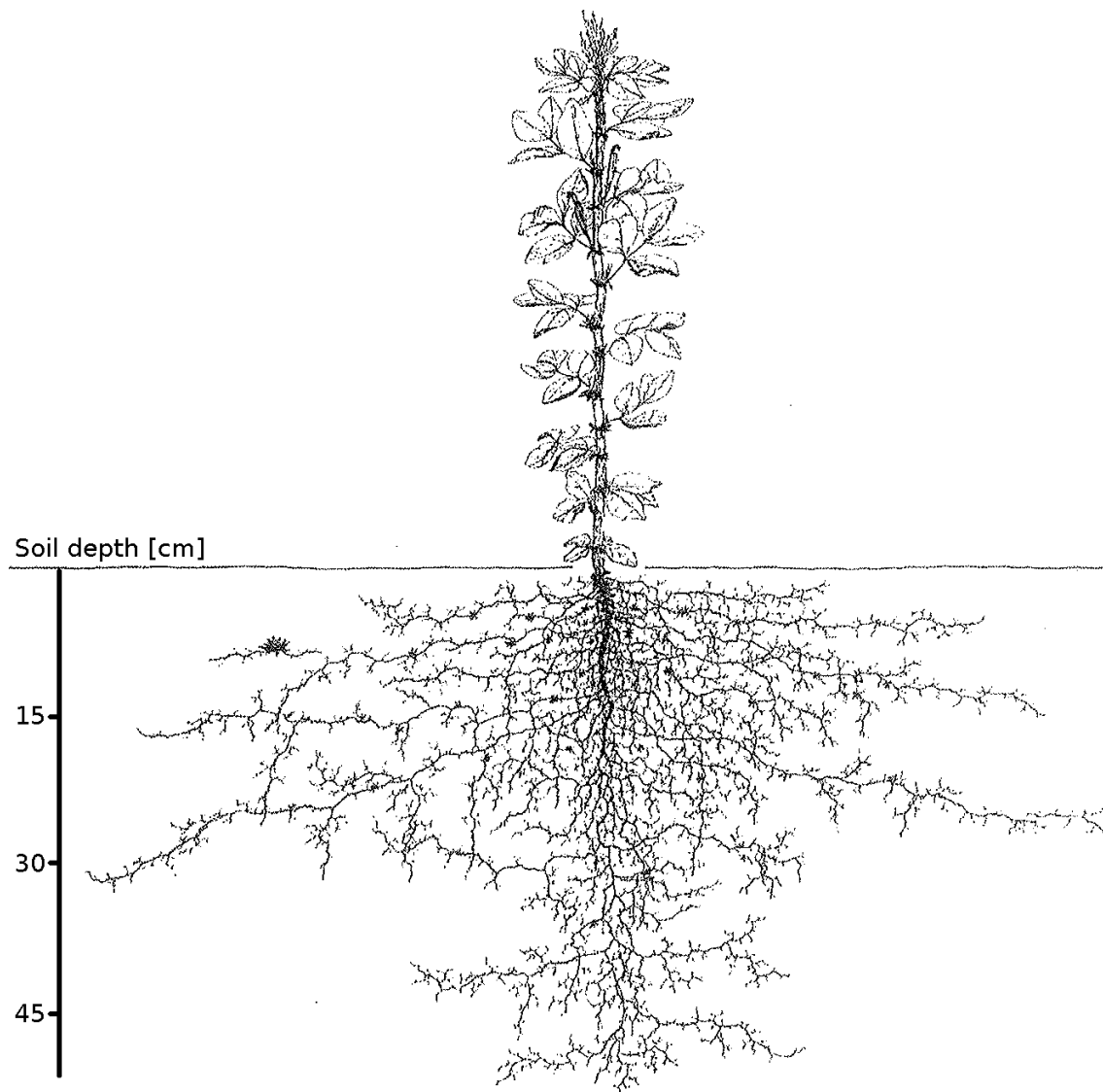
Figure 1.1: Drawing of the root system architecture of Vicia faba L., modified from Kutschera et al. (2009)

Root functional heterogeneity

The architecture of roots is inherently linked to root function. Individual roots may be very different in size, anatomy and function, as Pregitzer put it: "A root is not necessarily a root" (Pregitzer, 2002). Roots can be classified into different root orders or types depending on their origin. In dicots, there is typically a taproot originating from the radicle of the seed. First order lateral roots branch from the taproot and higher order lateral roots may branch from lateral roots. These different root orders are associated with different functions (Pierret et al., 2007). Variations in root properties are also prevalent along individual roots. As root tissues mature and

differentiate, they change the physiological status of the root. For example, older roots with fully differentiated xylem conduits have a much higher hydraulic conductivity in the axial direction than younger roots. Thus, they provide the hydraulic connection to the shoot. In contrast, the endodermis (in some species also the exodermis) of older roots may develop suberin lamellae in its cell walls, greatly reducing the hydraulic conductivity in the radial direction, effectively isolating the root from the soil (Enstone et al., 2002).

Finally, roots show a range of plastic responses to changes in their environment. Root plasticity is an important strategy for the optimization of resource use (White et al., 2013). For example, the development of root cortical aerenchyma can be triggered by low nutrient availability which results in lower root respiration, thus reducing the metabolic costs of soil exploration (Fan et al., 2003). To conclude this section, RSA is highly variable in space and time. It determines the ability of a plant to explore different regions of soil and to respond dynamically to the localized and temporally changing accessibility of soil resources.

1.2   Plant water uptake

The soil-plant atmosphere continuum

Water scarcity is a major limitation to crop production. About one third of the earth's land surface is arid and periodic drought affects agricultural production almost universally (Lynch, 1995). Most of the water used in agriculture is taken up by plants and transpired to the atmosphere. The development of sustainable water management practices requires a better understanding of the underlying processes and the complex biophysical dynamics of root water uptake (Green et al., 2006).
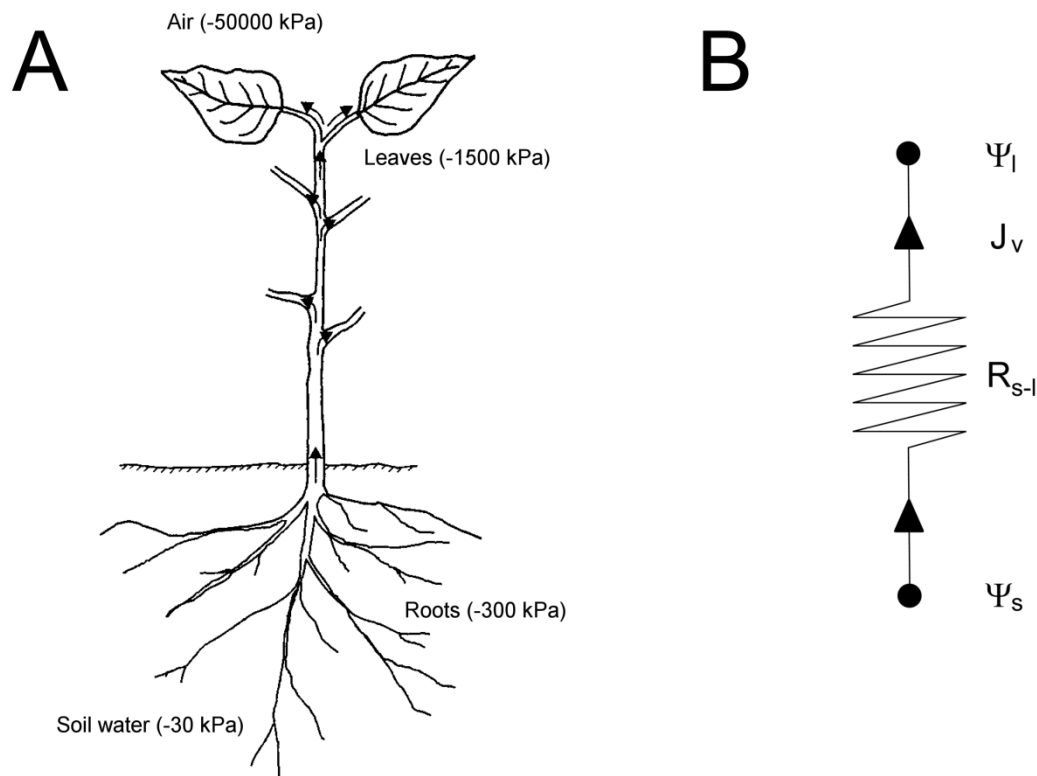
Figure 1.2: The soil-plant-atmosphere continuum. A) Typical distribution of water potential in the different components of the SPAC. Modified from Hillel (1998) B) Simplified drawing of the Ohm's law analogy to water movement in plants. Water flow is described by Equation 1.1

Plants need water as an active reactant, as a solvent, and to maintain turgor. Most of the water taken up by plants is just on transit and is transpired to the atmosphere via the stomatal cavities in their leaves. Transpiration is a necessary ecological trade-off for carbon gain from the atmosphere and it is the driving force of plant water uptake. The general consensus is that plant water movement is driven by the cohesion-tension mechanism, established by Böhm (1893). When a plant transpires, gradients in water potential are established. This causes an inflow of water from soil into the roots and to the leaves, where it is transpired to the atmosphere. Water flows thermodynamically 'downhill' towards increasingly negative water potentials (Figure 1.2A). The different components along the

pathway of water can be integrated when water movement is viewed as a catenary process (Gradmann 1928; van den Honert, 1948). This leads to the concept of the soil-plant-atmosphere continuum (SPAC). Water movement within the SPAC can be illustrated analogous to an electrical current (Ohm's law analogy, Figure 1.2B). Under steady-state conditions the same volume of water per time flows successively across the different components of the SPAC. Transport is governed by the gradient of water potential and the resistance to water flow within the system. Steady-state flow in the SPAC can be calculated using a simplified "black-box" resistance model (Zhuang et al., 2014):

$$J_v(t) = \frac{\psi_s(t) - \psi_l(t)}{R_{s-l}(t)}$$

(1.1)

where $J_v(t)$ is the volume flux density [$L^3\,L^{-2}\,T^{-1}$], $\psi_s(t)$ and $\psi_l(t)$ [P] are the water potentials in the soil and the leaves, respectively, and $R_{s-l}(t)$ [$M\,L^{-4}\,T^{-1}$] are the hydraulic resistances between soil and leaves. The physical nature of water flow in the different components of the SPAC is very different. For a mechanistic description it is therefore useful to isolate some components of the SPAC. The present thesis will focus on water relations of roots and soil, while the aboveground processes will be regarded as a black box.

Water movement in soil

The vast majority of terrestrial plants take up water from the unsaturated zone of soil, which is known as the vadose zone. The vadose zone is characterized by a high variability in water content, because it is closely coupled to the atmosphere through rainfall and evapotranspiration. Water movement in soil results from differences in total soil water potential (ψ_T), which is defined as:

$$\psi_T = \psi_m + \psi_o + \psi_p + \psi_z$$

(1.2)

where ψ_m is soil matric potential, ψ_o is the osmotic potential, ψ_p is the pressure potential, and ψ_z is the gravitational potential. In the absence of high solute concentrations, osmotic potential is usually neglected. Soil matric potential is the result of combined adhesive and capillary forces and binds water to the pore space of soils. The pressure potential is the hydrostatic pressure that is exerted by water saturating the soil above a point of interest. In saturated soil ψ_m is zero and ψ_p is positive, whereas in unsaturated soil ψ_p is zero and ψ_m is negative. The gravitational

potential is determined by the elevation of a point of interest relative to an arbitrary reference point. Soil matric potential is related to soil water content by the soil water retention curve, which depends on the pore size distribution and is characteristic for different soil types. At the scale of root systems and individual roots, water movement in unsaturated soil is described by the Richards' equation (Eq. 1.3), which states:

$$\frac{\partial \theta}{\partial t} = \nabla \cdot [K(\psi)\nabla\psi] + \frac{\partial K(\psi)}{\partial z} + S(x, y, z, t) \tag{1.3}$$

where θ [L^3 L^{-3}] is the volumetric water content of the soil, t [T] is time, K [L T^{-1}] the soil hydraulic conductivity, ψ [P] the soil matric potential, S [L^3 T^{-1}] is the sink term representing root water uptake, x and y [L] are the horizontal spatial dimensions, respectively, and z [L] is elevation.

Water movement in plant roots

Water movement from the soil into plant roots is caused by the water potential gradient between soil and roots. The rate of water movement depends on the size of the gradient and the hydraulic conductivity of the roots. The conductivity of roots can be considered in terms of two components, radial conductivity to water flow across the root cortex from the root-soil interface to the xylem, and axial conductance to water flow within the xylem up towards the shoot. These can be defined as:

$$J_h(z) = -K_h \frac{d\psi_x(z)}{dz} \tag{1.4}$$

$$J_r(z) = L_r[\psi_s(z) - \psi_x(z)] \tag{1.5}$$

where $J_h(z)$ [L^3 T^{-1}] is the axial flux up the xylem at distance z [L] from the apex, $J_r(z)$ [L T^{-1}] is the flux from the soil into the root per unit area, K_h [L T^{-1} P^{-1}] is the axial hydraulic conductance, L_r [L T^{-1} P^{-1}] is the radial hydraulic conductivity, $\psi_s(z)$ [P] is the water potential in the soil, and $\psi_x(z)$ [P] is the xylem water potential (Doussan et al., 1998a). Radial flow can occur along different parallel pathways, the apoplastic pathway along cell walls and intercellular spaces, and the cell-to-cell pathway, where water moves across cell membranes (Steudle, 2000). In the presence of pressure gradients, water movement will largely occur along the apoplastic pathway. At the endodermis, the apoplastic pathway is interrupted by Casparian

6

bands, so that at this layer water has to follow the cell-to-cell pathway. The axial component is characterized by a low resistance (or a high conductance) to water flow, which is - in flowering plants - accomplished by the joining of tracheary vessel elements through the loss of the protoplast and the removal of end walls between axially adjacent cells. According to Poiseuille's law, the hydraulic resistance of a xylem vessel is largely determined by its radius. Axial resistance is generally much lower than the radial resistance. It is therefore usually assumed that the latter is limiting the rate of root water uptake. The profile of water uptake along a root is not uniform and depends on the relative magnitudes of axial and radial resistances (Landsberg and Fowkes, 1978; Zwieniecki et al., 2002). There has been an extensive debate, whether root water uptake is limited solely by root hydraulic resistance, or if the resistance of the soil is a major constraint for root water uptake. The answer depends on the water status of the soil. Soil hydraulic resistance has little influence on root water uptake when the soil is wet, but it has a large influence when the soil is dry (Passioura, 1980). The situation is less clear in intermediate or heterogeneous situations, which are however very likely to occur in the field (Draye et al., 2010). The extraction pattern of water from soil depends therefore on the interplay of RSA, root hydraulic properties, and soil moisture distribution.

Mechanistic modeling of root and soil water flow

In large-scale, hydrological models root water uptake is typically represented by empirical functions that have no physical meaning. Given the complex nature of root water uptake at the level of root systems, these models often misrepresent the impact of RSA on the spatio-temporal pattern of soil water extraction (Javaux et al., 2013). In recent years, more mechanistic approaches based on the explicit description of the three-dimensional root architecture have emerged (Dunbabin et al., 2013). These models link the RSA with physically meaningful parameters that govern plant-soil interactions. For root water uptake, Doussan et al. (1998a; 2006) proposed the "hydraulic tree model", where the water flow is solved numerically in a tree-like system of serial and parallel resistances. This model has been coupled with Richards' equation solvers to describe water flow in the root-soil system (Doussan et al., 2006; Javaux et al., 2008). While such models require a large number of input parameters, which are often difficult to measure, and are computationally quite demanding, they enable the investigation of the water flow dynamics in the root-soil system at a high level of complexity. The ability to manipulate single parameters - inconceivable in experiments - makes them an invaluable tool to investigate hypotheses of how root water uptake is affected by RSA and how plants adapt to variable water availability. Due to the difficulty to measure RSA in-situ, the required RSA information used in these models was hitherto obtained using root

growth models, which generate virtual root systems based on crop specific parameters and rules (Dunbabin et al., 2013).

1.3   Imaging the root-soil system with X-ray CT

RSA is difficult to measure because of its inherent complexity and the fact that roots are embedded in opaque soil. Traditional methods of root detection in soil are destructive and labor intensive (Smit et al., 2000). However, recent advances in non-invasive imaging methodologies enable the direct observation of root-soil interactions and the dynamics of these interactions during plant growth (Downie et al., 2014). The most frequently used techniques to image plant roots in-situ include magnetic resonance imaging (Pohlmeier et al., 2008), neutron radiography (Oswald et al., 2008), and X-ray CT (Mooney et al., 2012). The major drawback of MRI and neutron imaging is the high cost and the limited accessibility of the hardware. In comparison, X-ray CT is much more accessible to researchers, which partly explains its increased use in plant-soil CT studies. A modern industrial CT scanner consists of an X-ray tube, where the beam is generated, a rotary sample stage, and a digital detector, where the signal is recorded.

Production of X-rays

In the X-ray tube, high energy electrons are focused on a metallic target. When the electrons hit the target X-rays are produced by two different mechanisms:

a) The incident electron is decelerated by coulombic interaction with a target atom. The electron loses kinetic energy and a photon is emitted, thereby satisfying the law of energy conservation. This type of X-ray radiation is called bremsstrahlung and it produces a continuous spectrum of X-ray energies. The maximum energy of bremsstrahlung is determined by the tube current, i.e. a tube current of 100 kV can produce X-rays with a maximum energy of 100 keV

b) The incident photon knocks an orbital electron off the inner shell of the target atom. An electron from an outer shell replaces the vacancy and a photon is emitted with an energy equivalent to the energy difference between the higher and lower states. The emitted photons are called characteristic X-rays, because they have a characteristic energy, which depends on the target element.

X-ray interactions with matter

There are four major types of X-ray-matter interactions: a) Rayleigh scattering, b) Compton scattering, c) photoelectric absorption and d) pair production. The proportion of the different interactions depends on the energy of the photons and the elemental composition of the radiated material. In the energy ranges used in soil-plant studies, Compton scattering and photoelectric absorption are the predominant effects. Compton scattering is an interaction most likely to occur between a photon and an outer shell electron. The incident photon is scattered at some angle and at a loss of energy. The electron is ejected with a kinetic

energy equal to the energy difference of the incident photon and the scattered photon. In photoelectric absorption, the incident photon is completely absorbed and its energy is transferred to an inner shell electron, which is ejected from the atom. The kinetic energy of the ejected electron is equal to the incident photon energy minus the binding energy of the electron. The photoelectric effect results in a vacancy in an inner shell, which causes a cascade of refilling by electrons from shells with lower binding energies. Both Compton scattering and photoelectric absorption result in the ionization of the atom. Absorption and scattering cause the attenuation of the X-ray beam. Attenuation is necessary to acquire image information about the scanned material. For a monochromatic beam of photons passing through a homogeneous material of thickness x, the number of photons transmitted without interaction (N) can be calculated by

$$N = N_0 \cdot e^{-\mu x} \qquad (1.6)$$

where N_0 is the number of incident photons, and μ is the linear attenuation coefficient [L^{-1}]. The linear attenuation coefficient is the sum of the individual attenuation coefficients for each type of interaction and depends on the photon energy of the X-ray beam, the density, and the atomic number of the material. In practice the analyzed material will be heterogeneous and μ will vary along the beam path. Equation 1.2 must therefore be rewritten as an integral:

$$N = N_0 \cdot e^{-\int_0^x \mu(\xi)d\xi} \qquad (1.7)$$

where ξ is the variable of integration along the beam path. In a standard industrial CT scanner the radiation is polychromatic, i.e the beam consists of a spectrum of photon energies. Since the probability of an interaction depends on photon energy, the attenuation of X-rays is no longer exponential. Lower energy photons are preferentially attenuated, which leads to a progressive change of the energy spectrum along the beam path (beam hardening). This is an unwanted effect, which can be reduced by the use of metal filters to reduce the amount of low energy photons ("soft" X-rays) in the beam.

Digital image processing

The attenuated beam is recorded by a digital detector. The intensity received by each pixel of the detector depends on the attenuation of X-rays along the beam path. The result is a radiography, a two-dimensional gray scale image (Figure 1.3A). During a CT scan, the sample is rotated by 360° in discrete steps. At each step, a single radiography is recorded. The complete dataset is processed by a computer,

which transforms the data into a tomography (Figure 1.3B-D), a three-dimensional image, using a back-projection algorithm based on the Radon transform. In the resulting three-dimensional image, each voxel (volume element) has a unique gray value corresponding to the attenuation of X-rays at this specific location. Because the attenuation of X-rays is proportional to the density of the material, a CT image contains valuable three-dimensional structural information of the scanned object. Therefore, X-ray CT can be used to determine root system architecture directly in soil, including its temporal development, interactions with specific soil features, or soil water and nutrient availability.
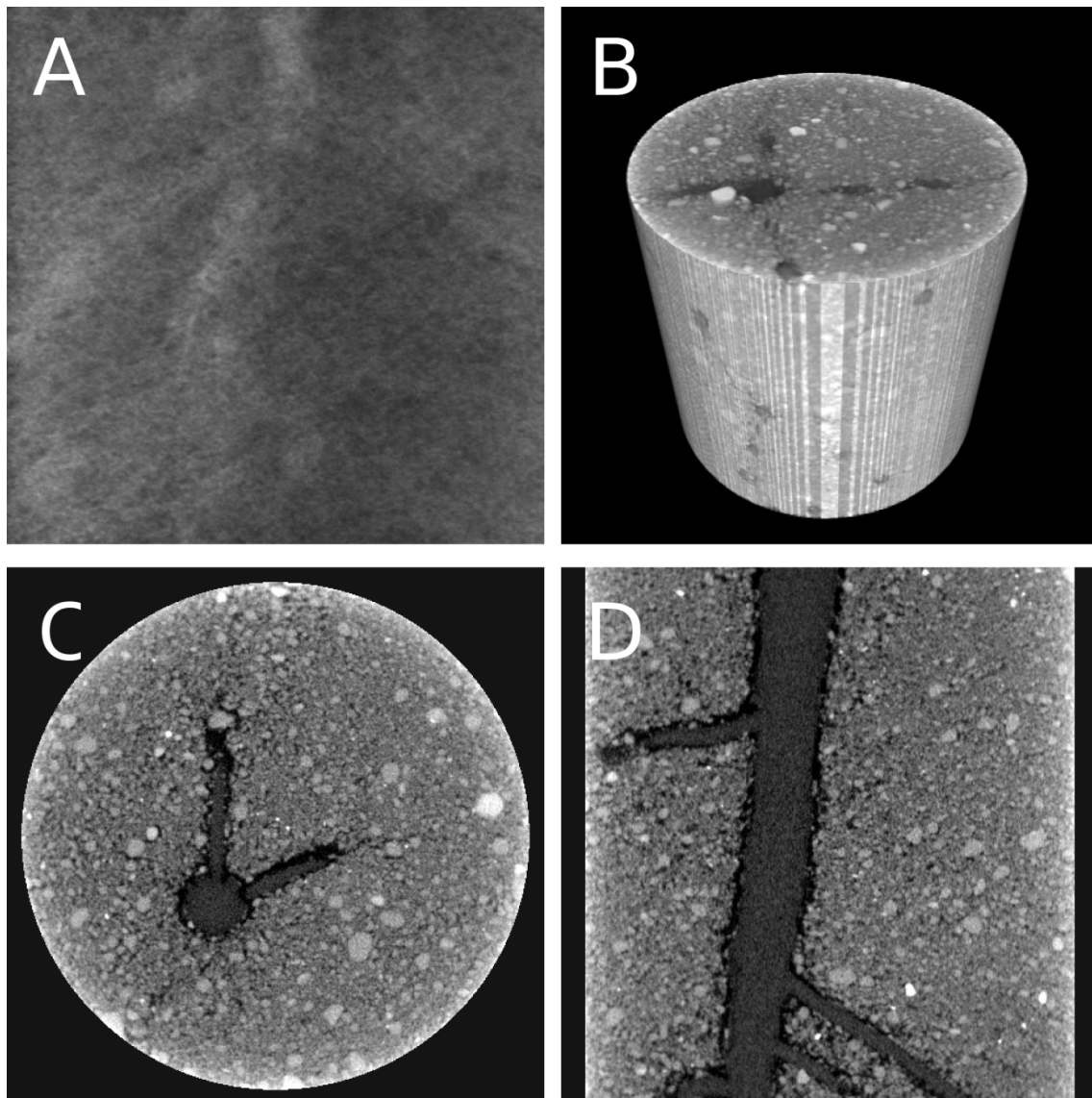
Figure 1.3: CT scan of a soil core containing roots A) 2D Radiography B) 3D rendered view of the reconstructed volume C) Horizontal slice D) Vertical slice

To be able to quantify the architecture and growth of roots in soil, image contrast and resolution must be good enough to enable the isolation (or segmentation) of roots from soil. Any spatial information in a tomography is

discrete, therefore the size of a single voxel (i.e. the spatial resolution) determines the minimum size of any detectable feature. In current industrial CT scanners the X-ray beam is cone-shaped; there is a trade-off between the size of an analyzed sample and the level of detail at which structural information can be gained. For plant-soil studies using pot experiments, this means that a compromise has to be found between pot sizes that are large enough to minimize the constraints of the pot geometry on root growth and the level of detail at which roots and soil can be visualized. Any roots with smaller diameters than the resolution will be lost. Some soil pores will always be smaller than the resolution, so that the gray value of a single soil voxel will correspond to the average attenuation coefficient of its components, which may be air, solid particles and water. The heterogeneous nature of soil complicates the detection of roots, because the gray values of both show a considerable overlap (Kaestner et al. 2006). Therefore, roots cannot be segmented using a global threshold. A number of algorithms have been proposed to overcome this problem, e.g. by using region growing (Kaestner et al., 2006) or more automated tracking approaches (Mairhofer et al., 2012). In the resulting binary images, roots appear as a complex three-dimensional object. Digital image analysis can be used to quantify the root architectural traits.

1.4   Objectives

The main objective of this thesis is to improve the understanding of root water uptake and its dependence on and interplay with RSA. As outlined in this introduction, root water uptake is a highly complex process that is, at a given transpiration rate, governed by the water availability of the soil, the architecture of the root system and the hydraulic properties of both soil and roots. These properties are potentially highly variable with time and space, difficult to measure and to interpret accurately. The potential of X-ray CT to observe and describe the dynamic development of RSA and thus enable a more realistic representation of root water uptake was explored by using a combined approach of CT imaging, experiments and numerical modeling.

Hitherto, no coherent set of methods for the quantification of RSA in-situ, including the temporal dynamics of root development, is available. In *Chapter 2*, a methodological approach to the visualization and quantification of RSA of a growing broad bean (*Vicia faba* L.) root system using X-ray CT is presented. The chapter focuses on architectural traits that are linked to root uptake processes, i.e. root length distribution and the degree of soil exploration. Since root systems are by no means static and the extent of the root system, the distribution of roots in the soil, and the physiological properties of individual root segments change with time, special emphasis is given to the dynamic aspects of RSA. Root growth, the change of root distribution over time, and root demography (age distribution) are quantified. When RSA can be quantified non-invasively over time, it can be determined during running experiments with growing plants.

In *Chapter 3*, a split root experiment is presented, where X-ray CT was used to image and quantify the development of RSA during a drying period. Simultaneously, soil and plant water status were measured. Paraffin layers were used to generate hydraulically isolated compartments, allowing the analysis of local root water uptake with respect to the distribution of roots in the different compartments. Secondly, the split root setup led to a heterogeneous distribution of soil moisture, which is generally the case under field conditions. How root water uptake is affected by the heterogeneous distribution of soil moisture in the root zone is an important question that can be addressed using split root experiments. In cooperation with the Agrosphere Institute (IBG-3) at Forschungszentrum Jülich the temporal sequence of measured root architectures was used to generate dynamic virtual root systems, including information on root age of individual roots. The virtual root systems were used in the mechanistic three-dimensional root water uptake model R-SWMS to simulate root and soil water flow and their effect on plant water status. Comparison

of experimental data and simulation results was used to interpret the water flow dynamics.

Root water uptake may additionally be affected by small-scale alterations of hydraulic properties at the root-soil interface, such as soil compaction around roots (Aravena et al., 2014), root exudates (Carminati et al., 2011; Dunbabin et al., 2006; Hallett et al., 2003) or root shrinkage (Carminati et al., 2013; Tinker, 1976). Such alterations have important implications for the efficiency of water uptake by plants (Carminati and Vetterlein, 2013). In *Chapter 4* a study is described, where X-ray CT was used to quantify the shrinkage of roots and the subsequent reduction of root-soil contact during a drying period. The study aimed at extending previous findings for lupin (Carminati et al., 2013) by using a different species (*Vicia faba*) and refining the imaging approach. A method was developed to measure root-soil contact in-situ to check whether shrinking roots lose contact entirely or retain partial contact to the soil matrix. Plant and soil water status were measured in order to analyze the impact of root-soil contact on root water uptake. Root-soil contact and relative shrinkage of different root orders (taproots and lateral roots) were compared. Different behavior of taproots and laterals may account for functional differences between these root orders.

2   In situ visualization and quantification of 3D root system architecture and growth using X-ray CT

Nicolai Koebernick, Ulrich Weller, Katrin Huber, Steffen Schlüter, Hans-Jörg Vogel, Reinhold Jahn, Harry Vereecken, Doris Vetterlein

2.1 Abstract

Root system architecture and associated root-soil interactions exhibit large changes over time. Non-destructive methods for the quantification of root systems and their temporal development are needed to improve our understanding of root activity in natural soils. X-ray computed tomography was used to visualize and quantify growth of a single *Vicia faba* root system during a drying period. The plant was grown under controlled conditions in a sandy soil mixture and imaged every second day. Minkowski functionals and Euclidean distance transform were used to quantify root architectural traits.

We were able to image the root system with water content decreasing from 29.6 % to 6.75 %. Root length was slightly underestimated compared with destructive measurements. Based on repeated measurements over time it was possible to quantify the dynamics of root growth and the demography of roots along soil depth. Measurement of Euclidean distances from any point within soil to the nearest root surface yielded a frequency distribution of travel distances for water and nutrients towards roots.

Our results demonstrate that a meaningful quantitative characterization of root systems and their temporal dynamics is possible.

2.2   Introduction

The plant root system is of elementary importance for plant growth and performance as it constitutes the interface for the uptake of water and nutrients from soil. When these resources are scarce or unevenly distributed, uptake efficiency and hence plant productivity is largely determined by the spatial configuration, or the architecture of the root system (Lynch, 1995). To further advance our understanding of root-soil interactions a more detailed knowledge of the root system architecture (hereafter referred to as RSA) and its temporal dynamics in response to biotic and abiotic constraints is required. RSA will also determine the extent and spatial configuration of rhizosphere which comprises the region of soil influenced by root activity. Root tissue differentiates with increasing age and hence, the same is true for physiological functions of roots. As a consequence large variations in root morphology and physiological properties can occur among roots within a root system (Hodge et al. 2009). Again this extends to rhizosphere properties which may also show a high variation (plasticity) within the same root system (Carminati and Vetterlein, 2013).

Despite its importance for plant-soil interactions there still remains a substantial gap in understanding the role of RSA, its temporal dynamics and related processes at the soil-root interface. This is due to the difficulty of acquiring three-dimensional data on root distribution over time. Traditional methods of root detection are based on separating roots from soil by washing and subsequent analysis of the extracted roots. With these methods the explicit spatial context (i.e. the relationship of roots to each other and to specific soil features) is lost and loss of fine roots during washing can lead to a substantial underestimation of root length (Pierret et al. 2005). In addition repeated analysis of the same root system over time is impossible. Rhizotrons enable the continuous observation of root growth by monitoring roots in contact with transparent observation windows. While the observation is non-destructive, rhizotrons only provide a two dimensional representation of the 3D root architecture and the observation windows impose constraints on root development that are different from undisturbed soil (Neumann et al., 2009). Problems of root detection can be avoided by growing roots in translucent materials, as in hydroponics, aeroponics or gels. However, such approaches are of limited value for the investigation of root-soil interactions since the artificial media affect root growth patterns and root morphology (Hargreaves et al., 2009). Transparent soils (Downie et al., 2012) might help to overcome this problem but it remains unclear whether they are able to mimic the properties of real soils.

Non-invasive techniques developed in the last decades, have the potential to overcome the limitations of the traditional approaches. They enable imaging of roots in undisturbed soil and thus, are becoming the state of the art in root research. Currently the most advanced techniques are neutron radiography/tomography, magnetic resonance imaging and X-ray tomography. Neutron radiography/tomography is a promising tool to image roots and water content in soil, as neutrons interact strongly with hydrogen nuclei. It is therefore particularly suited for the study of plant-water relations (Carminati et al., 2010). However, neutron imaging techniques involving soil are limited to 2D radiography of thin samples or in the case of tomography to very small sample sizes (27 mm diameter; Moradi et al., 2011). A major limitation to the widespread use of neutron radiography or tomography is the limited accessibility of neutron sources. Magnetic resonance imaging (MRI) is based on the magnetic excitation of atomic nuclei (mainly hydrogen) when placed in a strong magnetic field. Like neutron imaging MRI is very effective in imaging roots and water distribution in soil (Pohlmeier et al., 2008; Stingaciu et al., 2013). Major limitations are the negative influence of paramagnetic particles on image quality (Heeraman et al., 1997) and, as with neutrons, its limited accessibility.

The most promising technique for non-destructive imaging of roots in soil is X-ray computed tomography (X-ray CT). X-ray CT was originally developed for medical uses and is based on the attenuation of X-rays along a sample placed in the beam path. The attenuation of X-rays depends on electron density of the material and therefore different materials can be distinguished easily. In a recent review Mooney et al. (2012) provided an overview of the growing application of X-ray CT to study plant-soil interactions. While early applications of X-ray CT in this field struggled with the detection of fine roots (Heeraman et al., 1997; Perret et al., 2007) newer scanners provide much higher spatial resolutions now enabling the visualization of very fine roots (Tracy et al., 2010). Still some limitations to the technique remain. The most important limitation for analysing RSA is the limited field of view, which prevents the study of large root systems that grow unconstrained by container geometry. Another common problem is the trade-off between sample size and resolution and, most notably, the difficulty to distinguish between roots and soil, which have overlapping attenuation values (Kaestner et al., 2006). A number of semi-automatic algorithms have been proposed (Pierret et al., 1999, Kaestner et al., 2006). Recently, more automated tracking approaches have been developed (Jassogne, 2009; Mairhofer et al., 2012). Their general applicability has yet to be proved. The result of segmentation is a binary image where the roots appear as three-dimensional, convex objects, which can be analyzed with tools from digital image analysis. While the technical development now allows high quality images, no coherent set of methods for the quantification of RSA has been

18

established. Likewise, the potential of analysing growth by repeated measurements has not been fully exploited so far.

In this paper we will show how tools from image analysis developed in other disciplines can be adopted and modified for a quantitative description of the relevant root traits including their temporal dynamics. This is possible with modern CT scanners allowing for a full tomography within very short time (minutes). Recently, Tracy et al. (2012) were able to quantify the impact of soil compaction on RSA development of young tomato roots, which were repeatedly imaged over 10 consecutive days. We show that this is also possible for more mature root systems of considerably larger size. Four dimensional data sets provide the potential to assign roots within the same root system to different age classes with distinct properties. As relevant root traits we focus on the spatial structure which is directly linked to transport and uptake processes. This structure can be described by basic geometrical features such as root length density. Beyond these basic features also the spatial distribution at the level of the root system is deemed to be relevant for the exploration of soil by plants. This can be expressed in terms of the distribution of inter-root distances which are directly related to travel distances for water and nutrients within a soil. These are classically calculated from root length density assuming that roots are evenly distributed. Using new imaging tools these properties can now be measured directly based on 3D distance transform provided by mathematical morphology.

2.3   Material and Methods

Plant material and sample preparation

A sandy soil substrate was prepared by mixing quartz particles of different size classes, consisting of 85 % sand, 10 % silt, and 5 % clay (Vetterlein et al., 2007). Additionally 50 g kg^{-1} of gravel (2-3 mm) and 20 g kg^{-1} of plastic beads (polypropylene, 2-3 mm) were added as internal reference for electron density. The mixture was filled into a cylinder ($\varnothing$ = 12.5 cm, h = 21.5 cm) by passing it through two sieves of 4 mm mesh size separated by a distance of 10 cm. This procedure produced a homogeneous packing (no visible layers in X-ray CT) of the soil at a bulk density of 1.53 g cm^{-1}. The cylinder had a porous plate at the bottom which was connected with tubing to a water source. The soil was watered with a nutrient solution by slowly elevating the water table to full saturation and then drained by slowly lowering the water table to the bottom of the sample (soil matric potential ψ = 0 hPa). *Vicia faba* L. 'Fuego' seeds were surface sterilized in 10 % H$_2$O$_2$ solution for ten minutes, thoroughly rinsed in deionized water and subsequently imbibed for one hour in a saturated CaSO$_4$ solution. Seeds were placed on wet blotting paper and placed in a dark cabinet at room temperature for 2 days to allow germination. A germinated seed was carefully placed in a prepared cavity in the soil at a depth of 1 cm. The cavity was then refilled with sand. The soil surface was covered by a 2 cm layer of fine quartz gravel to reduce evaporative losses. The plant was grown under controlled conditions in a climate chamber (23° C day / 18° C night, 65 % relative humidity, photoperiod of 14 hours, photon-flux density of 350 µmol m^{-2} s^{-1}). The plant was placed on a KERN 572 weighing cell (Kern & Sohn GmbH, Balingen, Germany), and grown over 32 days with no additional watering. Four micro-tensiometers (Vetterlein et al., 1993) were inserted horizontally through boreholes at 1.5, 6.5, 11.5 and 16.5 cm depth respectively to monitor the matric potential, ψ, during desiccation. Integrated volumetric soil water content (θ) at the time of the first tomography was 29.6 % corresponding to ψ_m = -23 hPa at 1.5 cm depth.

CT Scanning

Throughout the 32 day growing period, the sample was scanned every second day during the night phase with an industrial X-ray micro-CT scanner (X-Tek HMX 225) with a finefocus X-ray tube (spot size of 5 µm) using a voltage of 200 kV and a current of 250 µA. We recorded 800 projections with an exposure time of 200 ms. The height of the cylinder (21.5 cm) surpassed the field of view (12.7 x 12.7 cm), therefore separate scans of the upper and the lower part of the sample had to be performed. The total scan time was about 10 minutes. This fast procedure was chosen to reduce potential disturbance of the plants. In X-ray CT

there is always a trade-off between sample size and resolution. To offer growth conditions as close as possible to reality, and given the relatively thick roots of *Vicia faba* we decided to prioritize on a sample size that reduced the constraint of the container geometry on RSA. With our column diameter of 12.5 cm we achieved a resolution of 245 μm voxel side length.

Destructive sampling

At the end of the experiment, the bottom of the cylinder was opened and the soil pushed out gently. The bottom 4 cm of soil that could not be imaged were cut off with a knife and stored separately. Thereafter roots were extracted from the remaining soil column by washing using sieves of 3 and 2 mm mesh size successively. Roots were stored in Rotisol and scanned the next day on a flatbed scanner (EPSON Perfection V700 PHOTO) and the scanned images were subsequently analyzed for length, surface and volume within individual root diameter classes with WinRHIZO 2009b (Regent Instruments, Inc., Quebec, Canada) software.

Image processing and segmentation

All image operations were carried out using the software packages QuantIm and QtQuantIm (www.quantim.ufz.de; Vogel et al. 2010). Due to slightly changed positioning of the sample at different days (scan times), images had to be aligned by manually searching for identifiable features (i.e. tensiometers, plastic beads and quartz gravel particles) in samples from different dates. The exact voxel positions of 10 features in each image were cross-referenced with the other dates. Based on these reference points a transformation matrix is calculated that matches the images. Normalization of gray values was performed by fitting the gray values of manually set reference points. These were gravel particles and polypropylene beads, which do not change their properties with changing water content. The raw images were filtered with a total variation filter (Rudin et al., 1992, *Appendix 1, Figure A1.1B*) to remove small scale noise and, additionally, with a pseudomedian filter (Pratt, 2007, *Appendix 1, Figure A1.1C*).

This second step served two purposes: one was to enhance the contrast between roots and soil and the second was to remove beam hardening artefacts. Segmentation was done using a region growing algorithm which iteratively dilates a region starting from a manually set seed point (*Appendix 1, Figure A1.1E*). Thresholds were manually chosen by the user based on the visual inspection of the results. A similar approach was used by Pierret et al. (2002) for the segmentation of biopores from soil. After segmentation the image was clipped using a cylindrical mask to remove parts of the container walls which were identified as roots. This led potentially to the loss of some roots growing directly at the wall.

Quantification of root traits

   Quantification of root properties was performed with tools from mathematical morphology and integral geometry. For the estimation of root length we calculated the Minkowski functionals for the binary images. For a description of the theoretical background of Minkowski functionals and the algorithmic implementation see Vogel et al. (2010). In three-dimensional Euclidean space there is a direct geometric interpretation for these functionals for a given object X which in our case is the root system: The first functional $M_0(X)$ is simply the total volume of the object, the second functional $M_1(X)$ corresponds to the surface area of the object boundary δX. The third functional $M_2(X)$ is the integral of mean curvature of this boundary. For cylindrical structures $M_2(X)$ is directly related to the length of the cylinder (see also Ohser and Schladitz, 2009). It is defined as

$$M_2(X) = \int_{\delta X} \frac{1}{2}\left(\frac{1}{r_1} + \frac{1}{r_2}\right) ds \tag{2.1}$$

   where r_1 and r_2 are the minimum and the maximum radius of curvature for the surface element ds, respectively. For a cylinder r_1 is the cylinder radius (r_c) and r_2 is ∞. This leads to

$$M_2(X) = \int_{\delta X} \frac{ds}{2r_c} \tag{2.2}$$

Insertion of the surface area yields

$$M_2 = \frac{2\pi r_c l_c}{2r_c} \tag{2.3}$$

so that the length of the cylinder is obtained by

$$l_c = \frac{M_2}{\pi}$$

(2.4)

It follows from Eq. 3.4 that the cylinder radius has no influence on the outcome of the estimation of length. Quantification of root volume and surface area is theoretically possible, but both require a higher resolution to give robust results. The reliability of the Minkowski functionals in estimating root length was evaluated using virtual root systems that differed in total root length and branching density. Therefore a number of realizations of different root systems (N=13) was generated using the root growth module from R-SWMS, as described by Clausnitzer and Hopmans (1994) and Somma (1998). The model parameters branching rate and elongation rate were varied to generate the different root systems. The root systems had three root orders, i.e. the taproot, first order laterals and second order laterals. Branching densities ranged from 0.16 to 1.07 cm^{-1} and the total length of the root systems from 19 to 375 cm. The mean diameter of the roots was 0.15 ± 0.02 cm. The output of R-SWMS consists of a list of logically connected nodes, where each node forms a segment with its subsequent node. Certain properties are assigned to each node, e.g. its coordinates in space (3D), the connection within a branch, a radius, and the surface of the corresponding segment. To generate data comparable to X-ray measurements, the nodal information was digitized on a cubic voxel grid with a resolution of 200 µm, using a program written in Matlab. As an alternative we additionally estimated root length using the more classical approach of skeletonizing the images and measuring the length of the skeleton using the "Analyze Skeleton" tool in ImageJ (Arganda-Carreras et al., 2010). It should be noted, that the approach based on the mean curvature is computationally much more efficient.

Distance transform

In order to directly measure diffusion lengths for water and nutrients towards the roots we performed a 3D Euclidean distance transform on the binary image. In the resulting image for each non-root voxel the Euclidean distance to the next root voxel is assigned as a gray value. A frequency distribution of distances over depth was generated by subsequent division of the domain into horizontal layers of 1 cm thickness and creating the histogram of distances for each layer. For each 1 cm layer the "half mean distance" (HMD) between roots was calculated from root length density with the classical formula HMD = $(\pi R_L)^{-1/2}$ (Equation 2.5), where R_L is root length density (Gardner, 1960; Newman, 1969). HMD is often used as an approximation of the travel distance for water when modeling root water uptake.

Root demography

        Comparison of root length between subsequent dates was performed to quantify the age distribution of roots within the soil. The difference in root length between subsequent dates within horizontal 1 cm slices was calculated and the result interpreted as root growth. As the temporal resolution was two days, new roots within a slice were labeled with a maximum age of two days. If there were no changes between dates or a reduction of root length we assumed no growth.

2.4   Results

Plant and soil measurements

The plant reached a height of 23.4 cm and a leaf area of 160 cm² at the end of the experiment. There were no signs of nutrient deficiency or wilting. Volumetric soil water content (θ) at the end of the experiment was 6.75 %, soil matric potential ψ_m was below -700 hPa (below the measurement range of our tensiometers).
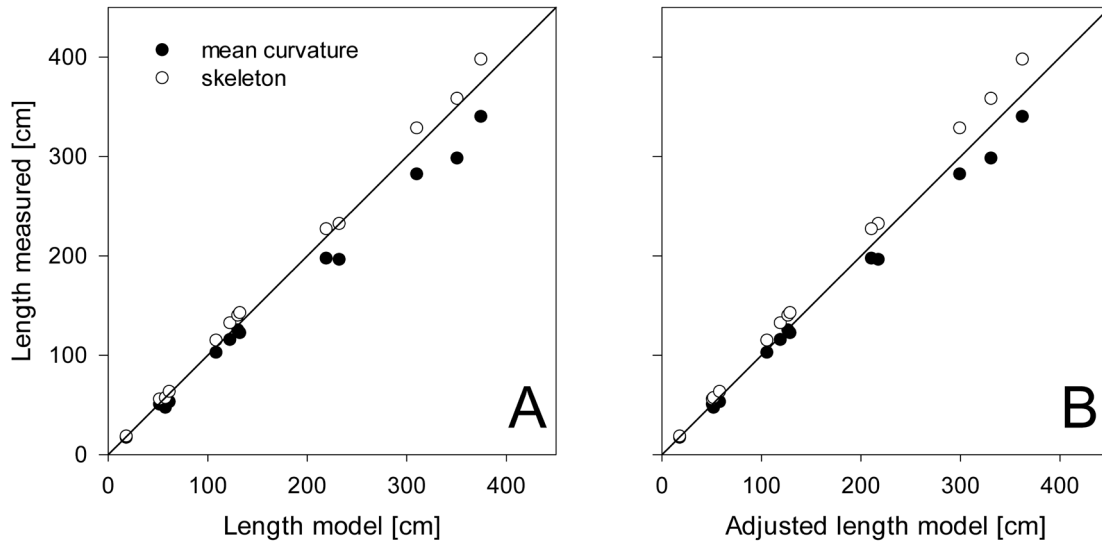

Figure 2.1: Root length estimated with mean curvature and the length of the skeleton, respectively, over A) the actual root length of the virtual root system B) the adjusted root length corrected for the overlap at the base of each branch root. The solid lines represent the 1:1 relationship

Estimation of RSA in virtual root systems

For the evaluation of root length estimations using the virtual root systems we calculated a relative error using the equation ($L_{estimated} - L_{model}$) / L_{model} (Equation 2.6). Root length of the virtual root systems was underestimated by 9.8 ± 4.8 % (mean error ± standard deviation of error) when using mean curvature, and overestimated by 3.9 ± 3.3 % when measuring the length of the skeleton (Figure 2.1A). The absolute deviation of root length calculated with mean curvature to the actual root length was highly correlated with the total number of branches (Figure 2.2). A multiple linear regression with total root length and the number of branches as independent variables showed that only the number of branches was significant ($P < 0.01$), while total root length was not significant ($P = 0.08$). We additionally calculated an adapted length for the virtual root system, which removed the basal part of each lateral root that was overlapping with the parent root. The adapted length corresponds to the length that would be measured using a measuring tape. Because the branching angle was 90°, we subtracted the radius of the parent root for

each branch. When using the adapted length, the mean curvature approach underestimated root length by 6.1 ± 3.1 % while skeletonization overestimated root length by 8.2 ± 2.6 % (Figure 2.1B).
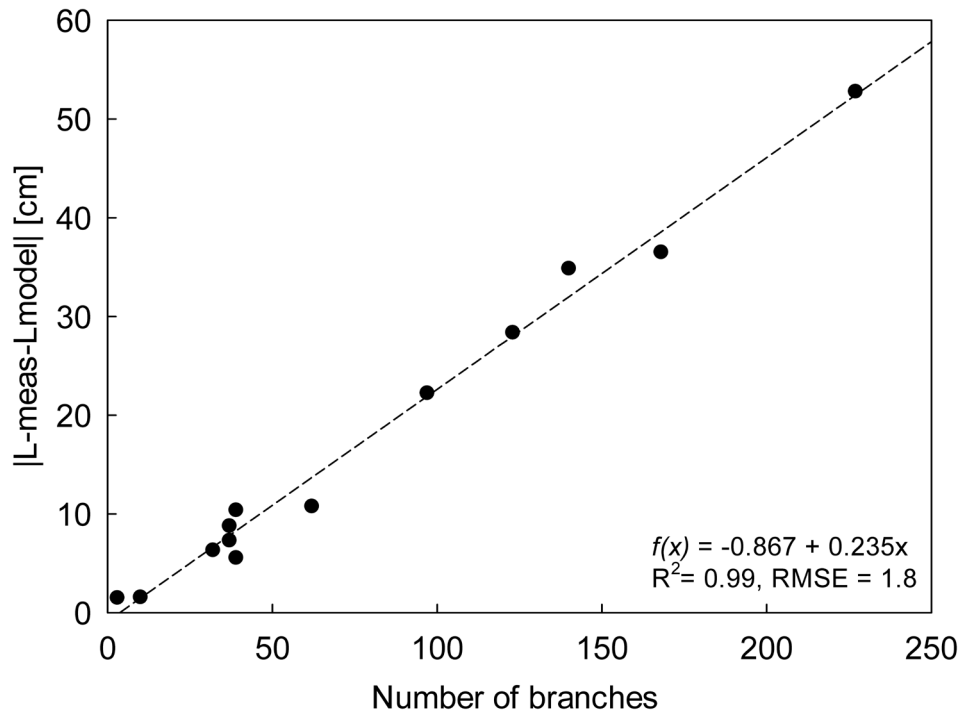

Figure 2.2: Absolute deviation of root length estimated with mean curvature from modeled root length over number of branches. The dashed line represents the linear regression

Image processing and segmentation

The raw X-ray CT images were 16-bit grayscale volumetric images with a size of 512 x 512 x 512 voxel corresponding to 12.5 cm in each direction. The mechanism for attaching the porous plate to the soil cylinder at the bottom required an additional plastic ring to firmly seal which caused photon starvation at the lower end (4 cm), so not the entire root system could be imaged. The upper 1 cm of the sample was clipped, as it contained only the seed but no roots. The resulting image size after joining the upper and lower image was 512 x 512 x 595 voxel (14.5 cm in z-direction). The region growing algorithm worked fine for the taproot and the thickest lateral roots but due to low contrast a very conservative threshold had to be selected. Finer lateral roots had to be added by setting new seed points and repeating the procedure until there were no visible roots left. The resulting root system of four selected dates is shown in Figure 2.3. The segmentation method produced some minor artefacts: i) the repeated setting of new seed points caused the final root structure to be unconnected at some points, ii) the plastic beads in the soil mixture were falsely classified as root if a root was growing next to them, as were some macropores in the topsoil, iii) after day 26 drying of the soil caused the formation of cracks, which caused large errors in the images at day 28 and day 30,

26

while at day 32 most of the cracks could be successfully excluded by a prior segmentation of the cracks using region growing. These artefacts clearly changed the resulting root structure and affected the subsequent quantification of RSA. At 4 days after planting (DAP) only a short taproot (3 cm) was visible. At 6 DAP a set of short laterals emerged at the base of the taproot. At 10 DAP the taproot had reached the bottom of the visible domain and the first laterals had reached the container wall, and were subsequently forced downward. More laterals emerged along the more distal taproot. Until 16 DAP the majority of roots was clearly located in the topsoil, after 18 DAP this pattern changed and root growth was almost exclusively seen in the subsoil.
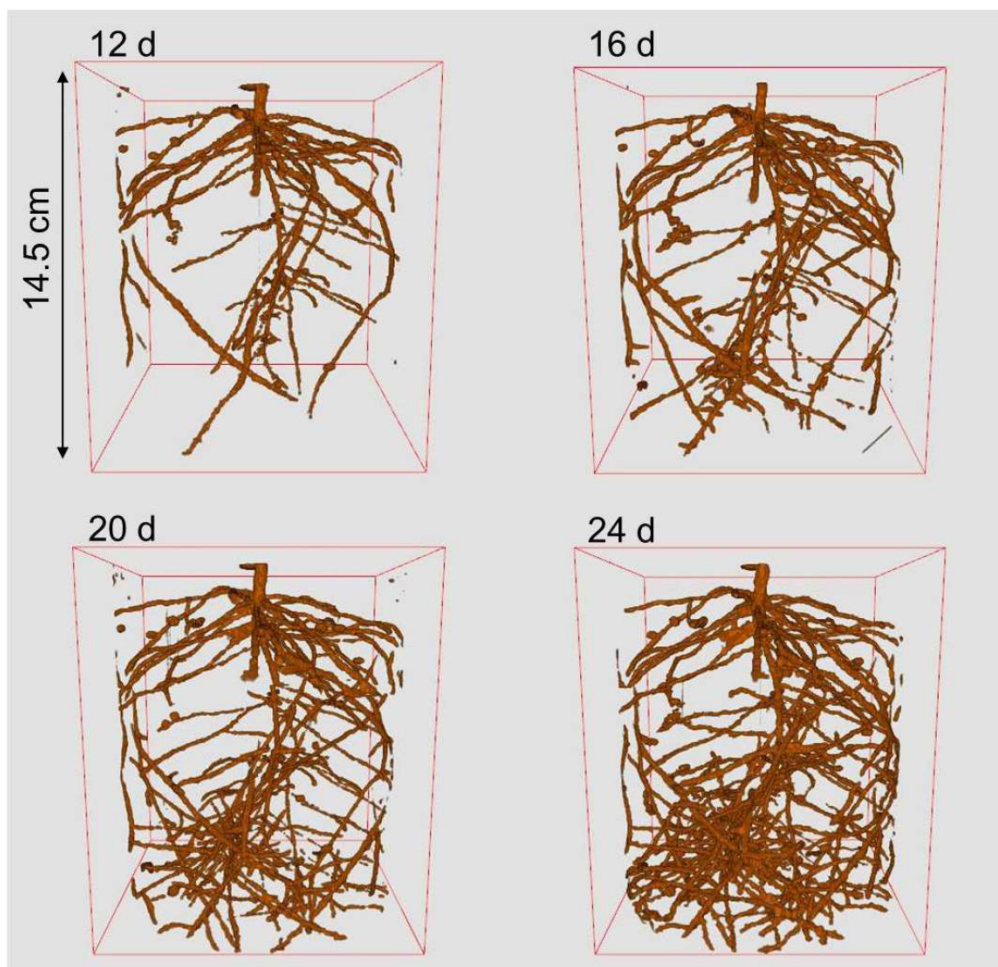
Figure 2.3: 3D rendered view of the segmented root system of Vicia faba after 12, 16, 20 and 24 days, respectively
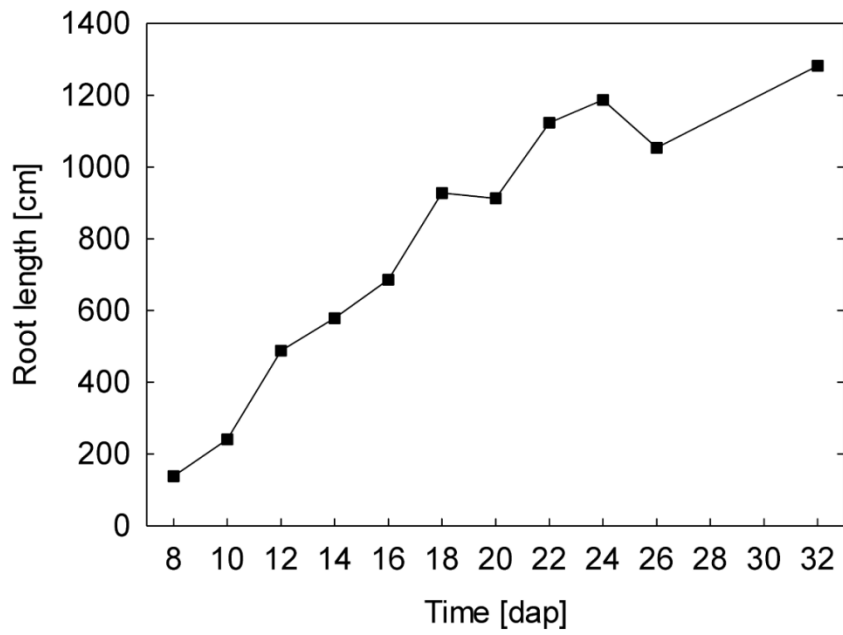
Figure 2.4: Development of estimated root length in the entire imaged sample volume over time
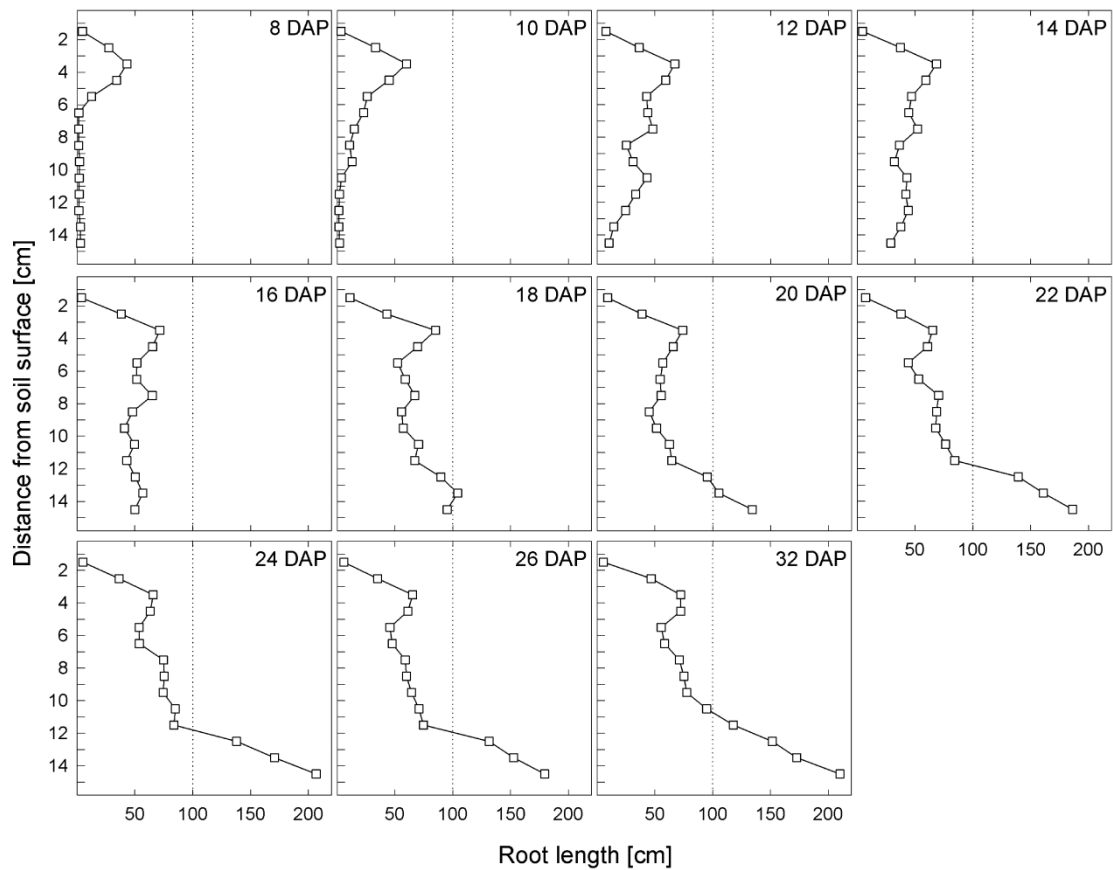

Figure 2.5: Change of estimated root length with depth and time. Each open square represents the root length within a slice of 1 cm thickness. Data from day 28 and 30 were very noisy and excluded from the analysis

Quantification of RSA

The quantification of root length was performed for each image from 8 DAP to 32 DAP. In the whole sample root length increased linearly from 8 to 18 DAP with a slightly reduced growth between DAP 18 and 32 (Figure 2.4). Root length increased for almost all time steps, except for 18 to 20 DAP, and 24 to 26 DAP. Total root length in the sample increased almost ten-fold from 138.25 cm to 1282.4 cm, corresponding to an increase in root length density from 0.08 cm cm^{-3} to 0.72 cm cm^{-3}.

The root length estimation using WinRHIZO after destructive harvest excluding the lowest 4 cm of soil (root length in the lowest 4 cm was 570.1 cm) was 1413.5 cm, 9.3 % higher than the estimation from the tomography. We additionally calculated root length within horizontal layers of 1 cm thickness in order to quantify the vertical root distribution (Figure 2.5). After 8 DAP 90.6 % of root length was in the upper half of the sample and 59.1 % in the upper 4 cm alone. From 18 DAP on there were more roots in the lower part with an increasing percentage until 22 DAP, where 62.9 % of roots were in the lower part with 16.5 % of roots in the deepest layer alone. After 22 DAP the cumulative distribution changed only slightly.
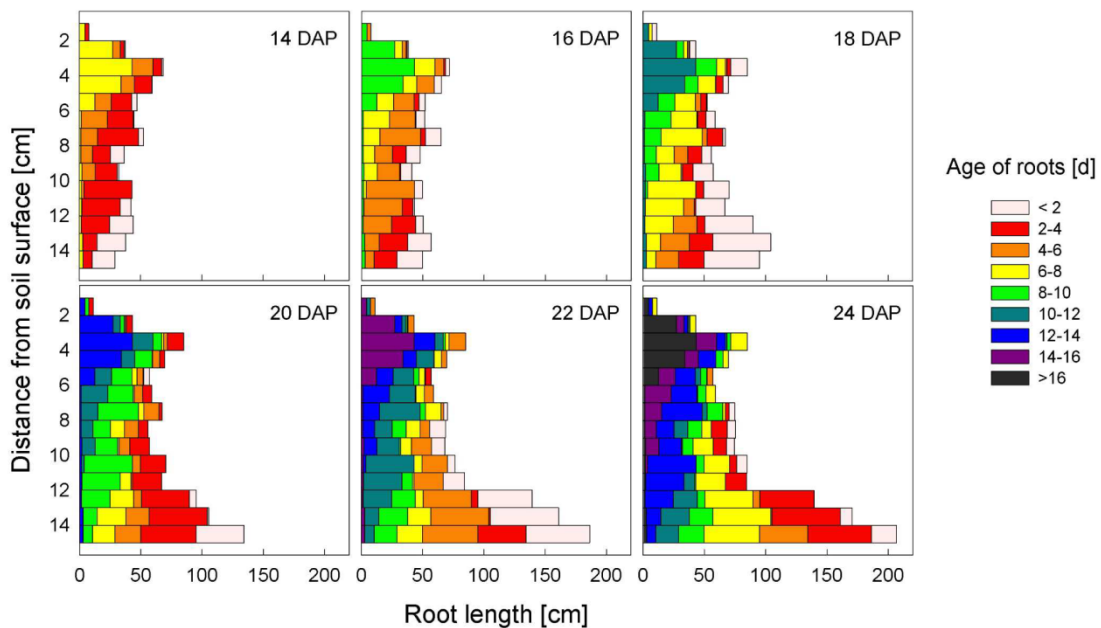

Figure 2.6: Development of root demography along soil depth for six consecutive scans. Horizontal bars represent root length within 1 cm slices. Different colors represent root age

Root age

From differences in root length between two subsequent dates we calculated root growth in each layer. We interpret any increase in root length between successive time steps as new growth. The age of the newly detected roots will have a

maximum age of two days. Roots that were already present at the previous date will have an age of at least 2 days and so forth. When analyzed over the whole period we can generate a vertical root age map (Figure 2.6), i.e. we can show the change of root age distribution with depth and time. The results show that initially young roots were present in the whole profile. After 20 DAP no substantial root growth occurred in the topsoil, leading to an encroachment of young roots in the lower part of the profile, while in the upper part older roots constituted the majority of roots. At 24 DAP in the upper 8 cm more than half of the roots were older than 12 days.

Distance transform

The distance transform of the binary images produced a three-dimensional 'distance map' (Figure 2.7) which shows the Euclidean distance of each non-root voxel to the nearest root surface. The distribution of distances was closely related to root length density, and varied over both time and soil depth. Comparison of the frequency distribution of Euclidean distances to the nearest root surface with the HMD estimated from root length density shows that the bulk of distances are shorter than HMD (Figure 2.8). HMD in the uppermost layer was beyond the shown data range at 14 and 22 DAP because root length density was very low. With time, shorter distances became more frequent, especially in the deepest soil layer, where at 22 DAP more than 70 % of soil voxels were within 5 mm of the root surface.
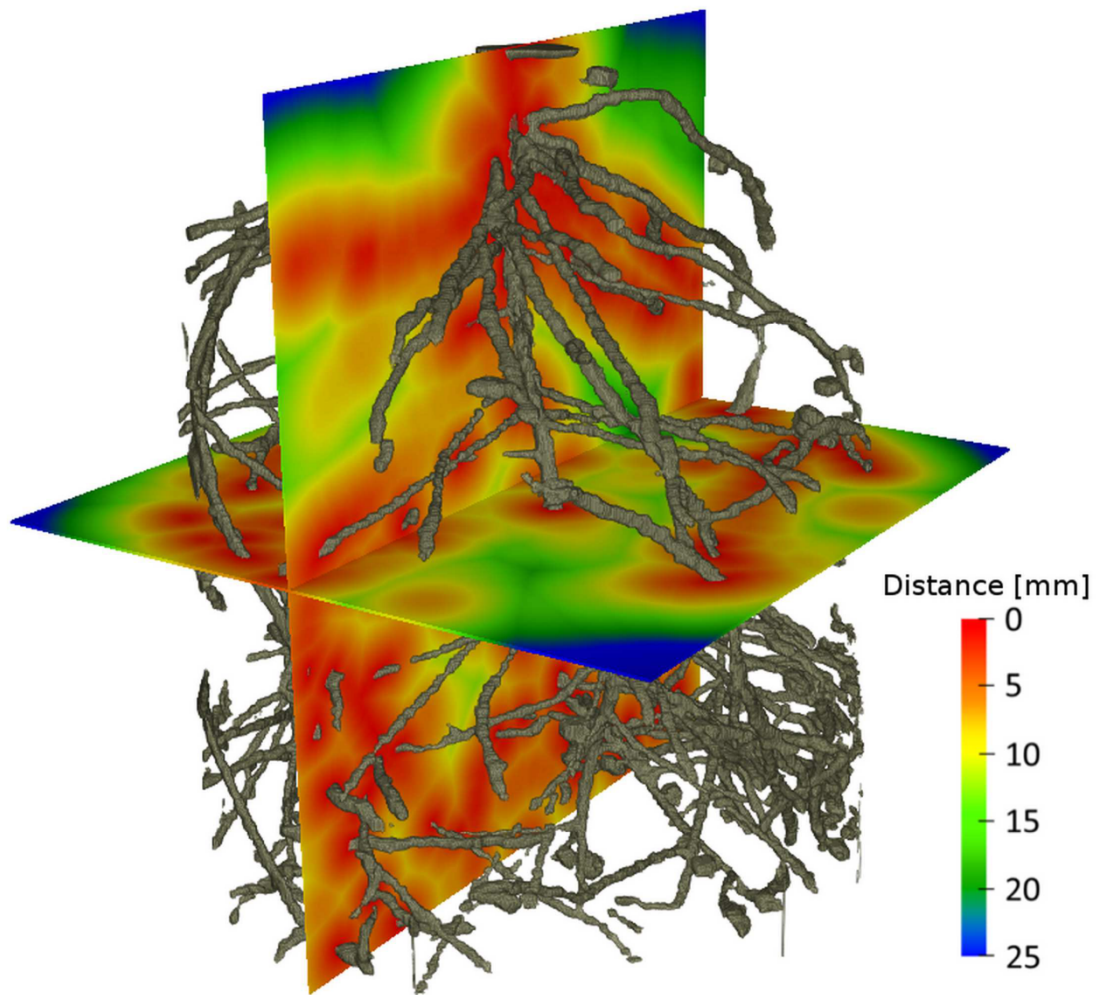
Figure 2.7: Result of the distance transform at 26 DAP on two planes of the three-dimensional image. The 3D rendered root system is added for comparison
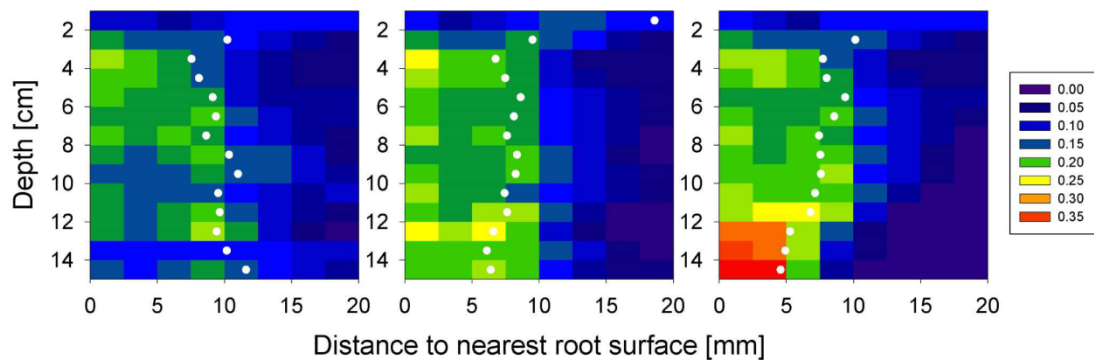

Figure 2.8: Frequency distribution of the 3D Euclidean distances to the nearest root surface over soil depth at 14, 18 and 22 days after planting, respectively. Histograms had 20 equally spaced classes of 2.5 mm width; only the first 8 classes are shown. Colors represent the frequency of each distance class within a 1 cm layer. White circles represent the theoretical "half mean distance" calculated from root length density in each layer

2.5 Discussion

Reliability of the Minkowski functionals

The systematic underestimation of root length based on the mean curvature as compared to the skeleton is highly correlated with the number of branches (Figure 2.2). This can be explained by different sensitivities to root junctions. The root length of the virtual root systems is the sum of Euclidean distances between the connected root nodes. Because lateral roots emerge at the center of the parent root, the total length corresponds to the length of the skeleton. The integral of mean curvature is a measure of the surface of the structure; therefore, at each junction a fraction of the lateral which is covered by the radius of the parent root is not seen. Hence, the loss of root length due to number of branches also depends on root radius. For simple root systems, the approach based on mean curvature can give satisfactory results, however for very densely branched root systems a correction factor might be necessary. Schladitz et al. (2012) used the porosity of an open foam as a correction factor when estimating the strut length of open foams with the same approach. This is based on the assumption that an increasing density and thickness of struts leads to an increased overlap of the struts. This cannot be directly transferred to root systems, because the branching pattern of a root system is less regular than the strut system of foams. It can, however, be argued that the length which is omitted at the junctions is actually excess root length produced by the thinning procedure during skeletonization. This is the reasoning behind the use of adjusted root length. When adjusted root length was used mean curvature estimations were more accurate than skeletonization. Still, some uncertainties remain to the use of mean curvature in length estimation. Root tips increase the mean curvature integral and should therefore lead to an overestimation of length, the same is probably true for surface roughness. The degree of both effects is unknown and should be addressed in future research. Since skeletonization also has some drawbacks (e.g. the sensitivity to surface roughness, which leads to the production of extra branches), we conclude that the approach based on Minkowski functionals is on a par with skeletonization, while being computationally much more efficient. Furthermore, estimation of volume and surface area of roots is possible without additional computational costs when a higher resolution is used (at least 5 voxels diameter, Vogel et al., 2010). This is relevant for future CT studies, given that the resolution of the newest generation of CT scanners is improving fast. On the downside, our approach yields no additional structural information like branching density and number of tips, which is possible with skeletonization.

Quantification of RSA

Although root length in CT images was underestimated by 9.3 % as compared to destructive sampling, the overall ability of our method to quantify root distribution in soil is consistent with previous studies. Flavel et al. (2012) found that CT underestimated root length of wheat by 8 %. They had a much higher resolution (68.23 µm) in their columns of only 30 mm diameter which enabled them to analyze finer roots than in the present study. Earlier studies showed a similar trend of underestimation of root length by up to 10 % (Gregory et al., 2003; Perret et al., 2007) but the opposite trend was also reported (Heeraman et al., 1997). In most of these studies the size of the system was considerably smaller than in our case. A general problem of CT is the trade-off between sample size and image resolution. We specifically aimed for a large sample diameter to provide more realistic growth conditions for the roots, which necessarily leads to reduced resolution. Additionally, in order to penetrate the whole sample we needed higher energy X-rays which produce lower contrast between soil and roots. Finally, the segmentation routine involved different user based decisions that clearly affected the resulting root structure. Even with these limitations we show that X-ray CT can be used to visualize and quantify complex root systems and their development over time. Some of the discrepancy between root length estimated with X-ray CT and WinRHIZO can be explained by the loss of roots that were directly growing at the container wall, due to the cropping of the container wall itself. The smallest structures that can be safely detected should have at least double the size of the resolution if not larger (Vogel et al., 2010), in our case 490 µm, which leads to the possibility of the loss of fine roots. The length of roots with a smaller diameter than 500 µm estimated in WinRHIZO amounted to only 2.7 % of total length; thus this can only partly explain the difference between the two methods. The influence of water content on the accuracy of our measurements was not tested since we only had destructive data for the last day of sampling. Zappala et al. (2013b) reported a significant effect of water content on the success of segmenting a root system from soil showing that volumetric water contents above 25 % lead to a significantly reduced volume of segmented roots from CT as compared to WinRHIZO, probably due to the inability to segment fine roots. In spite of our relatively large sample size, the resulting root distribution was still constrained by the geometry of our container and is therefore not representative of root distributions in the field. The sample size we used was near the maximum that could be entirely penetrated by the X-ray beams without photon starvation. The resulting resolution was good enough to image RSA of *Vicia faba,* which is known for having coarse roots.

Distance measurements

Direct measurement of 3D Euclidean distances to the nearest root surface was performed as a measure for soil exploration of roots. It is a straightforward method to describe travel distance from any point in the soil to the root surface. Potential applications of the distance map include the calculation of water or nutrient uptake, root exudation, root-pathogen interactions, communication in the rhizosphere, determination of chemical or physical gradients in the rhizosphere, and competition between roots to name just a few examples. The frequency distribution of distances depends largely on root length density but can show considerable variation due to non-regular distribution of roots (Van Noordwijk et al., 1993). Comparison with HMD calculated from root length density in two dimensions with Gardner's formula shows that the bulk of measured distances (up to 80 %) are shorter than HMD (Figure 2.8). This is partly due to the fact that HMD is calculated in discrete layers and therefore roots in neighboring layers have no effect on HMD while they are accounted for in 3D distance transform. In our case study, the deviation of HMD from the arithmetic mean of distances derived from 3D distance transform was small, indicating a regular root distribution within each layer (Figure 2.9). Situations, where the deviation between the two methods is larger are likely to occur in larger containers with heterogeneous soil properties or in samples taken from the field (Tardieu, 1988). Since non-regular root distributions will have an influence on the actual water and nutrient uptake of the root system, the frequency distribution of distances might be a better predictor for root uptake than root length density in 1D uptake models. Distance measurements can also be used to analyze the deviation of rooting patterns from randomness (Pierret et al., 1999). The accuracy of the distance map depends primarily on image resolution, as no distances shorter than the voxel side length can be detected. Obviously, also the quality of the segmentation affects the results. Any missing root structures, misclassified macropores, and both under- and overestimation of root diameter, will change the outcome of the distance measurements.

Root age

The non-invasive nature of CT imaging allows the quantification of root age within a root system when the same sample is imaged repeatedly over time. By simple subtraction of root length per layer from subsequent dates, new root growth can be quantified and the age determined based on the temporal resolution, i.e. the time between two scans. In some cases root length decreased between two subsequent scans. When this was the case we attributed the difference to the uncertainty of our method as discussed above and therefore assumed no growth. Estimated root age distributions are a result of the dynamics of root growth in the container. Encroachment of young roots in the deeper soil near the end of the

experiment might hint to preferential growth in moist soil layers but the pattern is also a consequence of the sample geometry as laterals were forced to grow downwards when they reached the cylinder walls. Since root properties can change drastically with the maturation of roots, distribution of root ages can be an important factor in root-soil interactions. So far, experimental data on root age distribution are virtually non-existent for 3D root systems growing in soil. However, studies based on root architectural models show the importance of age-related changes in root functions for water and phosphorous uptake (Doussan et al., 1998b; Schnepf et al., 2012). Such model studies show that there is clearly a need for methods to quantify age distribution within root systems. A method for the spatially explicit assignment of root age for individual root segments using a 3D virtual reality system similar to Stingaciu et al. (2013) is currently under development.
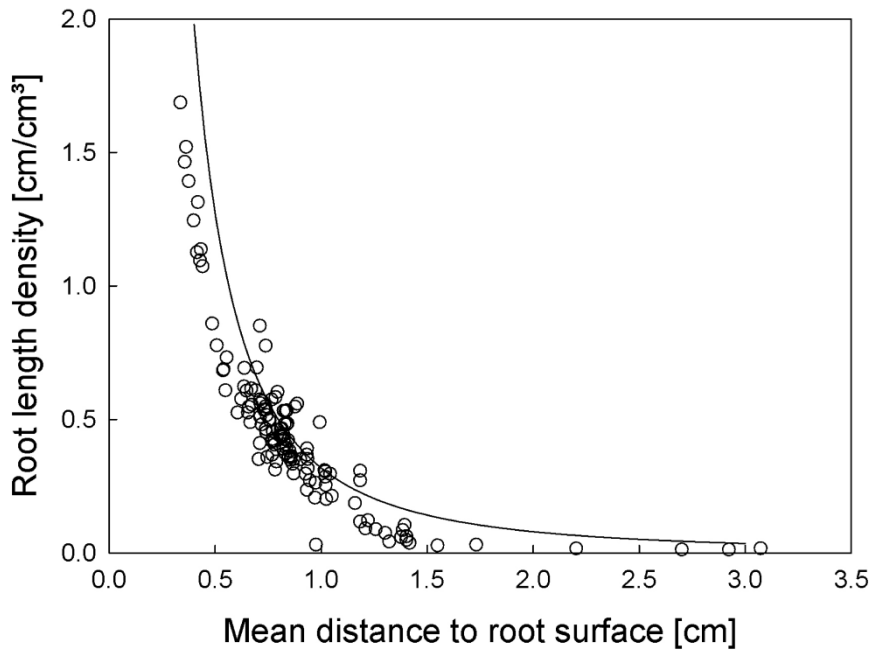
Figure 2.9: Relationship of root length density and mean distance to root surface in each 1 cm layer for every time step. The solid line represents the theoretical relationship of half mean distance and root length density according to Gardner (1960)

2.6   Conclusions

The X-ray technique for imaging soil-root systems was fast and easy to handle. Including the preparation and positioning of the sample the whole procedure lasted 30 minutes per soil column. Weighing of the sample directly before and after the scan showed no measurable water loss during the measurement. It can therefore be concluded that the method provides only little disturbance and can be used during running experiments with plants. Our methods from digital image processing were able to extract the root system of *Vicia faba* for a soil water content decreasing from 29.6 % to 6.75 %. Quantification of root length with Minkowski functionals showed similar accuracy as the classical approach of measuring the skeleton but requires less computational costs. The ability to perform scans at subsequent dates enables the quantification of root growth and the derivation of root demography. Since various root functions change with age, detailed knowledge about the demography within a root system will be very valuable for better characterizing water and nutrient uptake in the future. Measurement of three-dimensional Euclidean distances to the nearest root surface is an efficient tool to determine the frequency distribution of travel distances for water and nutrients to the nearest root. We suggest using this frequency distribution rather than half mean distance derived from root length density to describe the root system as a sink in one-dimensional uptake models, as it can explicitly account for the spatial arrangement of roots.

3   Unraveling the hydrodynamics of split root water uptake experiments using CT scanned root architectures and three dimensional flow simulations

Nicolai Koebernick, Katrin Huber, Elien Kerkhofs, Jan Vanderborght, Mathieu Javaux, Harry Vereecken, Doris Vetterlein

3.1   Abstract

Split root experiments have the potential to disentangle water transport in roots and soil, enabling the investigation of the water uptake pattern of a root system. Interpretation of the experimental data assumes that water flow between the split soil compartments does not occur. Another approach to investigate root water uptake is by numerical simulations combining soil and root water flow depending on the parameterization and description of the root system. Our aim is to demonstrate the synergisms that emerge from combining split root experiments with simulations. We show how growing root architectures derived from temporally repeated X-ray CT scanning can be implemented in numerical soil-plant models. Faba beans were grown with and without split layers and exposed to a single drought period during which plant and soil water status were measured. Root architectures were reconstructed from CT scans and used in the model R-SWMS (root-soil water movement and solute transport) to simulate water potentials in soil and roots in 3D as well as water uptake by growing roots in different depths. CT scans revealed that root development was considerably lower with split layers compared to without. This coincided with a reduction of transpiration, stomatal conductance and shoot growth. Simulated predawn water potentials were lower in the presence of split layers. Simulations showed that this was related to an increased resistance to vertical water flow in the soil by the split layers. Comparison between measured and simulated soil water potentials proved that the split layers were not perfectly isolating and that redistribution of water from the lower, wetter compartments to the drier upper compartments took place, thus water losses were not equal to the root water uptake from those compartments. Still, the layers increased the resistance to vertical flow which resulted in lower simulated collar water potentials that led to reduced stomatal conductance and growth.

3.2   Introduction

Water scarcity is an important abiotic limitation to plant growth and agricultural productivity. Under water limited conditions, changes in root system architecture (RSA) play a major role to reach locations where water is still present, which is often the subsoil. There is no simple relationship between the amount of roots present in certain locations and the actual root water uptake (RWU) from these sites (Pohlmeier et al., 2008). RWU is repeatedly described as a sink moving down the profile with time, only weakly related to root length density in a certain depth (Hainsworth and Aylmore, 1986; Pierret et al., 2003; Garrigues et al., 2006). In many of these studies change in soil water content in a certain depth is assumed to be synonymous with root water uptake. The illustrative Martini glass analogy first used by Zwieniecki et al. (2002) demonstrates that this assumption is too simple. When drinking a sip of Martini with a straw, the Martini is taken up from the bottom of the glass, but a change in "Martini content" is only observed in the upper layer of the glass due to the very high hydraulic conductivity within the glass. Roots and soil matrix are much more complex than the Martini-glass system; however, in soil-plant system the soil hydraulic conductivity and resulting soil hydraulic redistribution also obstruct the view on the site of root water uptake and its temporal dynamics. This has been known for a long time and a number of strategies have been developed to overcome this problem.

An experimental strategy to prevent soil hydraulic redistribution is to divide the root zone into different compartments, which prevent water flow between compartments to permit controlled heterogeneous distribution of soil moisture (Drew, 1975; Herkelrath et al., 1977). In case of horizontal splits, the split layers should additionally be penetrable by roots, which can be, for example, achieved by applying wax or paraffin. When roots take up water in a given compartment the change in total water content can be directly related to root water uptake from this compartment. This assumption can, however, only be drawn if the split layers are completely hydraulically isolated. In the case of water redistribution through the layers, the leakage rate has to be known. Another problem to determine RWU from a soil compartment arises due to the non-linearity of the soil water retention curve. Water content or soil water potential is usually measured at discrete points in the soil. When roots take up water from the soil, strong gradients in soil water potential can develop around the roots. Thus, an extrapolation between point measurements to the complete soil compartment becomes erroneous. A second experimental strategy is to directly observe water flux in soil as it has been successfully demonstrated by Zarebanadkouki et al. (2012). They imaged water flow into roots using neutron imaging of deuterated water. However, this method is hitherto either

constrained to quasi two-dimensions (rhizotrons) or very small root systems and to short time scales.

An alternative approach is to quantify the amount of water being translocated by root or soil hydraulic redistribution. Mechanistic root water uptake models that describe water flow in soil, into, and within roots allow quantifying and locating root water uptake and redistribution of water within the soil and root system. The use of mechanistic models, like R-SWMS (root-soil water movement and solute transport, Javaux et al., 2008), has two prerequisites: (i) that the dominant processes are known and (ii) that the required input parameters are available. To fulfil the latter, dynamic information about RSA as well as hydraulic properties of individual root segments have to be available.

RSA has been obtained in the past using root growth models, i.e. RSA is artificially created based on a set of crop specific parameters and rules (e.g. branching rules, growth rates, etc.) derived from experiments (Clausnitzer and Hopmans, 1994; Leitner et al., 2010; Lynch et al., 1997; Pagès et al., 2004). Mostly, one or several typical realizations of RSA obtained from such models for a plant of a certain age have been used to calculate different scenarios, like root water uptake from saline soils (Schröder et al., 2013), performance of varying root architectural traits under different soil moisture regimes (Leitner et al., 2014), or the impact of stomatal regulation type on root water uptake (Huber et al., 2014).

Root growth models have been used as an alternative to 3D-data of root systems as these were not available in the past. However, such data are now becoming increasingly accessible with non-invasive methods reaching a level of resolution which is sufficient to visualize most or all of the root system. The most advanced techniques for imaging soil-grown roots include X-ray computed tomography (Mooney et al., 2012), neutron radiography (Oswald et al., 2008), magnetic resonance imaging (Pohlmeier et al., 2008), or transparent soils (Downie et al., 2012). These techniques are of particular interest because they allow for repeated measurements. When ionizing radiation is used, it is however important to choose appropriate scan parameters to minimize potential damage to living tissues (Dutilleul et al., 2005; Zappala et al., 2013a). Previous studies clearly demonstrated the potential of X-ray CT to analyze the temporal dynamics of growing roots (Gregory et al., 2003; Jenneson et al., 1999; Lontoc-Roy et al., 2005). While these early studies were limited to young seedlings, more recent work shows that the same is possible for considerably older root systems (Han et al., 2008; Koebernick et al., 2014; Tracy et al., 2012). First modeling approaches based on the use of RSA from non-invasive imaging are available (Stingaciu et al., 2013). The second challenge remains, i.e. the scarcity of data on root hydraulic properties. Measured data are primarily from hydroponically grown very young root systems. Certain assumptions have to be made to separate radial and axial conductivity during the measurements.

Nevertheless, there is a wealth of information on how conductivity changes during root development and these have been used to scale the conductivity of individual root segments (Doussan et al., 1998b; 2006). As roots age the resistance in the axial pathway typically decreases due to the maturation of xylem vessels, while in the radial pathway resistance increases with the development of apoplastic barriers (Bramley et al., 2009; Frensch and Steudle, 1989).

In order to avoid confounding root water uptake and hydraulic redistribution by the interpretation of local changes in soil water content we have chosen two of the above strategies: (i) an experimental approach of introducing barriers to avoid soil hydraulic redistribution; (ii) a modeling approach which takes soil and root hydraulic redistribution into account.

The objective of the current study is to compare experimental (introducing barriers to avoid soil hydraulic redistribution) and modeling approaches (calculation of soil and root water flow) with respect to their capacity to localize root water uptake in the presence of strong gradients in soil water potential. Local changes in soil water content will be compared to measured and modeled root water uptake.

For the experimental approach we combined a classical set up using wax barriers (Drew, 1975) with quantitative measurement of RSA over time via X-ray CT. This setup allowed the observation of the relation between RSA and water uptake and how it is affected by soil drying. The addition of paraffin layers allowed for the development of strong spatial heterogeneities in soil water potential, as is generally the case under field conditions.

For the modeling approach we used the mechanistic 3D model R-SWMS (Javaux et al., 2008), which enables a detailed description of soil and root water flow. While R-SWMS so far has only been applied for static (non-growing) root systems, mostly created by root architectural models, we now extended the existing model by an additional root development module, which uses the measured CT-data of RSA over time. Doussan's concept of changing axial and radial conductivity with age (Doussan et al., 2006) was included by using his root hydraulic parameterization by assigning these parameters to root age classes derived from the time lapse 3D RSA CT-Data.

Apart from modeling the actual experimental setup, root distributions obtained from split experiments were also used in simulations without splits and vice versa. This approach allowed us to (i) reinterpret measurement results, (ii) show the influence of split layers on plant water potentials that could be linked to differences in plant/root growth and eventually on root water uptake and (iii) show where soil water is taken up during root growth.

3.3   Materials and Methods

3.3.1   Experiments

Two subsequent experiments under the same environmental conditions (growth chamber, 23° C day / 18° C night, 65 % relative humidity, photoperiod of 14 hours, photon-flux density of 350 μmol m^{-2} s^{-1}) were conducted with *Vicia faba* L. cv. Fuego.

The first experiment (3 replications), which will be referred to as "NoSplit" in the following, was conducted with homogeneously filled soil columns of 21.5 cm height with unrestricted soil water flow. The second (4 replications), referred to as "Split" was similar to the first one, but paraffin layers at 5, 10, and 15 cm height were established to interrupt soil water redistribution. This method was adopted from Drew (1975), who showed that root growth was unaffected by such layers. Both experiments were conducted consecutively, which explains the differences in the two setups.

Experimental setup

"NoSplit" (without paraffin layers)

The porous substrate was prepared by mixing quartz particles of different size classes, consisting of 85 % sand, 10 % silt, and 5 % clay (Vetterlein et al., 2007). Additionally 50 g kg^{-1} of gravel (2-3 mm Ø) and 20 g kg^{-1} of plastic beads (polypropylene, 2-3 mm Ø) were added to the substrate as internal reference for digital image analysis.

PVC cylinders (inner Ø = 12.5 cm, h = 21.5 cm) were filled up with the substrate by passing it through two sieves of 4 mm mesh size separated by a distance of 10 cm. This procedure was chosen to avoid particle size separation during filling. Resulting bulk density of the substrate was 1.52 ± 0.01 g cm^{-3}. The cylinders had porous plates at the lower end (Figure 3.1A), which were connected with plastic tubing to a water source. The soil was gently watered with a nutrient solution (modified from Römheld and Marschner (1990)) by capillary rise from the bottom of the sample (soil water potential $\psi = 0$ hPa at z = -21.5 cm). Average volumetric soil water content (θ) at the start of the experiment was 31.1 ± 1 %. *Vicia faba* seeds were surface sterilized in 10 % H$_2$O$_2$ solution for 10 minutes, thoroughly rinsed in deionized water and subsequently imbibed for one hour in a saturated CaSO$_4$ solution. Seeds were placed on wet blotting paper and placed in a dark cabinet at room temperature for 2 days. For each cylinder, one pre-germinated seed was carefully placed in a prepared cavity in the soil at a depth of 1 cm. The soil surface was covered by a 2 cm layer of fine quartz gravel. Until shoot emergence

columns were covered with aluminium foil to further minimize evaporation. With the removal of aluminium foil the drying period was initiated (Day 6).
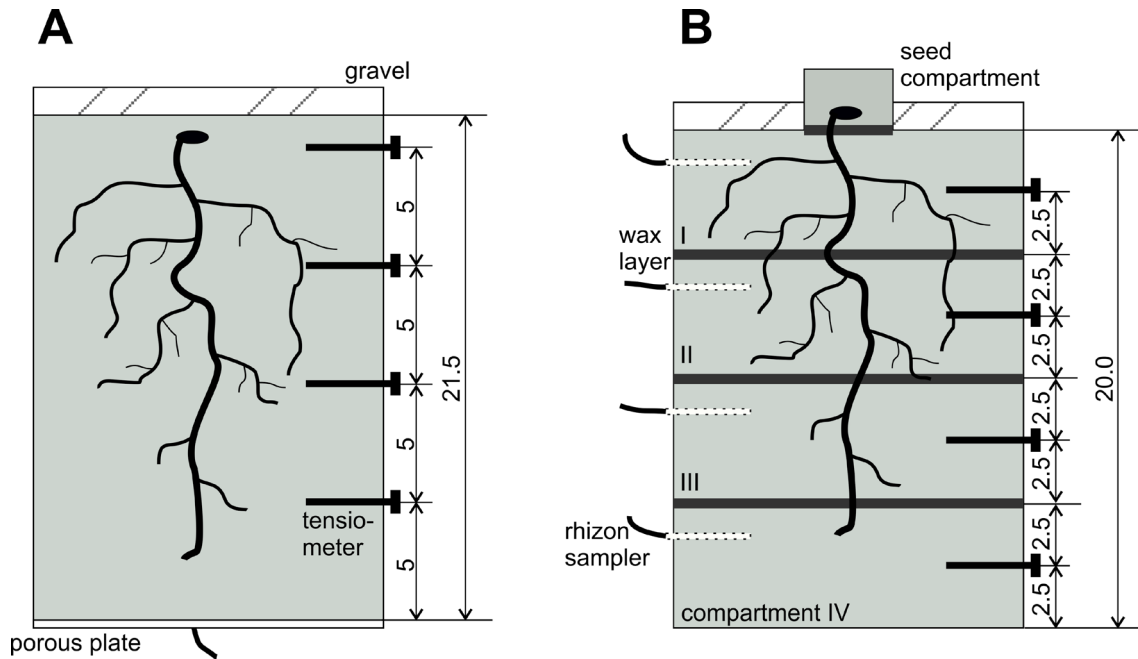

Figure 3.1: Schematic view of the experimental setup with locations for tensiometers and paraffin layers. A) NoSplit setup B) Split setup. All dimensions are given in cm

"Split" (with paraffin layers)

The substrate was the same as in the "NoSplit" experiment, however, without the addition of plastic beads as these caused problems in the segmentation procedure (see below). Soil bulk density was slightly higher ($\Delta = 0.12$ g cm⁻³). For the split layers, molten paraffin was casted and flattened to a thickness of approximately 0.5 mm and cut into a circular shape. At -5, -10, and -15 cm depth a layer of paraffin was placed on top of the soil and sealed to the cylinder walls using molten paraffin (Figure 1 (B)). For initial irrigation, we placed rhizon soil moisture samplers (Eikelkamp, Giesbeek, NL) in each soil compartment. Those were connected over night to bottles filled with 150 ml nutrient solution each. Volumetric water content at the start of the experiment was 23.8 ± 0.5 % in each compartment. Seed preparation was the same as in the "NoSplit" experiment. To avoid the formation of cracks in the soil due to the placement of large *Vicia faba* seeds, these were planted in a separate seed compartment: a cylinder ($\varnothing = 6$ cm, h = 3 cm) filled with the soil mixture and 20 ml of water. When the roots emerged through the paraffin layer at the bottom of the seed compartment, the small cylinder was placed on the topsoil (Day 0). The remaining bare topsoil was covered with gravel to reduce evaporation. The split samples were initially also covered with aluminium foil, which was removed on Day 4 to start the drying period.

Transpiration and soil matric potential

The PVC cylinders were placed on weighing cells (KERN 572, Kern & Sohn GmbH, Balingen, Germany), and grown for 30-36 days with no additional watering. Weight data were recorded every 10 minutes throughout the experimental period. Four micro-tensiometers (Vetterlein et al., 1993) were inserted horizontally through sealed boreholes ("NoSplit": -1.5, -6.5, -11.5, and -16.5 cm soil depth; "Split": -2.5, -7.5, -12.5, -17.5 cm, Figure 3.1) to monitor the soil matric potential (ψ_m), during drying.

The daily transpiration rate was calculated from weight differences between two subsequent days. Evaporation was assumed to be negligible due to the layer of coarse gravel on the surface and as surface was never rewetted during the experiment. Relative humidity was constant day and night hence dew formation could also be excluded. Only on the seed compartment used in "Split" experiment, there was no gravel layer and hence water applied initially (20 ml) was assumed to be lost by evaporation uniformly within the first 7 days.

Leaf area development was estimated by daily measuring the length and width of the lamina of each leaflet and using the linear model of Peksen (2007)

$$LA = 0.919 + 0.682 \, L \cdot W \qquad (3.1)$$

where LA [cm²] is the one-sided leaf area, L [cm] is the length of the lamina, and W [cm] is the width of the lamina. After harvest, we used a flatbed scanner to measure leaf area. The results agreed well with the estimation using Peksen's model. Stomatal conductance was measured at the end of each day using a steady-state porometer (SC-1 Leaf Porometer, Decagon Devices, Inc., Pullman, WA, USA). Two measurements per plant were taken on the abaxial side of the youngest unfolded leaf pair and the mean value of the two measurements was stored.

CT Scanning and image analysis

All samples from the "NoSplit" and the "Split" experiment were scanned every second day during the night phase with an industrial X-ray micro-CT scanner (X-Tek HMX 225) with a fine focus X-ray tube. The scanning parameters are summarized in Table 3.1. Potential X-ray dose was estimated using the free online tool Rad Pro Dose Calculator (McGinnis 2002-2009). In the "Split" experiment, which had a higher exposure, cumulative dose at the end of the experiment was 4.8 Gy. This is well below the maximum dose (~30 Gy) suggested for plant CT studies by Zappala et al. (2013a). Due to the height of the cylinders separate scans of the upper and the lower part of the sample had to be performed. In the NoSplit setup

the mechanism for attaching the porous plate to the soil cylinder at the bottom required an additional plastic ring for sealing reasons which caused photon starvation at the lower end (7 cm), so that not the entire root system could be imaged.

Table 3.1 X-ray settings used in the different experimental setups

	NoSplit	Split
Voltage [kV]	200	210
Current [μA]	250	500
Number of Projections [-]	800	2000
Exposure time [ms]	200	200
Resolution [μm]	245	277

Although the samples were positioned carefully, images scanned at different times were not perfectly aligned. A manual, feature-based method was used to register the images (see Koebernick et al. 2014). The scans from the upper and lower halves of the samples were combined into a single image. The raw images were filtered with a total variation filter (Rudin et al., 1992) to remove small scale noise while preserving sharp edges. We additionally used a pseudomedian filter (Pratt, 2007) to enhance the contrast between roots and soil and to remove beam hardening artefacts. Roots were segmented from the background using a region growing algorithm, similar to the approach of Kaestner et al. (2006). The algorithm used two thresholds to determine, whether a voxel belongs to the root system. The thresholds were chosen manually based on the histogram and visual inspection of the segmentation results. The images were processed with the freely available software QtQuantim (www.quantim.ufz.de). A more detailed description of the technical procedure can be found in Koebernick et al. (2014). In the NoSplit experiment, two samples (NoSplit 1 and NoSplit 3) could not be successfully segmented due to technical difficulties. Due to improved scanning conditions for the Split setup all architectures could be segmented. The segmented images of the root systems are shown in Figure 3.2A. These images contained a number of misclassified voxels (e.g. wall material, paraffin layers, cracks, tensiometers) and roots were disconnected at some points.
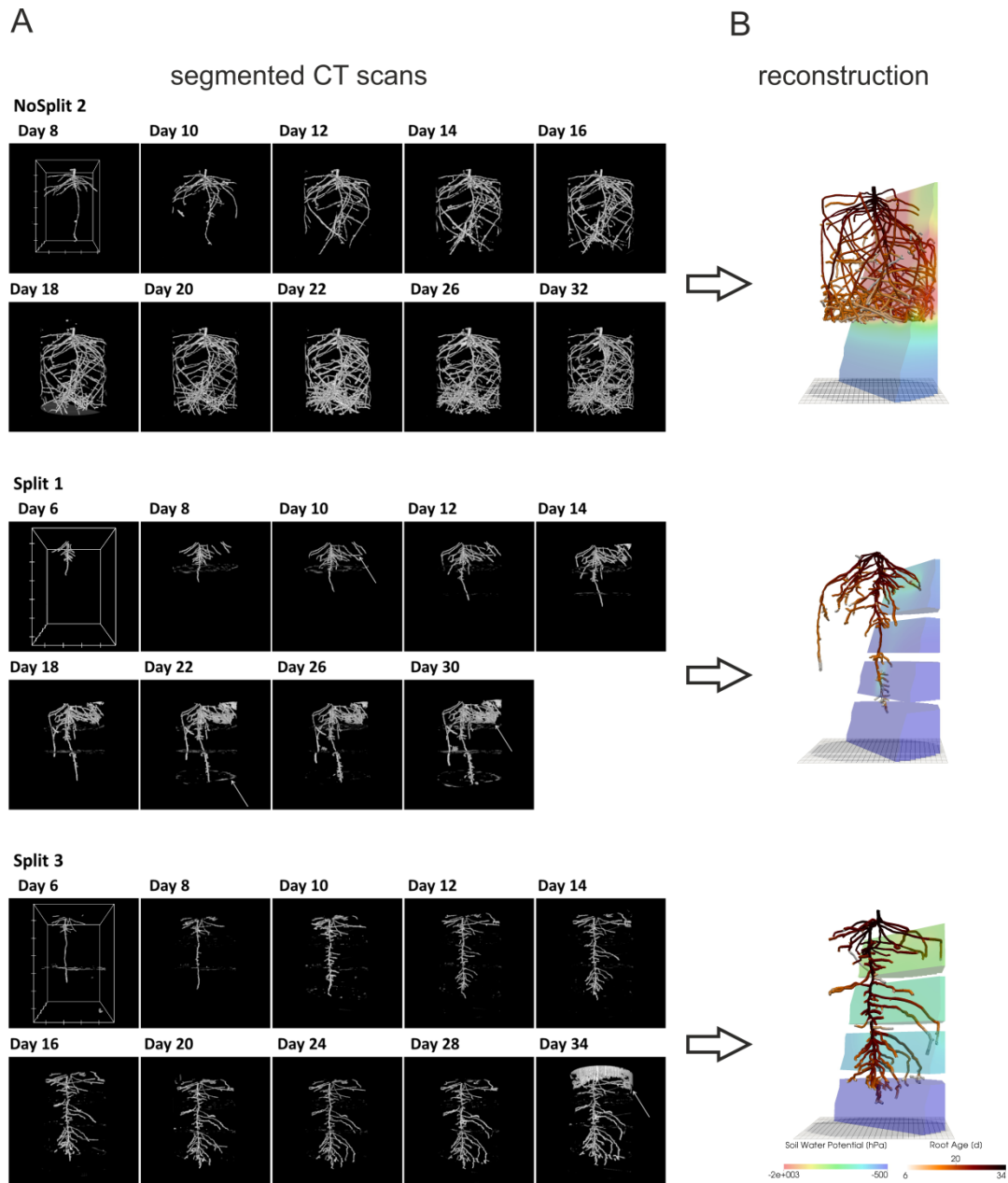
Figure 3.2: A) Three dimensional rendered view of the segmented CT images at different scan times. White arrows indicate misclassified objects: NoSplit 2, Day 8: plastic bead Split 1, Day 10: tensiometer, Day 22: paraffin layer, Day 30 soil crack. Split 3, Day 34: container wall. White boxes at Day 8 or 6 show the scaling of the root system: the distance between two ticks equals 100 pixels, which equals 2.45 cm for NoSplit2 and 2.77 cm for the Split setups B) VR reconstructions of root system architectures at the end of each experiment within their respective soil Root systems are colored according to root age and the soil according to the simulated soil water potential

For the subsequent simulations, a connected root structure was required. Thus, the binary images had to be manually reconstructed using a three-dimensional

46

virtual reality system, which was initially developed to reconstruct MRI data but can be used for any binarized images (for a detailed description of this method see Stingaciu et al. (2013)). Due to the labor-intensive manual reconstruction only two replications of the "Split" (Split 1 and Split 3) experiment were reconstructed. We chose Split 1 and Split 3 because these cover the contrasting root architectures in the "Split" experiment. Misclassified regions in the binarized CT images could be excluded by this manual procedure.

For the determination of root age of each segment at each time step, the reconstructed and stored root system of the precedent scan was opened simultaneously with the image of the subsequent scan. Using the overlay of both scans newly grown roots could be identified and added to the existing root structure. The temporal resolution of the growing root architecture was limited by the time interval between two CT scans (2 days). To obtain smoother root growth, the origination time t_s of a segment s that grew between times t_i and t_{i+1} when a CT scan was made, was calculated using Equation 3.2:

$$t_s = t_i + \frac{l_s}{\Delta l_s}(t_{i+1} - t_i)$$

(3.2)

where Δl_s [L] is the length of all segments that grew between time t_i [T] and t_{i+1} and that are connected to the same connection point of the root system at time t_i as the root segment s, and l_s is the length of all segments that are closer to the connection point than segment s and therefore should have emerged before segment s. The average length of one manually reconstructed root segment was 0.087 ± 0.008 cm.

Destructive measurements

At the end of the experiment (Day 31-35) roots were extracted from the soil by washing using sieves of 3 and 2 mm mesh size successively. In the "Split" experiment, compartments were analyzed separately. In the "NoSplit" experiment, the roots grown into the lower 7 cm of the cylinder that could not be imaged were harvested separately. Roots were stored in Rotisol and subsequently scanned on a flatbed scanner (EPSON Perfection V700 PHOTO). The images were analyzed with WinRHIZO 2009b (Regent Instruments, Inc., Quebec, Canada) to obtain total root lengths.

3.3.2   Modeling of RWU

For the simulation of RWU we used the numerical model R-SWMS, which solves the water flow equation in the root network and in the soil (Javaux et al., 2008). The numerical solution of the Richards equation (Equation 3.3, Richards (1931)) with a sink term S based on SWMS_3D (Simunek et al., 1995).

The water flow equation for the root network is solved based on the radial and axial flow equations (Equations 3.4, 3.5) and the mass balance at each root node, resulting in a system of linear equations for ψ_x, the xylem water potential (Doussan et al., 1998a). The system is solved with a biconjugated gradient method.

The root and the soil water flow equations are coupled through the definition of the sink term of the Richards equation and of the water potential at the soil-root interface for the Doussan equation. The sink term of the Richards equation is defined as the sum of the radial root flow into all root segments, k, located within a soil voxel (cuboid), i, divided by the cuboid volume (Equation 3.6). The soil-root interface water potential at each root node is defined as the distance weighted average of the water potential at the soil voxel nodes.

$$\frac{\partial \theta}{\partial t} = \nabla \cdot [K(\psi)\nabla(\psi)] + \frac{\partial K(\psi)}{\partial z} + S(x, y, z, t) \tag{3.3}$$

$$J_r = K_r^* A_r (\psi_{s,int} - \psi_x) \tag{3.4}$$

$$J_x = -K_x^* A_x \left(\frac{d\psi_x}{dl} + \frac{dz}{dl}\right) \tag{3.5}$$

$$S_i = \frac{\sum_{k=1}^{n_k} J_r^k}{V_j} \tag{3.6}$$

where θ [L^3 L^{-3}] is the volumetric water content of the soil, K [L T^{-1}] the soil hydraulic conductivity, ψ [P] the soil matric potential, and z [P] the gravitational potential. S [L^3 T^{-1}] is the sink term, J_r [L^3 T^{-1}] the radial flow into the roots, J_x [L^3 T^{-1}] the axial flow in the root xylem, K_r^* [L T^{-1} P^{-1}] is the radial conductivity, K_x^* [L^2 T^{-1} P^{-1}] the axial conductivity, $\psi_{s,int}$ [P] is the water potential at the root-soil

48

interface and ψ_x [P] the xylem water potential, A_r and A_x [L²] are the lateral surface and the cross sectional areas of a root segment, l [L] is the length of a root segment. The axial conductance, $K_x = K^*_x A_x$ [L⁴ T⁻¹ P⁻¹]. The indices i and k stand for discrete soil voxels and root segments, respectively. V_j [L³] is the volume of a single soil voxel.

The equivalent hydraulic conductivity of the root system, K_{root} [L³ P⁻¹ T⁻¹], is defined by the relation between actual transpiration, T_{act} [L³ T⁻¹] and the difference between the effective soil water potential and the root collar potential (Javaux et al., 2013)

$$T_{act} = K_{root}\left(\psi_{s,eff} - \psi_{collar}\right) \tag{3.7}$$

$$\psi_{s,eff} = \sum_j SUF_j \psi_{s,int} \tag{3.8}$$

where $\psi_{s,eff}$ [P] is the effective soil water potential, which is weighted by the standard uptake fraction, SUF_j [-]. SUF_j represents the relative water uptake by a root segment j in a soil profile with a uniform soil water water potential and can be derived by solving the Doussan equations. A more detailed explanation can be found in Couvreur et al. (2012).

The R-SWMS code and a manual as well as the reconstructed root architectural files are available upon request from the authors.

Model setup

The samples NoSplit 2 from "NoSplit" experiment and Split 1 and Split 3 from "Split" experiment, with fully reconstructed root architectures, were used for the setup of virtual experiments in R-SWMS. In the following when referring to modeling data names of samples will be written in italics.

Soil domain

We defined rectangular domains with a discretization of 0.5 x 0.5 x 0.25 cm³. The domain size was 14 x 14 x 21.5 cm³ for the "NoSplit" experiment. The domains of the "Split" experiment differed in the z-direction (z=20 cm for Split 1; z=20.25 cm for Split 3, Figure 3.2B). The cylindrical geometry of the soil columns was approximated using Pythagoras' Theorem with a cylinder radius of 7 cm. Voxels belonging to this cylinder were defined as soil material; voxels on the outside were

defined as wall material. The water retention characteristic was described by a bimodal Mualem - van Genuchten expression (Durner, 1994; Van Genuchten, 1980). The soil hydraulic parameters in Table 3.2 were derived from separate HyProp measurements (Peters and Durner, 2008), except the saturated hydraulic conductivity, K_s, which was predicted using the Rosetta tool (Schaap et al., 2001). Paraffin layers were defined as 0.5 cm thick layers within the cylinder. The modeled layer thickness is thus 10 times larger than the thickness of the split layer in the experiment. However, to achieve a reasonable simulation speed, we had to settle for this trade-off. The split layer material was defined equal to the wall material. However, as a certain leakiness of the split layers became obvious during the time course of the experiment and later on during the modeling, we decided to simulate the leakage by assigning a small hydraulic conductivity to the layers of concern. All soil boundary conditions were defined as zero flux. Initial conditions were defined according to the initial water content at the start of the drying period in the experiments. In the "NoSplit" setup soil matric potential was at hydrostatic equilibrium and in the Split setup, soil water content was equal in each compartment.

Table 3.2: Soil hydraulic parameters for the Mualem-van Genuchten expression. Saturated and residual water content, θ_s and θ_r, respectively; van Genuchten shape parameters, α and n; pore connectivity parameter λ; and saturated hydraulic conductivity, Ks. For the soil, a bimodal $\theta(\psi)$ relation (Durner, 1994) was used.

Material	θ_r [cm^3 cm^{-3}]	θ_s [cm^3 cm^{-3}]	α [hPa^{-1}]	n	w2	$\alpha2$ [hPa^{-1}]	n2	λ	K_s [cm d^{-1}]
Soil	0.01	0.35	0.05	4	0.35	0.0033	1.3	0.5	170
Wall	0.01	0.35	0.000003	1.5	-	-	-	0.5	0
Paraffin split / semi*	0.01	0.35	0.000003	1.5	-	-	-	0.5	0 / 0.001*

* denotes the parameterization for the *SC* scenario

Root architecture

The root architectures for the simulations were obtained from the manually reconstructed CT images. Root hydraulic properties were based on an age dependent parameter set by Doussan et al. (2006) for *Lupinus angustifolius* (Figure 3.3, bold lines). Radial conductivity of roots was given a constant value of 8.64×10^{-4} cm d^{-1} hPa^{-1}. The axial conductances increased stepwise with segment age. In Doussan et al. (2006) axial conductance (i.e. xylem conductance) of lateral roots increased with age, whereas taproot axial conductance increased with distance

to the tip. Thus for the tap root we had to convert our age information to distance information. For this we divided the given distances by the mean measured elongation rate of the taproot (0.7 cm d⁻¹) to translate the given distances to the according ages.

At a given simulation time only the root segments with an origination time smaller than the actual simulation time were taken into account. The root system was updated at each further run-time step thus enabling predefined root growth over time. We converted the measured daily transpiration rates of each sample to a periodic step function with zero flow during the night and so defined the root flow boundary conditions in the model at the root collar.
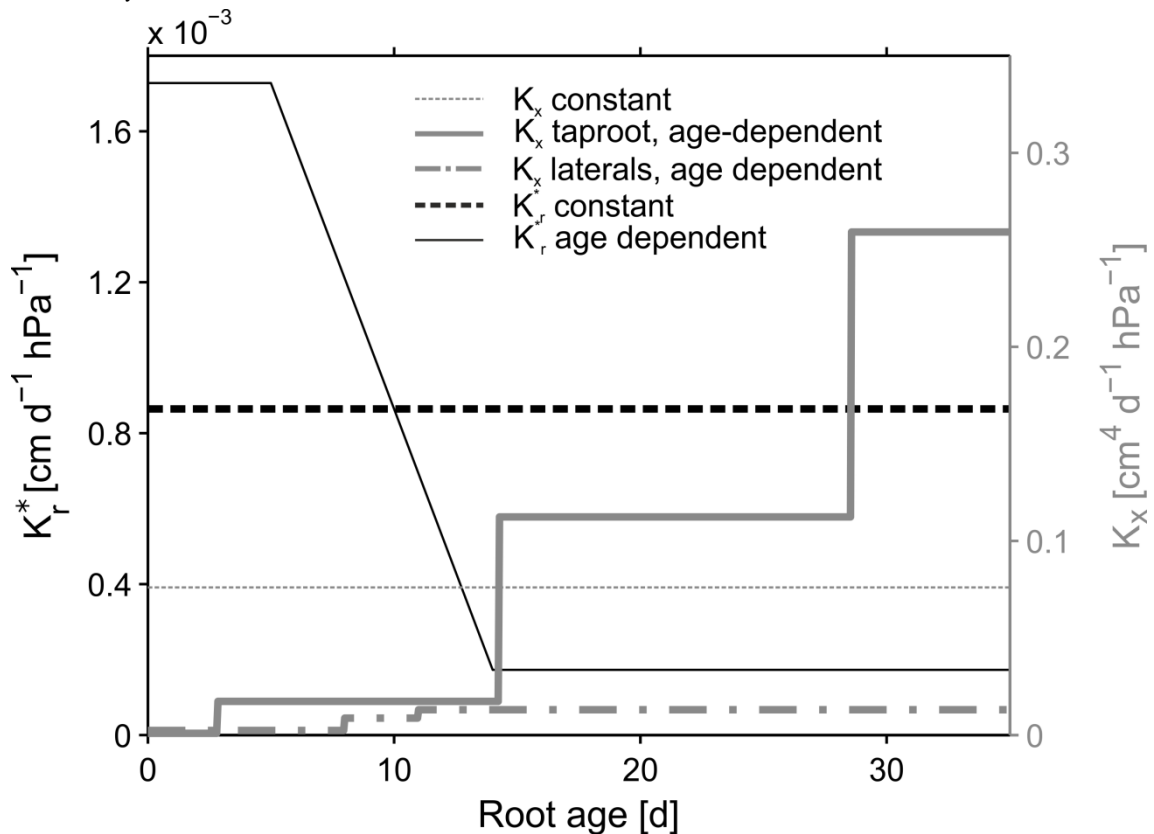
Figure 3.3: Root hydraulic conductivities. Reference parameterization is depicted in bold lines. Age dependent radial conductivity is equal for both, the taproot and laterals. Constant values were kept constant over root type and age

Scenarios

Each of the three samples was exposed to two or three scenarios to analyze the effect of paraffin layers on RWU. In the first scenario *(CD)*, a continuous soil domain without any split layers was used. In the second scenario *(NC)*, we defined three non-conductive paraffin layers. Finally, the third scenario *(SC)*, aimed to achieve best agreement to measured data for the "Split" experiment by considering leaking paraffin layers and assigning a low hydraulic conductivity of 0.001 cm d⁻¹ (Table 3.2) to the split layers. Sample Split 1 was simulated with three slightly

conductive layers, and Split 3 with a non-conductive layer at -5 cm and two remaining slightly conductive layers.

A sensitivity analysis was performed to evaluate the uncertainties in the modeling approach due to uncertain age dependent root hydraulic conductivities. We focus on predawn water potentials, ψ_{pd}, since simulated soil water potentials could be compared with measurements and transpiration rates were used as boundary conditions. Equation 3.7 shows that in case of zero transpiration, e.g. during night, $\psi_{s,eff} = \psi_{collar}$. Thus, predawn water potential is independent of K_{root} and *SUF* can be used as an indicator for the impact of different root hydraulic conductivities on ψ_{pd}. Since *SUF* represents the water uptake by a root segment, relative to the total of the uptake of the root system, *SUF* does not depend on the absolute (radial and axial) conductivities of the root segment but on the ratios between the conductivities of one segment to other segments.

The variability of *SUF* induced by different age dependencies of the hydraulic parameters was examined by comparing different combinations of age dependent and constant axial and radial conductivities for the different reconstructed root architectures (NoSplit2, Split1, Split3) at the end of the growth period. The constant value for K_x was defined as the arithmetic mean of the age dependent K_x values and age-dependent K^*_r values were modified from Doussan et al. (1998b) who defined age-dependent K^*_r values for *Zea mays L.* (Figure 3.3). An overview of the parameterization is given in Table 3.3.

Table 3.3 Perturbations of root hydraulic conductivities from Figure 3 for the sensitivity analysis

	K^*_r	K_x
Reference	constant	age dependent
1	constant	constant
2	age dependent	constant
3	age dependent	age dependent

3.4   Results

3.4.1   Experimental results

As expected, plant performance differed markedly between the two experiments (Figure 3.4). In the "NoSplit" experiment plants were bigger and had a larger leaf area (Figure 3.4A). Leaf growth was initially the same in both experiments, but after Day 15 leaf area increased more in the "NoSplit" experiment. A similar pattern could be observed for total root lengths obtained from CT images over time (Figure 3.4C). Root elongation was similar for both, "Split" and "NoSplit" experiment until Day 10. Afterwards elongation rate was higher for "NoSplit". Root length estimations from destructively harvested roots using WinRHIZO were on average higher than estimations from CT (Table 3.4).
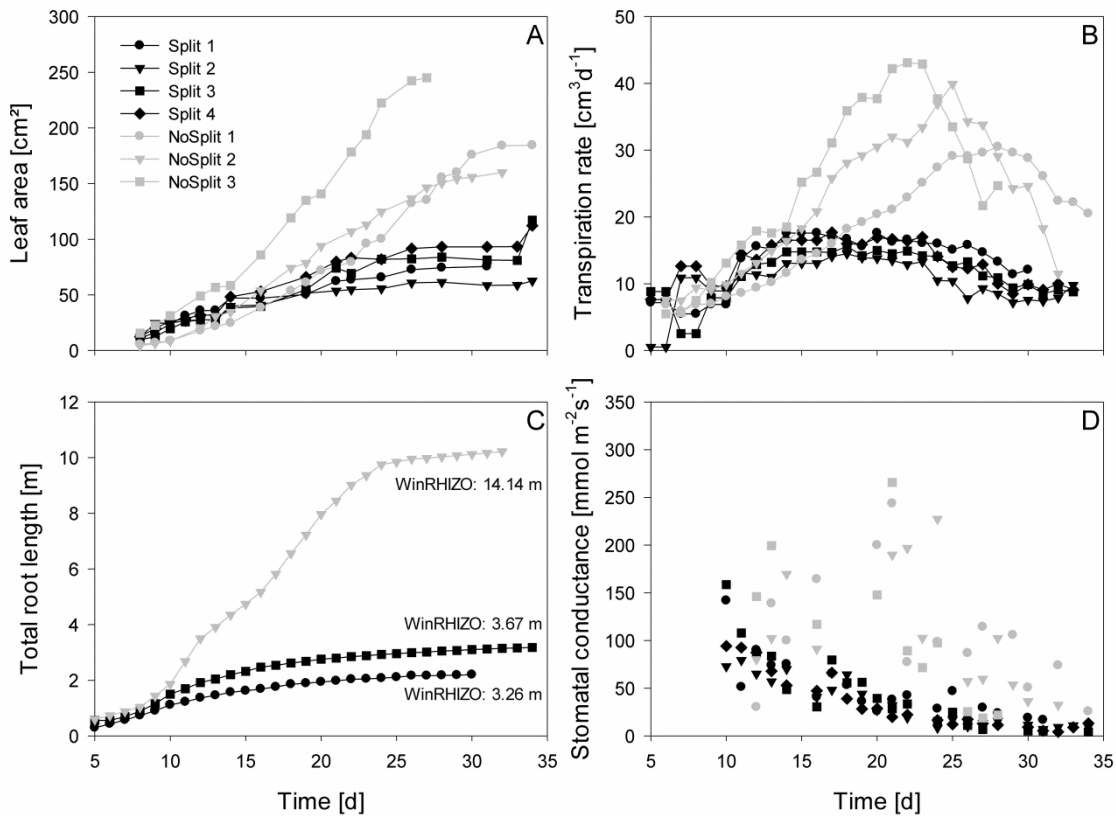
Figure 3.4: Measured plant traits over time from Day 5 / 10 until Day 35. Gray symbols represent the NoSplit setup and black symbols the Split setup. Different symbols represent replications. A) One-sided leaf area B) Evapotranspiration rate C) total estimated root length of the samples used for modeling D) stomatal conductance of the youngest unfolded leaves, data points represent the mean of two measurements

The vertical root length distribution in the "Split" experiment differed between Split 1 and the remaining samples. Compartment I in Split 1 contained about 3/4 of the total root length, while the distribution for the other replications of

the "Split" experiment was more even (Table 3.4). In the "NoSplit" experiment root density increased with depth.

Table 3.4 Root length estimations from CT images and from destructive measurements at the end of each experiment

		Length CT [cm]	Length WinRhizo [cm]	(WinRhizo -CT)/WinRhizo [-]
NoSplit 1		-	*1504*	-
NoSplit 2		*1022*	*1414*	*0.27*
NoSplit 3		-	*2023*	-
Split 1	*Total*	*270*	*326*	*0.17*
	Comp. I	196	240	0.18
	Comp. II	44	48	0.08
	Comp. III	20	27	0.26
	Comp. IV	10	11	0.10
Split 2	*Total*	-	*335*	-
	Comp. I	-	79	-
	Comp. II	-	213*	-
	Comp. III	-		-
	Comp. IV	-	43	-
Split 3	*Total*	*319*	*368*	*0.13*
	Comp. I	126	132	0.05
	Comp. II	64	69	0.07
	Comp. III	90	125	0.28
	Comp. IV	38	41	0.07
Split 4	*Total*	-	*573*	-
	Comp. I	-	143	-
	Comp. II	-	234	-
	Comp. III	-	158	-
	Comp. IV	-	38	-

* Values for Compartment II and III combined

In both experiments transpiration rate initially increased with leaf area (Figure 3.4B). In "NoSplit" a sharp decrease in transpiration rate was seen at Days 23, 25, and 28, respectively for the different samples. Transpiration reduction occurred earliest in NoSplit 3, which was also the largest plant with the highest transpiration rate up to that day. In the "Split" experiment, transpiration reduction

could be observed earlier, although the reduction in transpiration was not as strong as in the "NoSplit" experiments. The lower leaf areas and smaller transpiration rates in the "Split" experiment were accompanied by lower stomatal conductance of the youngest unfolded leaves in comparison to the "NoSplit" experiments (Figure 3.4D). Stomatal conductance decreased already from the first measurement, i.e. Day 10, in the "Split" experiment. In the "NoSplit" experiment the variability of stomatal conductance in the different samples was very high, but low values were not measured until Days 23 or 24, respectively.

Water depletion from each compartment was calculated from measured tensiometer values assuming a uniform matric potential within a layer and using the substrate specific water retention curve (Table 3.2). These data were compared to total water loss derived from weighing cells (Figure 3.6). When air bubbles started to form in the tensiometers no further water content change could be calculated. The calculated water content at this point was between 9.5 and 10.6% (ψ_m = -745 to -431 hPa). In the "NoSplit" setup (Figure 3.6A) there were no true compartments, we therefore assumed that the tensiometers represented the matric potential for the surrounding volume closest to the tensiometer. While the difference between calculated and measured cumulative water depletion for the "Split" setup (Figure 3.6B-C) converged to below 10 % (+9 % Split 3, -5 % Split 1) at the end of the experiment, it was much higher (17 %) in the "NoSplit" setup. Comparison of the slopes over time indicates a poor fit of the dynamics. Calculated water depletion was clearly overestimated at the beginning and underestimated towards the end of the experiments, especially in Split 3. The arrival of roots in Compartments III and IV in Split 1 was at Day 12 and 18, respectively, nonetheless there was significant (even if overestimated) water depletion from both compartments before these dates.

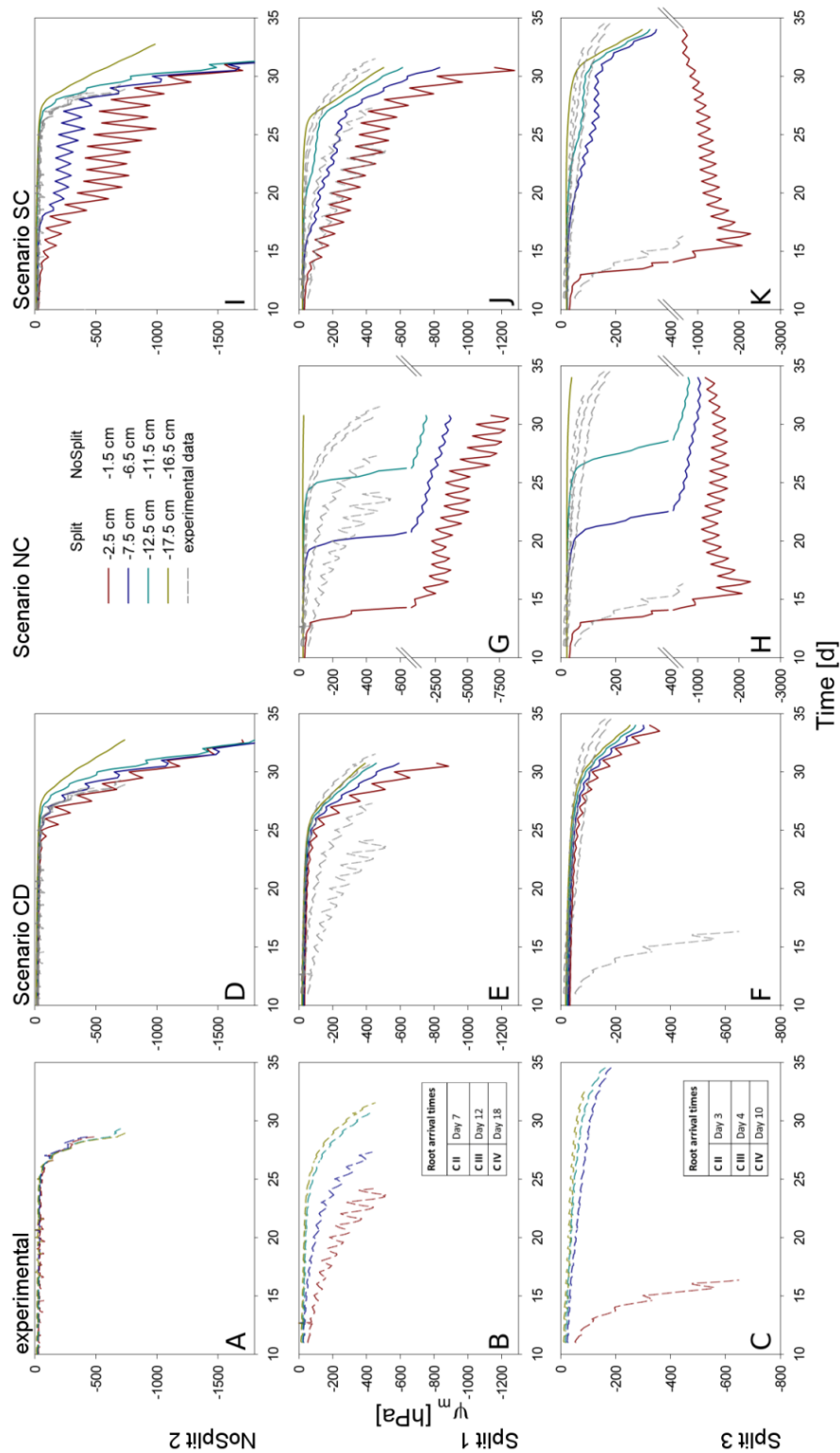*Figure 3.5: Soil matric potentials for the three samples (top to bottom) within the different compartments. A) – C) Values measured by the tensiometers in the experiments D) – K) Comparison of different scenarios with the measured values, repeated in dashed, gray lines D) – F) Simulation CD – unrestricted, continuous soil domain G) – H) Simulation NC – impermeable, non-conductive layers I) – K) Simulation SC – semi-conductive layers*
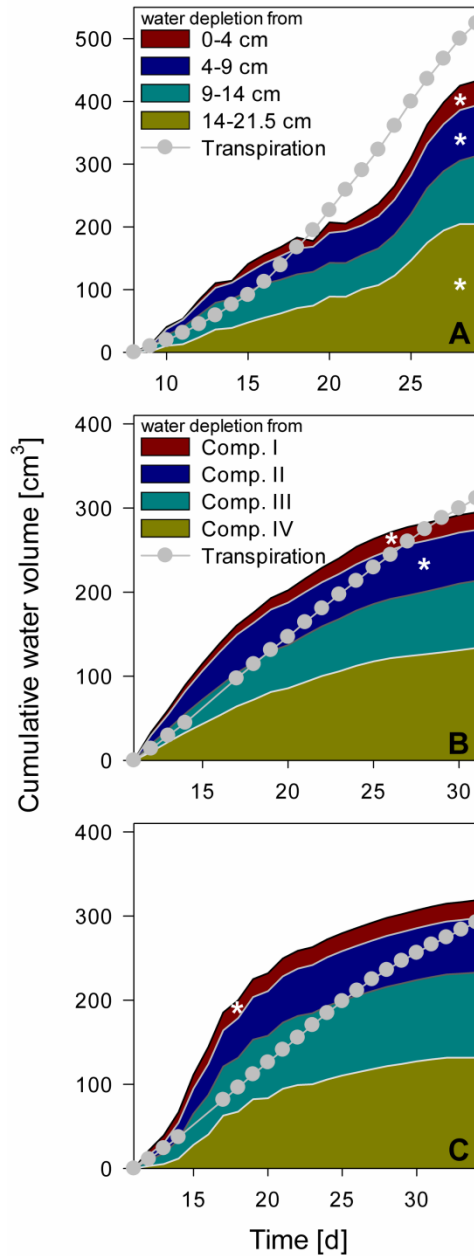
Figure 3.6: Cumulative water depletion from each compartment over time compared to cumulative transpiration from Day 8 for NoSplit (A) and Day 11 for Split 1 (B) and Split 3 (C) until the end of the experiment. Filled areas represent cumulative water content change in the different compartments calculated from tensiometer measurements. Gray line and circles represent cumulative transpiration measured with balances. White asterisks denote the point, when the tensiometer in the compartment showed air bubbles

3.4.2 Simulation results

The three samples (NoSplit 2, Split 1 and Split 3) representing different RSA were subjected to three different scenarios: (*CD*), a continuous, unrestricted soil domain, (*NC*) a soil domain with non-conductive split layers, and (*SC*) with semi-

conductive split layers. Mean simulated soil matric potentials in four layers were compared to the measured tensiometer values (Figure 3.5).

Choice of scenario

In scenario *(CD)* (continuous soil domain) (Figure 3.5D – F), the simulated matric potentials in the different soil layers started declining strongly and nearly simultaneously only towards the end of the simulation period. The simulated decline occurred the earliest and was the strongest in the "NoSplit" experiment reflecting the larger cumulative transpiration from this experiment.

For the "NoSplit" experiment, the simulated matric potentials for scenario *(CD)* showed a similar behavior as the measurements (Figure 3.5D). The timing and the slope of decrease fitted the experimental data well. The lowest tensiometer (-16.5 cm) was an exception, probably due to the fact that the deep roots could not be detected in the CT and were missing in the model.

For both samples of the "Split" experiment (Figure 3.5E, F), the measured matric potentials of the upper two tensiometers started decreasing much earlier than the simulated matric potentials for scenario *(CD)*. This illustrates the effect of the paraffin layers on the soil water distribution in the "Split" experiment which is ignored in scenario *(CD)*.

Scenario *(NC)* with non-conductive paraffin layers was simulated only for the "Split" experiments (Figure 3.5G, H). The simulated matric potentials at the tensiometer depths decreased sequentially from top to bottom and the time lag between these decreases was much larger than in scenario *(CD)* for the same samples. The simulated water potentials started to decrease shortly after roots arrived in a compartment. In Split 3 (Figure 3.5H), simulated average water potential in Compartment I decreased to about -2000 hPa until Day 15 and remained at this level thereafter only showing pronounced diurnal fluctuations until the end of the simulation run. In both samples of the "Split" experiment (Figure 3.5G, H) for scenario *(NC)* the simulated changes in water potential in Compartment IV were very small due to the small fraction of roots in this compartment.

With Scenario *(NC)* we were not able to reproduce the measured dynamics of soil matric potentials of the "Split" samples. Measured matric potentials did not show a sequential stepwise decrease but a more gradual decrease that started earlier than the simulated decrease and sometimes even earlier than the root arrival time in a compartment. One exception was the matric potential in Compartment I of the Split 3 sample. Scenario *(NC)* produced large water potential differences between the different compartments, which were not in agreement with the measurements.

The previously described results indicate that paraffin layers were not perfectly isolating, but that there must have been water redistribution between

neighboring compartments, albeit at a lower rate than in completely unrestricted soil. Thus, scenario *(SC)* was applied.

For Sample Split 1 in scenario *(SC)* (Figure 3.5J), the simulated matric potentials of Compartment I showed a slower decrease than those obtained with scenario *(NC)* or *(CD)*. At the same time scenario *(SC)* resulted in an earlier decrease of matric potential in the lowest compartment compared to scenario *(NC)*. The pronounced measured diurnal pattern of soil matric potential in Compartment I was successfully reproduced in scenario *(SC)*.

Likewise, for Sample Split 3 simulated matric potentials of scenario *(SC)* showed the best agreement with measured tensiometer data. Here the assumption that all layers except the top layer were leaking was important for obtaining the good agreement.

As expected, for the "NoSplit" experiment (Figure 3.5I), agreement between measured soil matric potentials and those simulated with scenario *(SC)* was very poor. However it is interesting to note the influence of, albeit leaking, hydraulic barriers to soil water potentials.

In contrast to experimental approaches, which can only detect changes in soil matric potential, the simulation results allow disentangling the different fluxes which contribute to local changes in matric potential and soil water content. The evaluation of fluxes was restricted to those simulations which showed the best agreement between measured matric potentials and simulated once, i.e. scenario *(CD)* for sample *NoSplit 2*, scenario *(SC)* for samples *Split 1* and *Split 3*.

Simulated flow dynamics

The water balances of the single soil compartments are depicted in Figure 3.7. In case of impermeable split layers, the storage change within one soil compartment should equal root water uptake. However, if the split layers are leaking, which is the case for most of the layers, only adding the net flow through the split layers to the storage change equals root water uptake.

For the *NoSplit 2* (Figure 3.7A) simulation RWU was largest in the upper compartment, where it started to decrease from Day 25 onward. The 5-10 cm layer only started to significantly contribute to RWU from Day 17 onward and the 10-20 cm layer only after Day 20, which is related to root arrival time.

It is interesting to note that "early morning values" of RWU in the 0-5 cm layer remained higher than those in the other layers even after 25 days i.e. during a period where overall contribution of the lower layers to RWU had increased and total transpiration rate was reduced in the experiment.

Simulations showed soil hydraulic redistribution of water from the lower layers to the top 0-5 cm. At 5-10 cm depth inflows from the deepest soil layer and outflows to the 0-5 cm layer were almost of the same magnitude, so the resulting

net flow oscillated around zero. Soil hydraulic redistribution started to decrease after Day 25 and seized after Day 31.
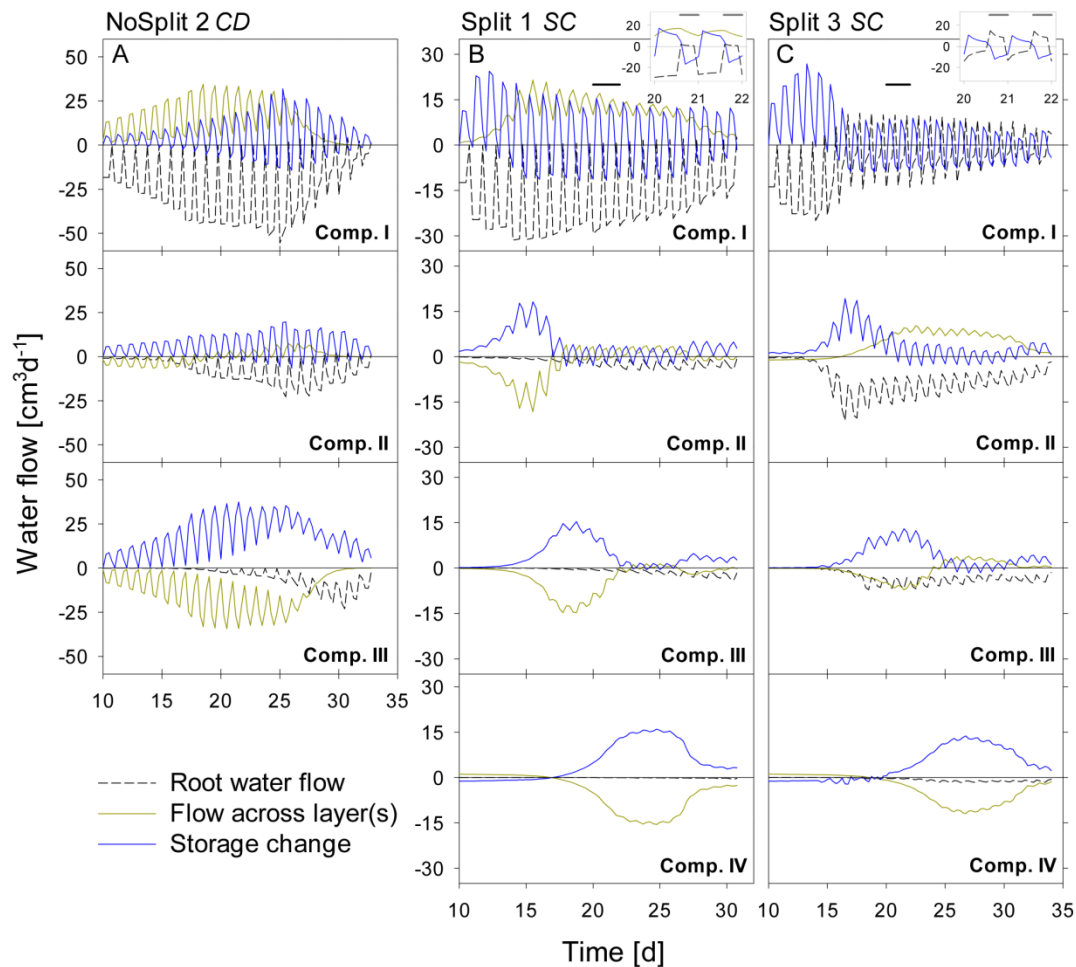

Figure 3.7: Modeled water flow dynamics over time in the A) NoSplit CD, B) Split1 SC, and C) Split 3 SC scenarios. Dashed black lines represent root water flow. Dark yellow lines represent the net flow across the paraffin layers from neighboring compartments. Negative values indicate water removal, positive values water addition to a compartment, respectively. Blue lines represent the resulting change of soil water content in the compartment with positive values denoting a decrease in water storage and negative values and increase in storage. Plotted values are flow rates at four discrete times per day. Because there is only one value for the night phase, flows at night appear as single peaks. The inlays at the top show the dynamics in Compartment I between Days 20-22 (as indicated by the black bars) at a higher temporal resolution (10/d), showing the dynamics of RWU and hydraulic redistribution

Since RWU from a layer corresponds to the sum of the net water flow into and the decrease of the water storage in a soil compartment, it is evident that RWU in a soil layer cannot be derived from water storage changes in that layer. RWU in the 0-5 cm layer is considerably larger than the changes in water storage whereas the opposite is true for the 10 - 15 cm layer. It is clearly visible that RWU and storage

change did not correspond to each other as long as there was significant soil hydraulic redistribution.

Substantial soil hydraulic redistribution occurred also in the samples *Split 1* (*SC*) and *Split 3* (*SC*), although K_s values of paraffin layers were only 0.001 cm d^{-1} (Figure 3.7B, C). In both simulations RWU did not correspond to water storage change with the exception of Compartment I in *Split 3*, which was assumed to be separated by a non-conductive split layer. RWU from Compartment IV was very small in both *Split 1* (*SC*) and *Split 3* (*SC*) while the change in soil water content was substantially higher due to flow across the split layer. The same pattern was observed in Compartment III, but net outflow of water started earlier and was eventually compensated by inflow from Compartment IV. Compartment II showed a contrasting behavior between the two samples of the "Split" experiment. In *Split 3* the non-conductive layer at the top prevented water movement in the soil to Compartment I, and the fraction of RWU from compartment II was considerably higher in *Split 3* than in *Split 1*.

In both simulations of the "Split" experiment, there was significant hydraulic redistribution via deep roots into Compartment I. Root hydraulic redistribution was much more pronounced in *Split 3*. According to the simulations the redistribution via the roots occurred during night and the water was taken up by the roots during the next day.

The comparison of cumulative root water uptake from the different compartments with cumulative water depletion at the end of the simulations highlights the importance of including soil hydraulic redistribution when analyzing the pattern of RWU (Table 3.5). This is most obvious in the unrestricted sample *NoSplit 2,* where 69% of RWU occurred in the 0-5 cm layer, while the water depletion in this layer was only 16% of total water depletion. But even in Compartment I of *Split 3*, which was assumed to be perfectly isolated, RWU and water depletion are slightly different, which is probably due to the discretization of simulation outputs and rounding errors.

Further, the development of the root system architecture (Figure 3.2) can be compared to the water flows within the soil and root system (Figure 3.7). Due to the semipermeable split layers in *Split 1*, most of the RWU takes place in the upmost compartment, the location where also most of the roots are found. In *Split 3,* where the top compartment is hydraulically isolated, the roots take up most of the water from this layer within the first 15 days, while afterwards the uptake shifts to the lower compartments. This pattern is reflected in the RSA development. The *NoSplit* setup shows a more or less smooth shift of roots as well as RWU downward in the domain.

Table 3.5 Total root water uptake and water depletion in each soil compartment at the end of each simulation

Simulation		RWU [cm³]	Water depletion [cm³]
NoSplit 2 CD	*Total*	*660.4*	*657.4*
	Comp. I	456.2	105.8
	Comp. II	124.3	139.6
	Comp. III	79.9	412.0
Split 1 SC	*Total*	*387.7*	*386.7*
	Comp. I	336.8	121.6
	Comp. II	32.2	82.4
	Comp. III	17.2	84.6
	Comp. IV	1.5	98.2
Split 3 SC	*Total*	*358.4*	*358.2*
	Comp. I	101.8	97.8
	Comp. II	175.5	87.8
	Comp. III	66.7	81.9
	Comp. IV	14.4	90.6

Sensitivity analysis

Following Equation 3.8, the effective soil water potential, in case that transpiration is zero, is equal to the water potential at the root soil interface weighed by the standard uptake fraction, *SUF*. The *SUF* was calculated for four different parameterizations of root hydraulic conductivity. Figure 3.8A shows the sum of *SUF* for the NoSplit setup within given soil depth increments. With age-dependent radial conductivity the *SUF* becomes more uniform over depth. For both Split setups the variability with the different parameterizations is not as large (see *Appendix 2, Figure A2.2*).

The SUF, which shows the hydraulic architecture of the root systems, are compared for the three different plants (Figure 3.8B). In contrast to the root system architecture, only small differences can be observed. The differences in predawn water potentials between the different plants were thus mainly due to the soil water distribution and less to RSA.
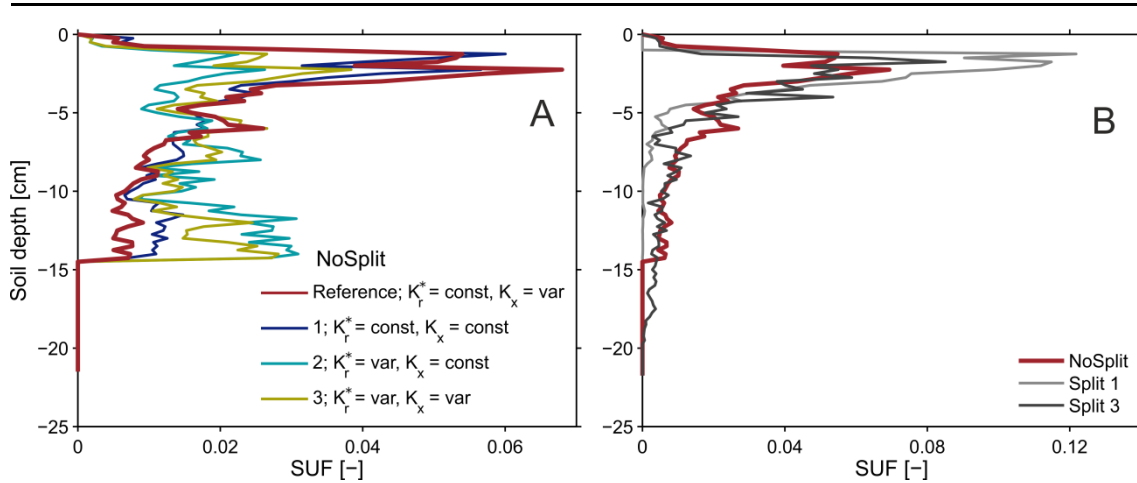
Figure 3.8: Sums of the standard uptake fraction over soil depth increments of 0.25 cm for A) the NoSplit root system at t = 32 days solved for different parameterizations of radial and axial root hydraulic conductivities and B) for the reference parameterization of root hydraulic conductivities for the three different plant architectures. The observed variability for the two split setups was less than shown in subplot A) and is shown in Figure A 2

Pre-dawn water potential at the root collar

Simulated pre-dawn water potential at the root collar (ψ_{pd}) was used as an indicator for plant water status (Figure 3.9). ψ_{pd} is independent of actual transpiration rates and can therefore be used to compare different samples. ψ_{pd} is generally thought to be in equilibrium with the soil water potential provided that night induced interruption of transpiration is long enough and flow rates in soil root systems are high enough to reach this equilibrium (Donovan et al., 2003). However, the soil matric potentials, simulated in this study were clearly not in equilibrium, especially for the two split samples.

In sample *NoSplit 2 (CD)*, simulated predawn ψ_{pd} decreased only slowly until Day 25 and was in equilibrium with soil matric potential in the topsoil (-1.5 cm depth). Due to the homogeneous soil water distribution it was also closely related to the matric potential in the wettest soil accessible to the plant, i.e. the soil at maximum rooting depth at each time step. From Day 25 onwards there was a strong decrease of soil matric potential in the whole column and an according decrease of $\psi_{pd.}$ After Day 30, ψ_{pd} was more negative than the topsoil matric potential. The disequilibrium increased until the end of the experiment. In both split samples ψ_{pd} was more negative than the matric potential at maximum rooting depth but less negative than the topsoil matric potential, indicating that the system did not reach equilibrium at the end of the night. ψ_{pd} in *Split 1 (SC)* was closer to the matric potential in the topsoil, reflecting the higher redistribution through the split layers in *Split 1 (SC)*.
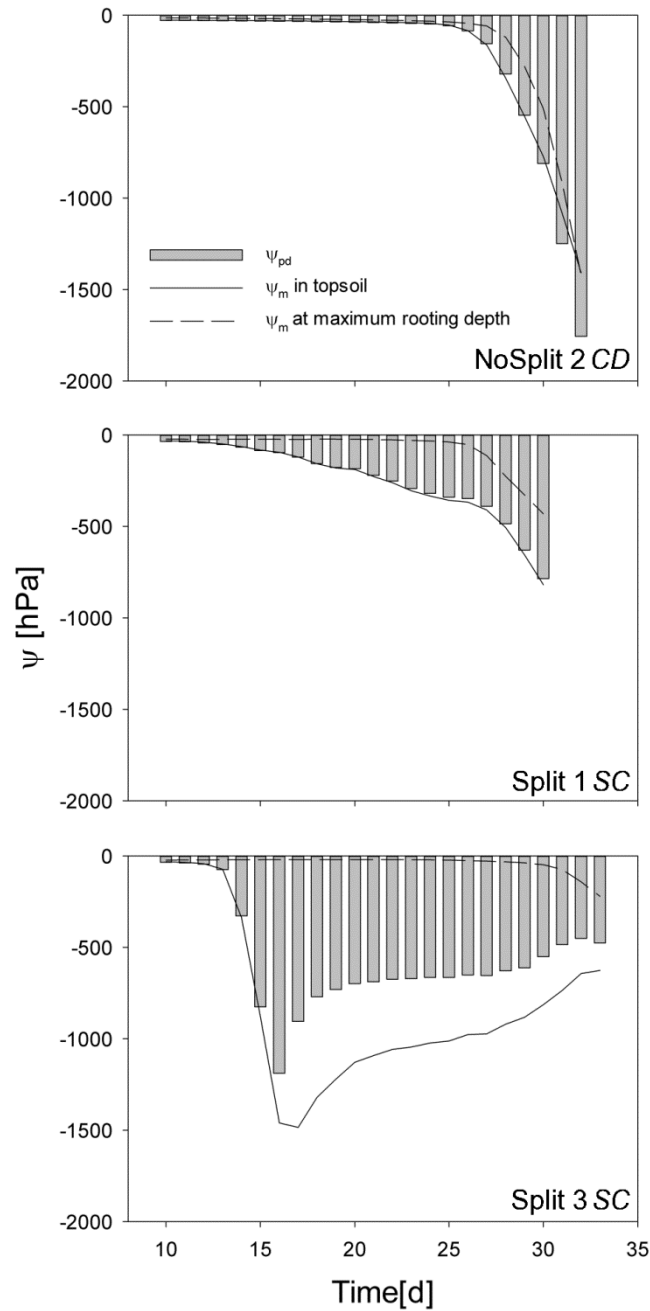
Figure 3.9: Simulated predawn water potential at the root collar (ψ_{collar} gray bars) for A) NoSplit 2 CD B) Split 1 SC and C) Split 3 SC and simulated soil water potentials (ψ_m) at the top 5 cm depth (full line) and at the maximum rooting depth (dashed line) over time

To illustrate the impact of the split layers on soil and thus plant water status, predawn soil water potentials of the different scenarios with and without paraffin layers (*SC* vs. *CD*) for each sample were compared. The difference of absolute soil water potentials for the two contrasting soil environments was calculated ($\Delta|\psi_{pd}| = |\psi_{pd}|_{SC} - |\psi_{pd}|_{CD}$) (Figure 3.10, bold lines). As expected, soil water potential was constantly more negative in scenario *SC* than in scenario *CD*. $\Delta\psi_{pd}$ in

Split 1 and in *NoSplit 2* were of the same magnitude, while in *Split 3*, where the upper paraffin layer was assumed to be non-conductive, it increased more rapidly and stronger, indicating an effect of the higher degree of hydraulic isolation of the different soil layers.

When using the previously calculated *SUF* to determine the impact of parameterization of root hydraulic conductivities on effective soil water potentials, the variability of soil water potentials compared to the plant variability is very small (Figure 3.10, thin lines).
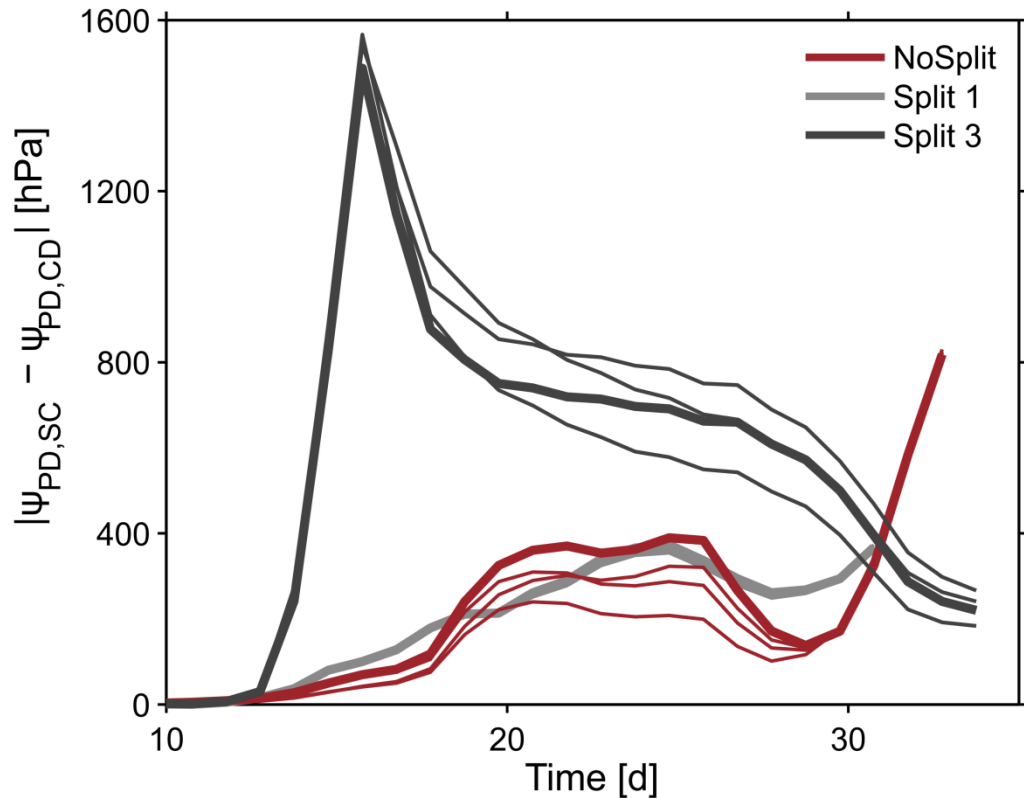

Figure 3.10: Influence of split layers on simulated soil water potentials for the reference parameterization (bold lines) and for the remaining three parameter sets for root hydraulic conductivities (thin lines, Table 3.3). The soil water potential was calculated based on scenarios for uniform distribution of soil water potential (Eq. 8). The four lines overlap in the Split 1 setup

3.5   Discussion

Influence of paraffin layers on plant growth

CT measurements gave insight into the changes of growth behavior caused by the addition of wax layers. However, the causes for these changes are not revealed by the CT measurements. By using a simulation model CT measured RSA and the low (zero) hydraulic conductivity of the wax layer could be linked to internal plant water potentials. This enables an interpretation of plant water stress and its implications for shoot and root growth.

Experimental results as well as simulations suggested strongly that most of the paraffin layers were not perfectly hydraulically isolating. Tomographic images and visual inspection after destructive harvest showed, however, no evidence of cracks or holes in the wax layers. It is possible that there were cracks at the container walls that were formed due to shearing of the paraffin caused by the weight of the soil in the upper compartments. The only paraffin layer that was evidently tight was consequently the uppermost layer in the sample Split 3. Drew (1975) suggested the use of layers as thin as 0.2 mm, which is even thinner than the layers that were used in this study. Another possible source of leakage is linked to diurnal shrinking and swelling of roots (Huck et al., 1970), which could lead to cavities in the paraffin where it is penetrated by roots. This could not be excluded as CT images were scanned during night.

Roots easily penetrated the paraffin and grew into the lower compartments. Taproots and vertically oriented laterals were not affected by paraffin layer. However, a few roots continued to grow horizontally within the soft paraffin layers (see *Appendix 2, Figure A2.3*).

The plants in the "Split" experiment were overall smaller with lower root densities. Inserting split layers generated a substantial resistance to vertical water flow within the soil and hence water redistribution in the soil column. A restriction of this redistribution led to lower simulated predawn root and collar water potentials, which were related to lower measured stomatal conductance. The lower predawn water potentials pointed at plant stress that resulted in a restriction of root and shoot growth. Even though the root-shoot ratio was shown to increase in *Vicia faba* in drier environments (El Nadi et al., 1969), this could not be observed in this experiment. A possible explanation for this is the higher bulk density in the split experiment. Slight increases of soil strength can lead to a substantial reduction of root penetration rate (Taylor et al., 1966). We cannot exclude a possible effect of oxygen depletion on plant performance caused by the addition of paraffin layers, as no oxygen concentrations were measured. However, we feel that hypoxia is highly unlikely: The soil was initially not water saturated and the fact that paraffin layers were permeable to water means that soil air could move as well. The rhizon

samplers were kept in the soil during the experiment as possible pathways for air. The soil mixture was an artificial mixture without added organic matter, so microbial respiration should be minimal. Experiments with the same quartz substrate showed that even close to saturation redox potentials only decreased after adding significant amounts of organic material (Ackermann et al., 2008).

Relation between measured water loss and RWU

The simulations showed the discrepancy between change in soil water content and the location of root water uptake for individual soil compartments, which was caused by soil hydraulic redistribution. Even a small conductivity of the hydraulic barriers led to considerable redistribution of soil water. The direct calculation of soil water content, and in extension RWU, from measured soil matric potentials was further complicated by the non-linear relation between water potential and water content, which precludes the extrapolation of a single tensiometer reading to the total soil compartment without knowing the gradients. The development of gradients around active roots is shown in *Appendix 2, Figure A2.4*.

Even if the vertical soil flow is completely restricted, hydraulic redistribution through the roots might still be a substantial amount of water that is exchanged between the roots and the soil in the drier regions of the root zone. In this case, however, the net water content change should correspond to net root water flow. The share of root hydraulic redistribution was higher when soil water redistribution was restricted by barriers, allowing the formation of a sufficing water potential gradient to drive flow. This may in part explain the controversy in literature as to the ecological relevance of root hydraulic redistribution. Its magnitude spans almost two orders of magnitude and is affected by numerous factors, such as root and water distribution, soil texture, and root-soil hydraulic conductance (Neumann and Cardon, 2012).

Predawn collar potential

Simulation results suggest that predawn collar water potential (ψ_{pd}) cannot be related to the water potential in the wettest part of the root zone, as was previously reported in literature (Hinckley and Bruckerhoff, 1975) (Figure 3.9). When gradients in soil water potential increase ψ_{pd} is closer to the driest part of the root zone as water redistribution in the soil is restricted by low unsaturated hydraulic conductivity. Disequilibrium between plant and soil water potentials was caused by the heterogeneity of soil water potential, as previously experimentally shown by Améglio et al. (1999) and Donovan et al. (2003). Root hydraulic redistribution can contribute to the disequilibrium as the nocturnal water loss prevents the recovery of plant water potential (Donovan et al., 2003). This leads potentially to the

equilibration of the system but is ultimately limited by the soil-root resistance to water flow. The largest redistribution in the model, however, takes place through the leaking split layers (Figure 3.7). For this reason, in *Split 1 (SC)*, where the leakage caused the deeper layers to dry earlier, ψ_{pd} was very close to the potential of the dry topsoil, while in *Split 3 (SC)*, with Compartment I being perfectly hydraulically isolated, ψ_{pd} was between the potentials of the topsoil and the soil at maximum rooting depth.

Determination of RSA with CT

Comparison of destructive WinRhizo scans and CT imaging showed a discrepancy of up to 27 % for total root length between both methods (Table 3.4). Underestimation of root length with CT imaging had several reasons: (i) 3.5 % of total root length had diameters < 0.5 mm. As a diameter of twice the resolution (voxel side length 245 µm and 277 µm, respectively) is required for a safe detection, these roots were possibly missed by CT imaging (Koebernick et al., 2014). (ii) Roots that grow along the cylinder walls are often lost in the course of data processing, when edges of the domain have to be removed. (iii) In the "Split" setup, roots sometimes remained within the soft paraffin layers. These were eventually undetectable with X-ray CT as there is no density contrast between paraffin and roots. (iv) A possible effect of the changing soil moisture content on the segmentation cannot be excluded, since destructive measurements were only available for dry conditions at the end of the experiment. Especially at high soil moisture contents the segmentation of roots can be increasingly difficult (Flavel et al., 2012; Zappala et al., 2013b). Conversely, Lontoc-Roy et al. (2006) had more difficulties segmenting maize roots from loamy sand under dry than under water saturated conditions. Our temporally repeated X-ray CT scans suggests that, for the relatively coarse roots of *Vicia faba* (mean diameter = 1.06 mm), water content did not strongly affect the segmentation results until the end of the experiment, when soil cracks started to form in the upper compartment of Split 1, which prevented the successful segmentation of nearby roots (Figure 3.2A).

Parameterization of root hydraulic conductivity

Information on root hydraulic conductivities is very sparse. The use of the xylem pressure probe to determine axial and radial root hydraulic conductivities is technically very demanding, particularly for soil grown plants. Most applications refer to solution culture studies. The root hydraulic parameters for this study were derived from literature data based on experiments with lupin plants (Doussan et al., 2006) and could not be validated by direct measurements or simulation results. Thus, these parameters are a major source of uncertainty. So far, three major uncertainties could be identified:

1)   The absolute value of the conductance of the root system, K_{root}, and how it differs between plants

This would affect the absolute value of simulated collar water potentials when transpiration takes place but it does not affect the predawn water potential. Thus the conclusion that split layers reduce the collar pre-dawn water potential compared to a case where there are no split layers is not affected. The distribution of the water uptake when the soil water potential is non-uniform in the soil profile is affected by uncertainty in the absolute conductance of the root system. However, the relatively good agreement between simulated and measured soil water potentials indicates that the distribution of the root water uptake was simulated satisfactorily using the chosen (or selected) root conductivities.

2)   The ratio between K_r/K_x

Previous simulation studies have shown that this ratio affects the location of root water uptake (Couvreur et al., 2014). When K_r/K_x is small, root water uptake occurs more uniformly along the root profile, whereas for higher K_r/K_x root water uptake occurs closer to the root collar. In this study we have additional root growth, which affects the location of water uptake. Again, the relative good predictions of the soil water potentials indicate that the root water uptake distribution was simulated quite accurately.

3)   The change of K^*_r and K_x over root segment age

A sensitivity analysis showed that uncertainty about the age-dependency of the root hydraulic parameters has only a small influence on the predawn water potential. However, the age dependency affects the development of the hydraulic conductivity of the total root system and hence also the xylem water potential during transpiration.

Further, the root hydraulic properties used in the model could be validated and/or optimized by additional measurements of water potential in the collar or the leaves. The most reliable measurement of leaf water potential (pressure chamber, Scholander et al. (1965)) is destructive and hence not suitable for measurement of changes over time. Lately developed sensors for leaf turgor (ZIM-probes, Zimmermann et al. (2013)) have the potential to overcome this problem. However, for given root architecture and transpiration rates, the ranking of the collar water potentials that were simulated for our experiments will remain the same if the hydraulic properties of root segments and their dependency on age are assumed to be the same for all plants.

3.6   Conclusion and Outlook

The initial goal was to disentangle root water uptake dynamics in a soil environment with strong water potential gradients. We addressed this question using a novel approach combining experiments, CT scanning and a simulation model. Notwithstanding the uncertainties that arise due to parameterization of the model we demonstrated the synergisms that emerge from combining split root experiments with model simulations and came to the following conclusions:

1)   In horizontal split experiments not only the soil hydraulic redistribution is altered, but whole plant performance.

2)   Using a simulation model in combination with data of the root architecture development, we found that the split layers generated an important resistance to vertical water flow or water redistribution in the soil column. Vertical redistribution of water was an important process to provide the root system with sufficient water for uptake. A restriction of this redistribution led to lower simulated predawn root and collar water potentials which were related to lower measured stomatal conductance. The lower predawn water potentials pointed at plant stress that resulted in a restriction of root and shoot growth.

3)   Vertical redistribution along water potential gradients in the soil makes it generally impossible to link local root water uptake with local changes in soil water content. Also in split root experiments, which are designed to reduce this redistribution, redistribution might nevertheless be important when large differences in soil water potentials between compartments emerge despite low hydraulic conductivities of split layers.

4)   If vertical redistribution of water through the soil is restricted, there may be nevertheless a substantial amount of water that is exchanged between the roots and the soil in the drier regions of the root zone.

5)   Simulation results suggest that predawn collar water potential can only be related to the wettest soil water potential in case of low heterogeneity. In case of soil moisture heterogeneity the predawn water potential is closer to the dry soil part.

6)   Paraffin layers are not perfectly hydraulically isolating different soil compartments.

7)   Conclusions 2-6 could not have been made without soil and root water flow simulations. To setup the model, data on the dynamic root architecture was essential. The agreement between measured and simulated soil water potentials and their dynamics for the different root architectures and experimental conditions (scenarios for the different soil setup) while making

use of the same set of root hydraulic and soil parameters for all the simulated experiments indicates that the flow processes in the coupled soil-plant systems were well represented in the model.

By knowing the distribution of soil and root water potentials, the combined method presented here would allow to study the direct relation between water use and root or plant growth, as was recently shown by Bao et al. (2014). Nevertheless, this is the first study in which 3D simulations of water flow in coupled soil-plant studies were performed based on real data of the root architecture and validated against measurements of soil water potential. We did not focus on how to setup an experiment so that root properties and their uncertainty could be derived from such a setup but we rather consider the study as a proof-of-concept. In future studies, inverse modeling could be carried out to determine the root parameters and their uncertainty.

4 Root-soil contact dynamics in drying soil

Nicolai Koebernick, Sebastian Blaser, Steffen Schlüter, Doris Vetterlein

4.1   Abstract

Root-soil contact is a prerequisite for the uptake of water and nutrients from the soil matrix. Root shrinkage and decrease of root-soil contact in drying soil has been shown repeatedly, but only few studies have investigated the dynamics of root shrinkage and its relationship with plant and soil water status. We studied the development of root-soil contact of *Vicia faba* L. during a drying period. Plants (N=4) were grown in cylinders filled with a sandy soil. Samples were repeatedly scanned with an X-ray CT scanner to visualize root-soil contact. Soil matric potential, transpiration rate, and stomatal conductance were measured daily. Initial root-soil contact was below 60 % in taproots and close to 90 % in lateral roots. Transpiration rate and stomatal conductance decreased before roots started to shrink. Lateral roots had a higher relative shrinkage than taproots, but they retained higher root-soil contact. Three hours after re-watering shrinkage was almost completely reversed and initial root-soil contact was recovered. This study confirms previous findings with *Lupinus albus* roots in that roots shrink after transpiration rate decreases. In contrast to *Lupinus*, lateral roots of *Vicia faba* shrink more than taproots, but they still retain partial contact to soil.

4.2   Introduction

Root-soil contact is of critical value for plant-soil interactions. Complete root-soil contact can cause problems with aeration, while low contact can limit the uptake of water and solutes by constraining the hydraulic pathway (Veen et al., 1992). The degree of root-soil contact is influenced by the texture and the water status of the growing medium (Herkelrath et al., 1977; Kooistra et al., 1992; Tinker, 1976). We define root-soil contact as the proportion of the root surface in contact with the fluid film adhering to soil particles, i.e. the solid phase plus water filled pores. We exclude root hairs from this definition. Typical root hair diameters are between 6-16 μm (Leitner et al., 2010), which is too small to be captured both precisely and representatively using current industrial CT scanners. When we assume that the total interfacial area of water scales linearly with saturation, which is true for a sand with perfect wettability (Kim et al., 1997), the potential degree of root-soil contact is a function of the porosity ϕ and the degree of saturation S_w of the surrounding medium, i.e. rhizosphere soil. If we regard a root simply as a convex structure embedded randomly in a porous medium, average root-soil contact will be

$$\rho = 1 - \phi\,(1 - S_w) \tag{4.1}$$

where ρ is root-soil contact. This relationship holds when we define porosity and saturation explicitly for the soil at the immediate root-soil interface, which may have different properties than bulk soil. As roots advance in the soil, they penetrate and deform the soil matrix and this can lead to appreciable compaction around the roots (Bruand et al., 1996; Vollsnes et al., 2010). Secondary growth of older roots may contribute to soil compaction. Reduced root-soil contact occurs when roots grow into macropores or loose soil where they retain only partial contact or as a consequence of root shrinkage (Tinker, 1976).

Living root tissues shrink when they are dried beyond a certain threshold. Theoretical considerations about the formation of air gaps adjacent to the root surface date back to the 1950s (Bernstein et al., 1959; Philip, 1957). Direct evidence of shrinking roots in soil was provided by Huck et al. (1970), who observed diurnal diameter changes by 25% of a cotton root segment in response to changes in transpirational demand. Cole and Alston (1974) determined that shrinkage occurs at a water potential between -0.5 and -1 MPa in excized maize roots. The first study to analyze root shrinkage with actual measurements of root-soil contact was conducted by North and Nobel (1997a). They determined root-soil contact of droughted *Agave deserti* roots with a thin-section technique (Van Noordwijk et al., 1992). They found

that root-soil contact had decreased from 94% to 21% after 14 days of drought. In a second treatment, they re-established root-soil contact of the droughted roots by vibrating the samples. This resulted in lower soil water potentials around the roots, indicating higher root water uptake and hence a limiting role of root-soil contact in water uptake. The vibrated roots also shrank less, which suggests a possible feedback mechanism between contact loss and root shrinkage. Such a mechanism was proposed by Carminati et al. (2013), who stated that once a gap is formed at the root surface, the additional resistance to water flow will lead to increased root shrinkage and thus shrinkage is a self-enforcing process.

The reliance on destructive methods has hindered researchers to study in detail the temporal dynamics of root shrinkage and gap formation with regard to plant and soil water status. Recent advances in non-invasive imaging techniques allow the direct observation of the root-soil interface during plant growth. Particularly X-ray computed tomography (X-ray CT) is now widely used in the study of plant-soil interactions (Mooney et al., 2012). If scanning parameters are chosen carefully to avoid damage of plant tissues, repeated CT scans of the same samples can be conducted to observe dynamic changes of the properties of interest (Zappala et al., 2013a).

Carminati et al. (2009; 2013) first observed the formation of air gaps with X-ray CT. In their experiments using *Lupinus albus* roots in a sandy soil substrate, air gaps appeared at soil matric potentials between -10 and -20 kPa, after transpiration rate of the plants started to decrease. They concluded that air gaps were not the cause but rather a consequence of water stress. The authors compared the shrinkage of taproots with lateral roots and found that taproots shrank to a higher degree than the laterals. Such a dissimilar behavior raises the question, if the observed differences are merely a result of the larger diameter of taproots or if such functional plasticity is a plant strategy for the efficient utilization of resources, as it was proposed by Carminati and Vetterlein (2013). There is clearly more research needed to answer this question. In Carminati et al. (2013) the detection of air gaps at lateral roots was complicated by resolution and no method for the determination of root-soil contact was available. Therefore the possibility of partial contact was omitted, while it may play an important role in maintaining water and nutrient uptake at low water potentials. Tinker (1976) argued that, due to surface tension forces, it is more likely that shrinking roots lose contact on one side of their surface, while the other side remains in contact with soil. Numerical simulations by Nye (1994) showed that partial contact loss may lead to strong gradients of water potential within the root cortex. Simulated water potential was highest in the part of the cortex that was near the contact zone with soil and steeply decreased away from it. Thus, when a root starts to lose contact at one point of its surface, further shrinkage is more likely to occur near this point and shrinkage will be eccentric.

To analyze the extent of root shrinkage and the occurrence of partial contact, a method for the quantification of root-soil contact is needed. A robust method of root-soil contact determination in X-ray CT images has been developed by Schmidt et al. (2012). After segmenting the images into root soil phase they used a morphological dilation operation on the soil phase so that it overlapped with the root surface. Basic set theory then provided the degree of root-soil contact.

In the present paper, we will present an alternative method of root-soil contact determination using Minkowski functionals. The purpose of this study is to extend previous experiments of Carminati et al. (2013) on the dynamics of root shrinkage with *Lupinus albus* by (i) including a method for root-soil contact quantification, (ii) using a different species, *Vicia faba*, and (iii) imaging at a higher resolution for a better comparison of taproots and laterals. The use of *Vicia faba* was partly motivated by the comparatively large diameter of its roots, which will simplify the detection of gaps at the surface of lateral roots. The use of a different species will also help to generalize previous findings.

4.3   Materials and Methods

Plant material and experimental setup

The experiment was set up with four replications (*Vicia* I, II, III, IV). PVC cylinders (8.1-cm diameter, 20-cm height) were filled with a sandy soil from the field site "Hühnerwasser", which consisted of 92% sand, 5% silt, and 3% clay. The soil was sieved to 2 mm and packed into the cylinders by passing it through two sieves. The procedure resulted in a homogeneous packing and a bulk density of 1.62 ± 0.007 g cm^{-3} (porosity = 38.9 %). Seeds of *Vicia faba* L. cv. "Fuego" were surface sterilized in 10 % H_2O_2 for 10 minutes and soaked for one hour in a saturated $CaSO_4$ solution. Seeds were placed on wet filter paper and stored in a dark cabinet at room temperature for 24 hours to allow for germination. Germinated seeds were carefully transplanted in the soil at 1-cm depth. The soil surface was covered with quartz gravel (2-5 mm) to minimize evaporation. Liquid flower fertilizer (Terrasan GmbH, containing 7% N, 1.3% P, 5% K) was diluted 1:100 and 100 ml per column of the solution was applied to plastic reservoirs, the cylinders were placed in these reservoirs. After all the water was taken up by capillary rise, an additional 50 ml of deionized water was applied. Free water was always available in the reservoirs to provide well watered growth conditions for 14 days (ψ_m = 0 kPa at the bottom of the columns). At the start of the drying period the reservoirs were removed. The drying period lasted 13-23 days varying between different samples. At the end of the experiment plants were rewatered by placing the plastic reservoirs with 100 ml deionized water at the bottom of the samples for three hours. Plants were grown in a climate chamber under controlled conditions (14 h photoperiod, photon flux density 350 mmol m^{-2}s^{-1}, constant temperature 23° C, 65% relative humidity). Throughout the experiment the columns were placed on balances and the weight was continuously recorded. From the balance data, total plant transpiration was calculated. Relative transpiration rate was calculated as the ratio between actual transpiration rate and the maximum transpiration rate at the start of the drying period. Microtensiometers (Vetterlein et al. 1993) were inserted at 5-cm depth and soil matric potential was measured at a 10 minute interval. Stomatal conductance was measured daily using a steady-state leaf porometer (Decagon Devices, Version 6.0) on the abaxial side of the youngest unfolded leaves. A measurement was made on each leaflet and the mean of two measurements was recorded.

CT scanning

CT scans of the samples were performed with an industrial X-ray micro-CT scanner (X-Tek HMX 225) equipped with a finefocus X-ray tube (spot size 5 μm). Initial scans of the entire columns were performed to locate the taproot and laterals. Based on these scans, a region of interest (field of view 3 x 3 cm, resolution 60 μm

voxel side length) was chosen for local tomography. The region of interest was located at a depth of 3-6 cm below the soil surface in the center of the cylinder in all the samples. Local tomography, where the field of view is smaller than the total sample size, can be used to image a subsample of the entire object at a higher resolution. A precondition for local tomography is the macroscopic homogeneity of the region outside the field of view, which is satisfied for homogeneously packed soil columns. A downside of this method is the occurrence of truncation artefacts, most commonly appearing as a bright concentric band at the truncation edges. Local CT scans were recorded with X-ray energy of 130 kV and a current of 500 µA. We recorded 800 projections with an exposure time of 400 ms using 2 frames per projection. The resulting total scan time was 10.6 minutes. X-ray dose per scan was estimated using the free online calculator RadProDose (McGinnis 2002-2006). The estimated dose was 1.1 Gy per scan. With a maximum number of 10 scans per sample, the cumulative dose was still well below the critical dose to influence plant growth (~30 Gy; (Zappala et al., 2013a)). To reduce the number of total scans per sample, we did not scan on a daily basis, but rather observed the development of soil matric potential in the samples and scanned when we expected changes in root-soil contact, based on prior experiments with *Lupinus albus* in the same substrate (Carminati et al., 2013). CT scans were performed in the middle of the day phase of the 14h photoperiod. When the plants were rewatered, additional CT scans were performed three hours after rewatering.

Image processing and analysis

The region of interest scan caused a truncation artefact, appearing as a bright band at the truncation edge and a characteristic gray value shift from the edges towards the center, similar to beam hardening. The artefact was corrected by fitting an empirical function to the gray values of a predefined region, excluding roots:

$$f(x) = a + \frac{b}{(1 - \frac{x}{\max(x)})^c + \varepsilon}$$

(4.2)

where x is distance to the center, *max(x)* is the maximum distance to the center, a is the average gray value in the center of the image, b and c are fitting parameters, and $\varepsilon = 0.0001$. The artefact could not be removed completely (clearly visible in Figure 4.1), therefore the image analysis was restricted to a cylinder of 2.4 cm (400 pixels) diameter in the center of the images. Cone beam artefacts at the top and the bottom of the image were removed by cropping, reducing the height of the images to 2.7 cm (450 pixels). Raw images (Figure 4.1A) were filtered using an adaptive Gaussian filter to remove small scale noise while preserving edges (Figure

78

4.1B). An unsharp mask was performed subsequently to enhance the contrast at the edges of objects (Figure 4.1C).

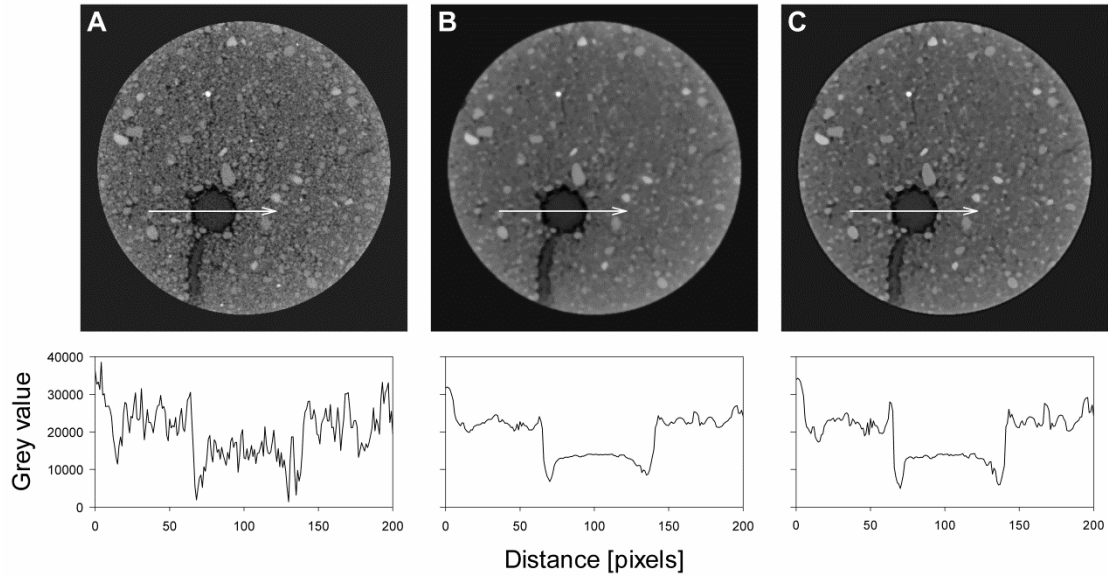*Figure 4.1: Horizontal slice of a local tomography of Vicia I at Day 13 of the drying period, showing the effect of image processing. Below, the profile of gray values along the white arrows in the images containing soil, the taproot, and surrounding air gaps is shown A) raw image B) filtered with adaptive gaussian filter C) sharpened with unsharp mask*

The histograms of the resulting images were bimodal with distinctive peaks for the root phase and the solid soil phase (Figure 4.2). The air phase had no separate peak but was represented by a tail at the lower end of the histogram. Therefore, we used a stepwise procedure to segment the three different phases. In the first step, the root phase including air was segmented from the soil phase. We computed the threshold using the average threshold computed by five standard histogram-based thresholding methods following the procedure described in Schlüter et al. (2014). Disconnected pores were excluded by applying region growing from a seed point within the root system and a subsequent opening operation. In the second step, the histogram of the resulting region, which contained the root system and the air gap, was used to find the threshold between air and roots with Rosin's method for unimodal thresholding (Rosin, 2001).

The segmented images contained artefacts caused by partial volume effects at the transition between air and soil phase (Figure 4.3B). These voxels were erroneously classified as root voxels. We developed a procedure to remove these partial volumes by marking all root voxels with both air and soil voxels in their neighborhood as transition voxels (Figure 4.3C). Transition voxels were reclassified

as either soil or air voxels, based on the comparison of their gray value with the mean gray value of the soil phase and the air phase, respectively (Figure 4.3D).
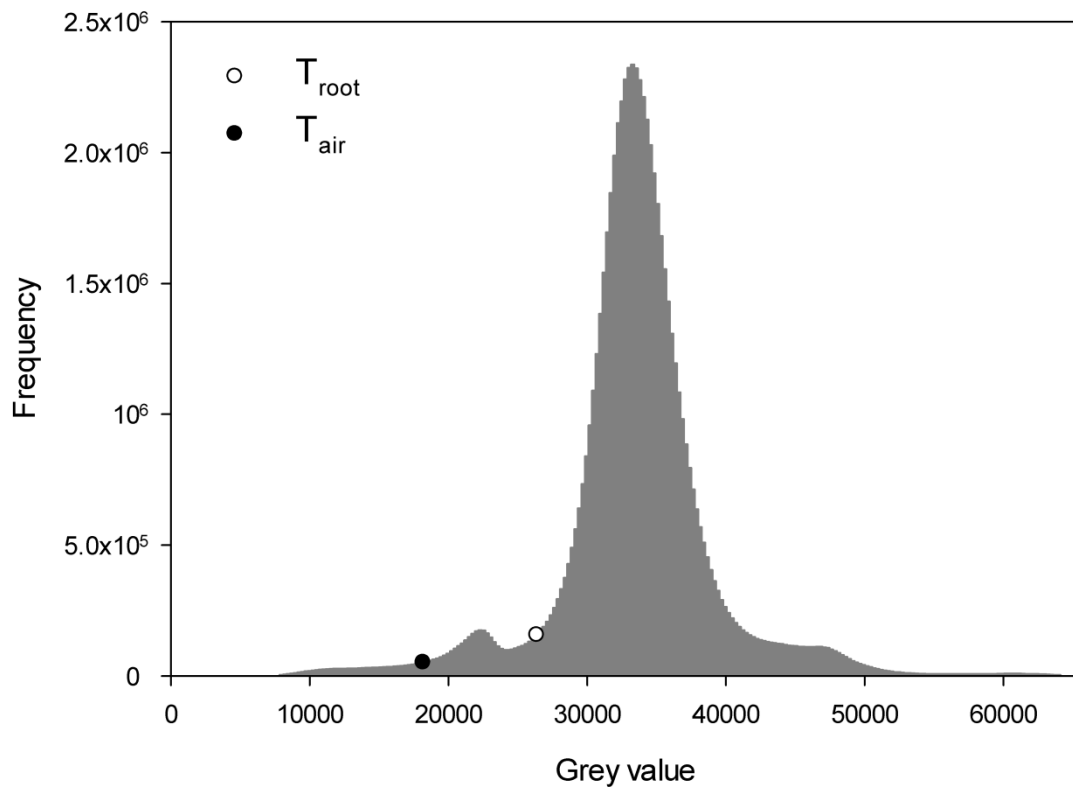

Figure 4.2: Histogram of the gray values of the filtered image of Vicia I on Day 12. The white circle denotes the threshold for the segmentation of roots (T_{root}), the black circle denotes the threshold for air (T_{air})
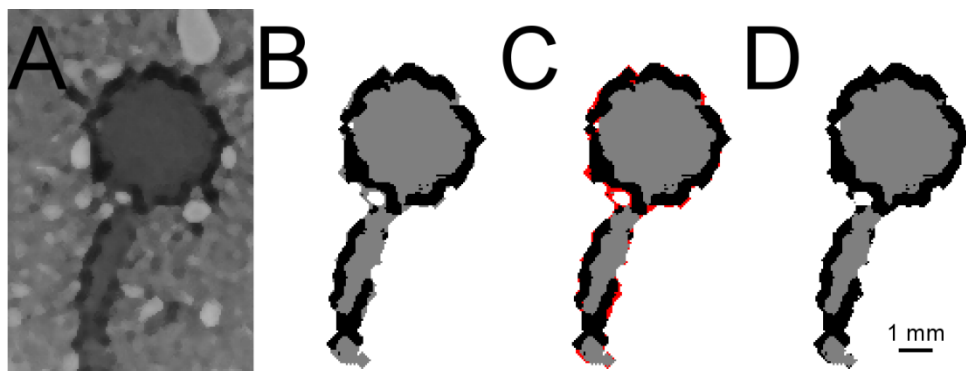

Figure 4.3: Enlarged cutout of the horizontal slice seen in Figure 1, showing the results of segmentation and post-processing. A) Filtered gray scale image B) Classified image after segmentation. Soil phase is white, root phase is gray, and air phase is black. Disconnected air-filled pores are part of the soil phase C) Transition voxels between soil and air phase are marked in red. Note that transition voxels were located based on 3D images D) Classified image after reclassification of transition voxels

Volume and surface area of the different phases were quantified by computing the Minkowski functionals (MFs) of each phase. MFs are basic geometric measures used to quantify structural properties which provide direct physical interpretations. In a three-dimensional Euclidean space, there are four MFs (Vogel et al., 2010). Only the first two will come to use in the present paper. The first functional, M_0, corresponds to the total volume of the structural unit, in our case root, soil matrix, or air. The second functional, M_1, corresponds to the interfacial area between structure and background. MFs are defined for binary structures; therefore the images have to be segmented into structure and background for each phase that is evaluated. The additivity of the MFs enables a straightforward calculation of root-soil contact. The surface area A of the evaluated phase is the sum of the boundary areas with the remaining phases. The linear system

$$A_{root} = A_{root-air} + A_{root-soil}$$
$$A_{soil} = A_{root-soil} + A_{air-soil}$$
$$A_{air} = A_{root-air} + A_{air-soil}$$

is solved for root-soil contact area

$$A_{root-soil} = \frac{A_{root} + A_{soil} - A_{air}}{2}$$

Percentage of root-soil contact is then simply calculated by

$$\rho = \frac{A_{root-soil}}{A_{root}} \times 100$$

(4.3)

For the analysis of root soil contact, taproot and laterals were analyzed separately. They could be easily separated by their different diameters. The opening map of the root phase was calculated and subsequently segmented by using a threshold which excluded lateral roots.

An alternative way of calculating root soil contact is provided by morphology and basic set theory (Schmidt et al., 2012): Dilation of the root phase yields all the voxels at the root interface. A subsequent intersection with the soil phase yields only soil voxels in contact with the root. The ratio of both volumes is calculated to estimate root-soil contact. This is possible, because the ratios of the volume and the respective area of a defined shape are the same.

Image analysis was performed using the freely available software ImageJ and QuantIm (www.quantim.ufz.de).

4.4   Results

Effect of soil drying on plant transpiration

The duration of the drying period varied between the four replications. In *Vicia* I, which was the largest plant, the soil dried faster than in the remaining samples (Figure 4.4), the sample was rewatered after 13 days. *Vicia* II was rewatered after 17 days of drying. The remaining samples *Vicia* III and IV had lower transpiration and were rewatered on Day 23. Soil matric potential after rewatering could not be measured because air bubbles had formed in the tensiometers.
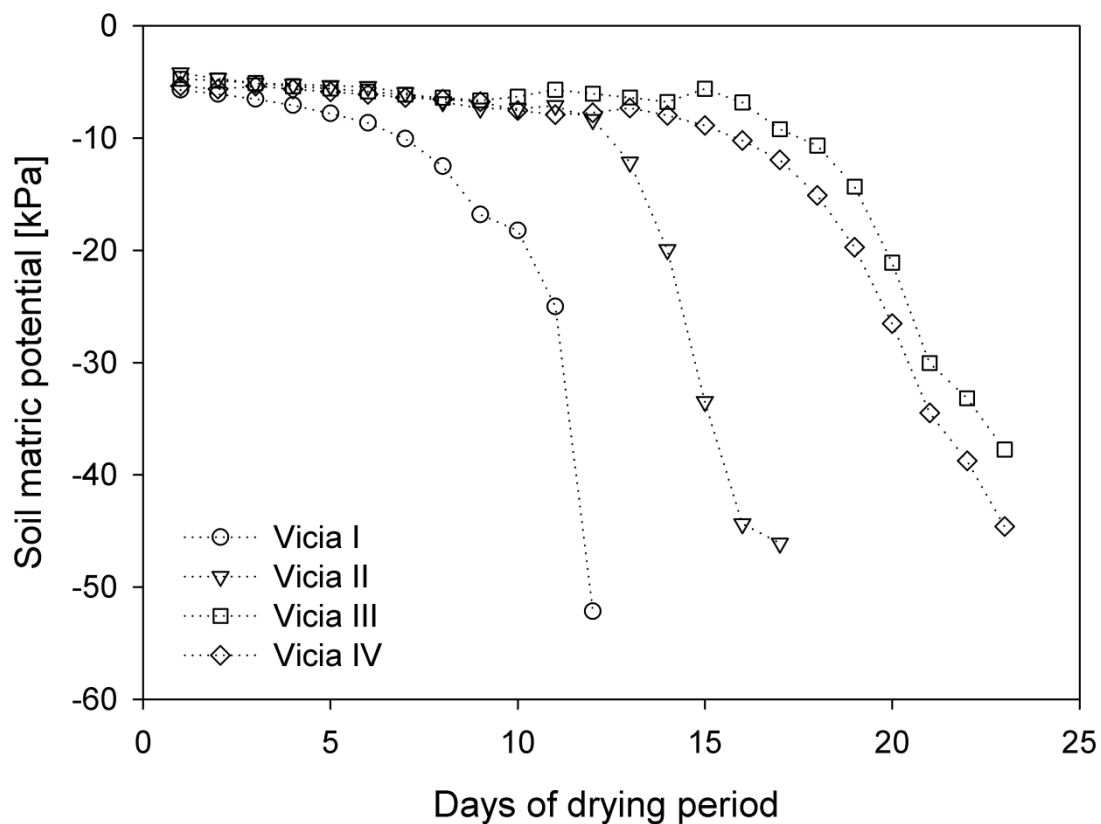
Figure 4.4: Development of soil matric potential over time during the drying period. Values are the mean soil matric potential of one day

Stomatal conductance of the youngest unfolded leaves decreased rapidly after the start of the drying period (Figure 4.5A). At soil matric potentials below -5 kPa stomatal conductance was already strongly reduced. Further drying of the soil only slightly affected stomatal conductance. 24 hours after rewatering we measured the recovery of stomatal conductance. Moderate recovery was seen in *Vicia* I (100.3 mmol m^{-2}s^{-1}) and *Vicia* II (66.7 mmol m^{-2}s^{-1}), while in *Vicia* III and IV there was no recovery after 24 hours (1.2 and 4.4 mmol m^{-2}s^{-1}, respectively). Reduction of stomatal conductance was accompanied by a reduction of relative transpiration rate

(Figure 4.5B). Maximum transpiration rate was observed on Day 4 of the drying period in *Vicia* III and on Day 2 for the remaining samples. Between -5 to -10 kPa, transpiration decreased to about half of the maximum, below -10 kPa relative transpiration still decreased, but the reduction was less steep. Minimal relative transpiration showed high variability between different samples, ranging from 1 % in *Vicia* IV to 31 % in *Vicia* III.
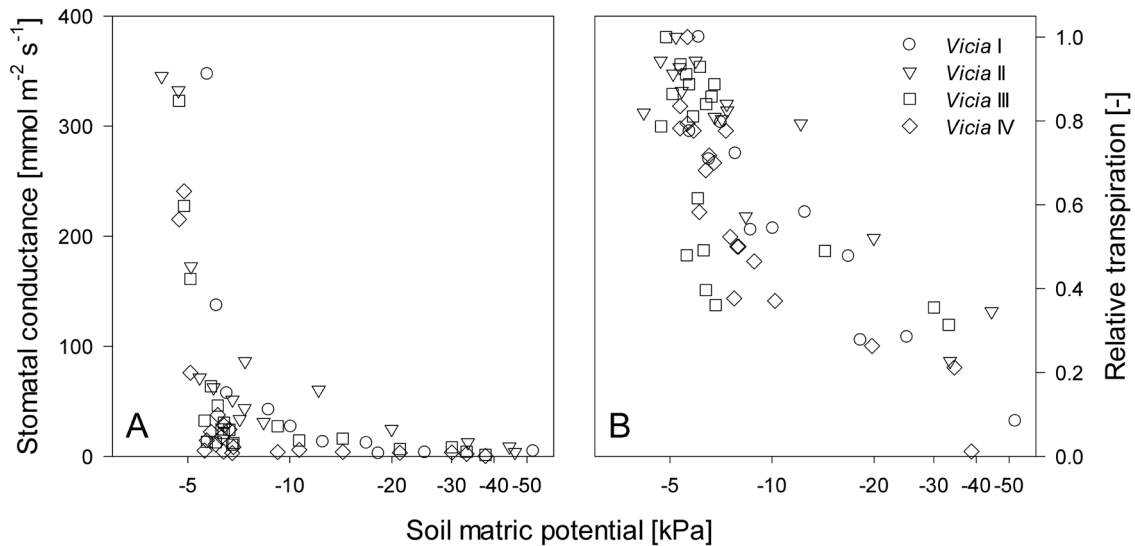

Figure 4.5: Development of A) stomatal conductance and B) relative transpiration rate over soil matric potential. Note the logarithmic scaling of soil matric potential

Development of root-soil contact

The different phases, soil, root, and air could be distinguished according to their gray values. In Figure 4.3A coarse sand particles appear bright, the soil matrix appears light gray, roots are dark gray, and air filled spaces appear black. The temporal development of the three phases from the start of the drying period (left column), to the end of the drying period (center) up to 3 hours after re-watering (right column) is depicted in Figure 4.6. All volumes of interest contained taproots and laterals. Samples I-III had similar architectures, while sample IV differed in that (i) there were overall fewer roots in the analyzed volume, and (ii) only the upper 9-mm of the taproot could be clearly distinguished. Further down, the root divided into three roots of similar diameter (Figure 4.6J-L). These were classified as lateral roots. There were no marked differences in root architecture over time within the analyzed volume of interest. This is confirmed by the quantitative analysis. Combined volume of roots and air within the analyzed region of interest changed only slightly over the course of the experiment (Figure 4.7), indicating that (i) the segmentation procedure was robust; (ii) the volume of the soil phase did not change significantly during soil drying; and (iii) there was no significant root growth within

the scanned region. In some instances, a part of the root system was not successfully segmented at a specific time step, which partly explains slight changes of the combined volumes (Figure 4.6B). The single volumes of the root and the air phase changed markedly over the drying period. A decrease of root volume was accompanied by an increase of air volume, signifying the shrinkage of roots.
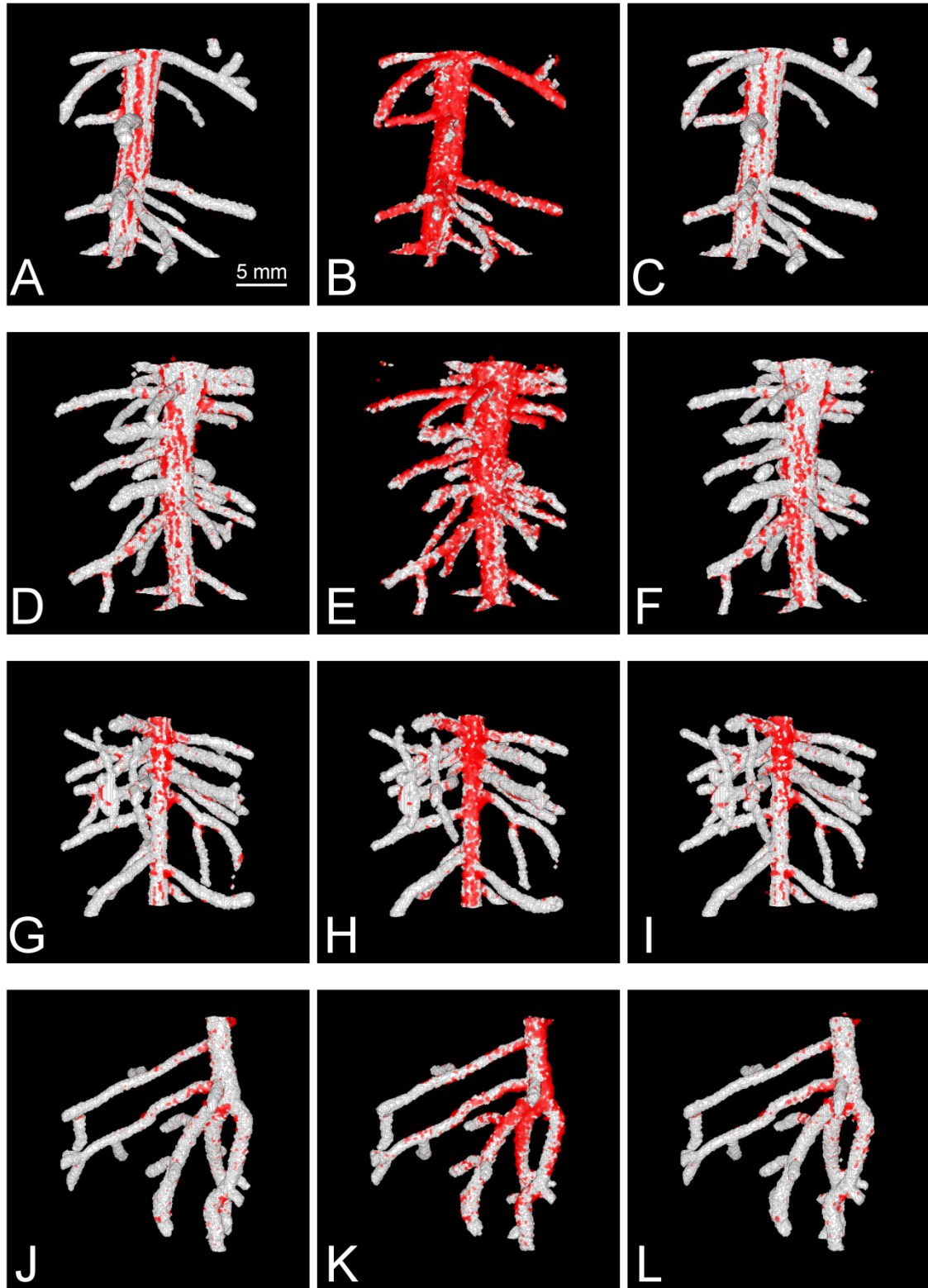
Figure 4.6 (previous page): 3D rendered view of the root systems (gray) and air gaps adjacent to the root (red) within the region of interest at the first scan (left column), before rewatering (middle column), and 3 h after rewatering (right column) A-C) Vicia I (D-F) Vicia II (G-I) Vicia III (J-L) Vicia IV. Dimensions of the shown region are 2.7 cm x 2.4 cm x 2.4 cm. The detached root fragment seen at the top in a and c was not detected in B
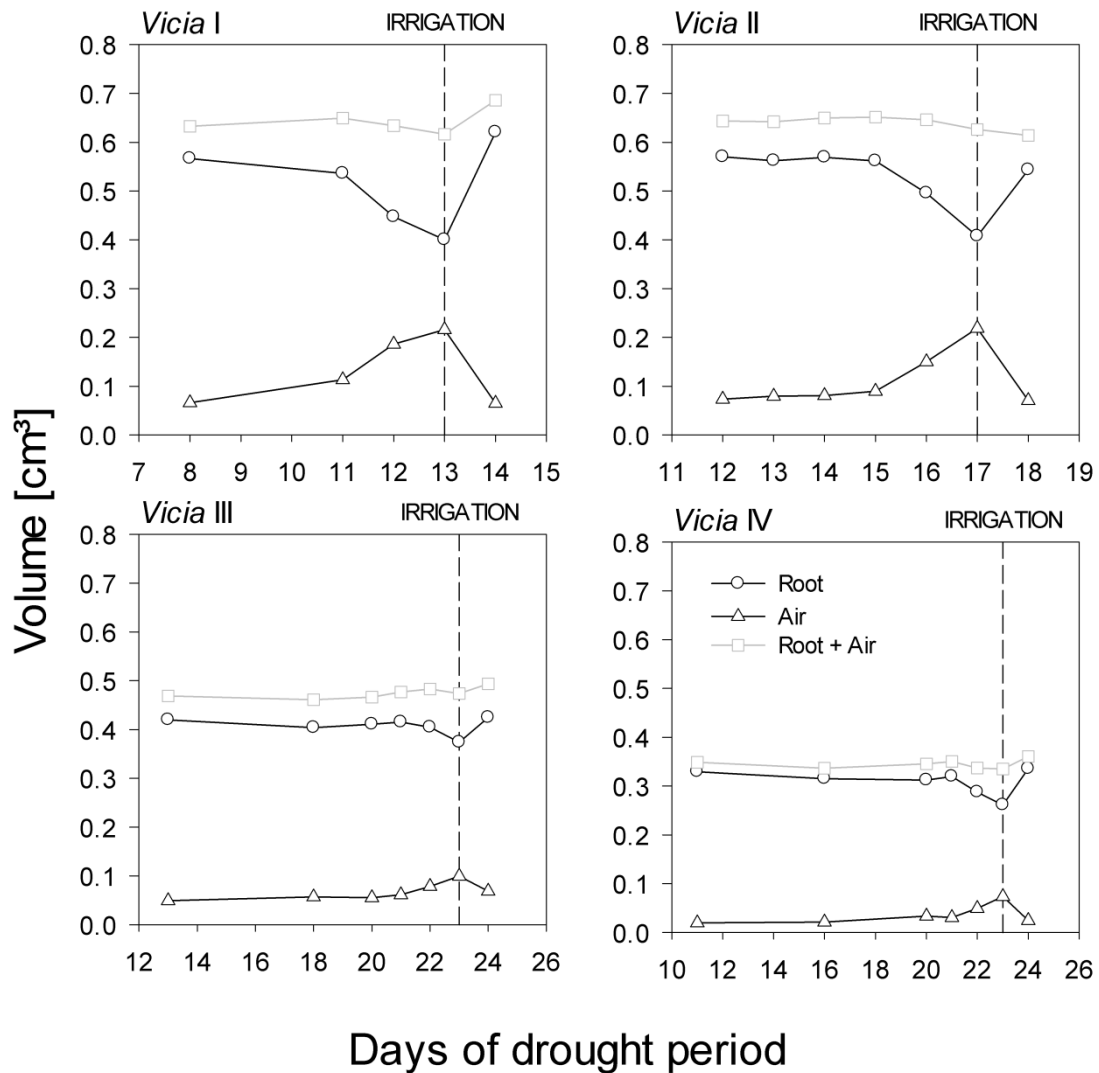

Figure 4.7: Development of volume of the root and air phase within the region of interest over time, respectively. Black circles represent air volume, gray circles represent root volume. Open triangles represent the combined volume of both phases. Note the different ranges of the time axis

There was a considerable variation between the different samples in both the extent and the dynamics of shrinkage. *Vicia* I and II showed a much stronger shrinkage than the remaining samples III and IV. At the end of the drying period, root volume of both *Vicia* I and *Vicia* II was reduced to 71 % of the respective original volume at the first scan. Root volume of *Vicia* IV at the end of the drying

period was 79 % of the original volume. Roots of *Vicia* III shrank to a lesser extent; the final volume was 89 % of the original volume. Three hours after re-watering, root volume increased in all samples, while air volume decreased simultaneously. Temporal dynamics of root shrinkage showed a high variation between different samples. Initiation of root shrinkage was apparent on Day 11 of the drying cycle in *Vicia* I, on Day 16 in *Vicia* II, while in *Vicia* III and IV it started only on Day 23. Only in *Vicia* I, shrinkage was observed between the first two scans. In the remaining samples both air and root volume changed only slightly until Day 16 (*Vicia* I) and Day 22 (*Vicia* III and IV), when root shrinkage was initiated. The shape of the volume changes over time showed an increasing rate of shrinkage with the duration of the drying period (Figure 4.7).
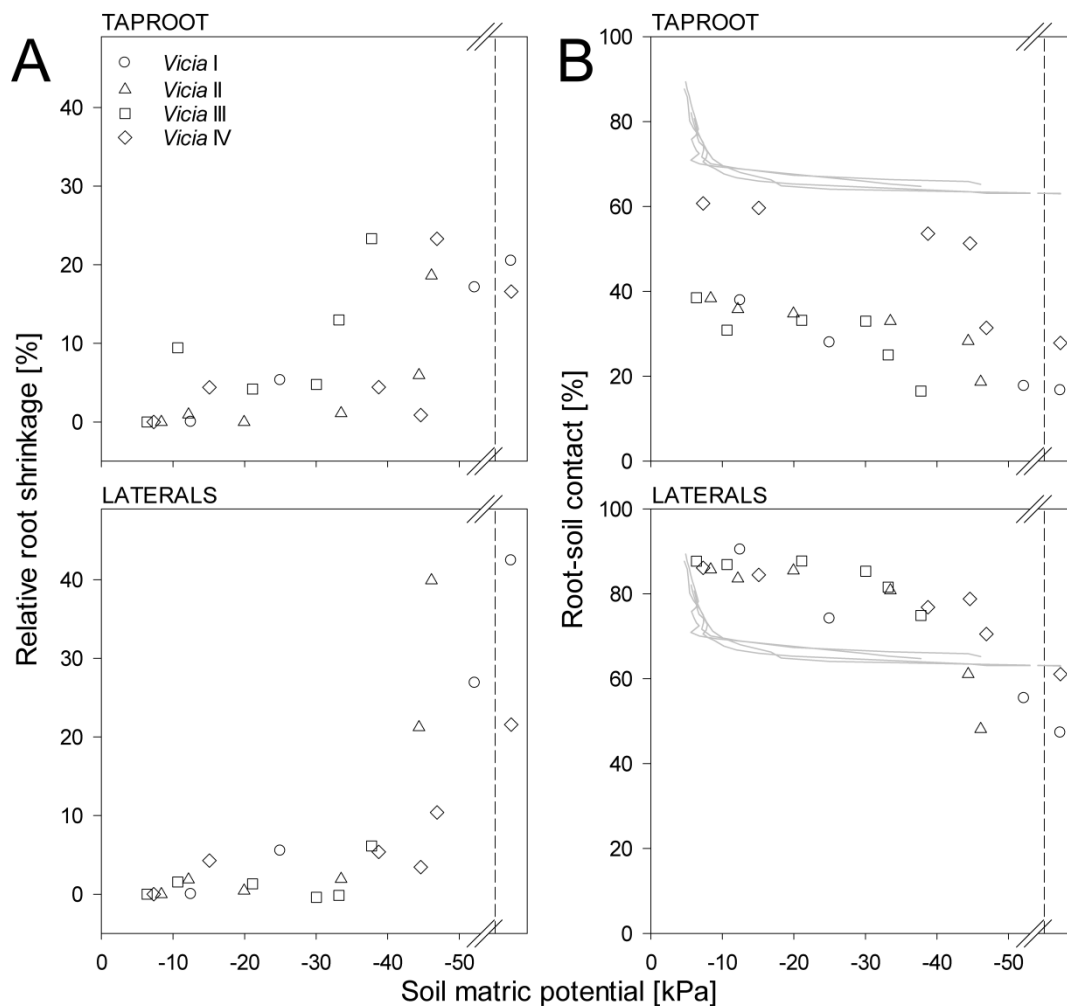

Figure 4.8: A) Development of relative root shrinkage over matric potential B) Development of root-soil contact over matric potential. Gray lines denote root-soil contact calculated with Eq. 4.1. The dashed lines at the right hand side of each plot indicate that no values for matric potential were available for the final scans. The last recorded value was in both cases -55 kPa

For further analysis taproot and laterals were analyzed separately. Relative root shrinkage was calculated in relation to the root volume at the first scan time. When plotted over matric potential, the dependence of root shrinkage on soil water status becomes more apparent (Figure 4.8A). Both the taproot and lateral roots showed only a slight variation of root volume (< 10 %) at matric potentials higher than -30 kPa. At lower matric potentials, a clear trend of root shrinkage was observed in all the samples. Except for *Vicia* III, where laterals showed only little change in volume, the relative volume loss of lateral roots at the end of the drying period was higher compared to the taproot. This was most pronounced in *Vicia* I and II, where the drying period was shorter. In *Vicia* IV shrinkage of taproots and laterals was similar. Three hours after irrigation root shrinkage was almost completely reversed, volumes differed only slightly from initial values. Assuming constant root length and a cylindrical shape of roots, relative shrinkage can be depicted in terms of diameter. Relative shrinkage in diameter (S_d) is related to relative volumetric shrinkage by

$$S_d = 1 - \frac{d}{\max(d)} = 1 - \sqrt{\frac{V}{\max(V)}}$$

(4.4)

where d is the diameter and V the volume of the root, respectively. Relative change in diameter at the end of the drying period is shown in the first column of Table 4.1. The average initial diameter of taproots as estimated from the ratio of volume and surface area was 1.8 mm, average diameter of laterals was 1.1 mm.

Table 4.1: Relative root shrinkage depicted as diameter change and change of root-soil contact during the drying period

Sample	Relative shrinkage (diameter) [%]		Root-soil contact at first scan [%]		Root-soil contact before re-watering [%]		Root-soil contact after re-watering [%]	
	taproot	laterals	taproot	laterals	taproot	laterals	taproot	laterals
Vicia I	10.8	24.1	37.9	90.4	16.7	47.3	41.2	86.2
Vicia II	9.8	22.5	38.4	85.8	18.7	48.1	35.4	86.6
Vicia III	12.4	3.1	38.5	87.7	16.5	74.9	33.9	83.2
Vicia IV	8.7	11.5	60.7	86.1	27.9	61.1	51.9	85.3

A major difference between taproot and laterals was observed when analyzing root-soil contact. While lateral roots had initially close to 90 % contact to the soil phase, root-soil contact of the taproot was initially between 40-60 % (Figure 4.8B). The occurrence of air gaps at the taproot was mostly confined to the

locations of lateral root emergence. At the points, where laterals emerged, complete rings of air around the base of the lateral root could be observed (Figure 4.9A). Consequently, *Vicia* IV showed the highest root-soil contact of the taproot, as only few laterals emerged in the analyzed region. Root-soil contact of the taproot decreased almost linearly with soil matric potential, at the end of the drying period contact with the soil phase was between 16.5 – 27.9 %. In lateral roots, root-soil contact decreased only slightly at matric potentials above -30 kPa. Below -30 kPa root-soil contact decreased sharply to values between 47.3 – 74.9 % at the end of the drying period. Thus, lateral roots showed more intense shrinkage and higher relative loss of root-soil contact than taproots but retained higher root-soil contact over the entire drying period. Three hours after re-watering root-soil contact showed similar values to the first scans after starting the drying period (Table 4.1).

A further difference between taproot and lateral roots was the location of the air gap. When the gap was at maximum extension, it formed an almost complete, concentric ring around the taproot. For lateral roots complete contact loss was only seen at the base, while in more distal parts the air gap was eccentrically located on one side of the root, while the opposite side remained in contact with the soil. However, in some instances we observed that there were soil particles stuck at the root surface and air filled gaps were forming few micrometers away from the immediate soil-root interface (Figure 4.9B).
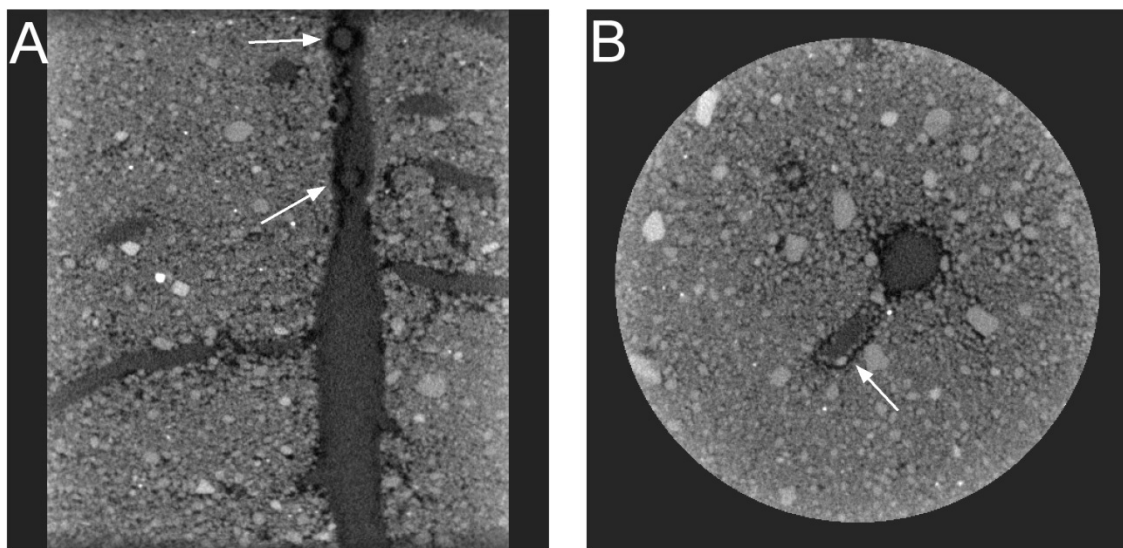

Figure 4.9: A) Vertical slice of Vicia I, after 8 days of the drying period. White arrows show air rings at the base of lateral roots B) Horizontal slice of Vicia II, after 17 days of the drying period. The white arrow points to a "divorced gap" appearing behind particles adhering to the root surface. The thickness of the layer adhering to the roots is ca. 5 pixels (300μm). Total size of both images is 30 x 30 mm

The effect of the choice of the threshold on our results was tested by varying the original T_{air} by segmenting and reanalyzing the images with a manually changed T_{air}. We chose a 5 % higher and a 5 % lower T_{air}, thus creating an envelope of 10% around the computed threshold. The difference of root-soil contact due to the variation of T_{air} by 10 % was on average 11.5 ± 4.7 %.

To validate the Minkowski method for root-soil contact quantification, we determined root-soil contact with an alternative method based on the dilation of the root phase and subsequent intersection with the soil phase (hereafter referred to as dilation method). For the comparison, root-soil contact in all the images was determined with both methods for the combined root phase (taproot and laterals). The two methods were highly correlated (Figure 4.10).
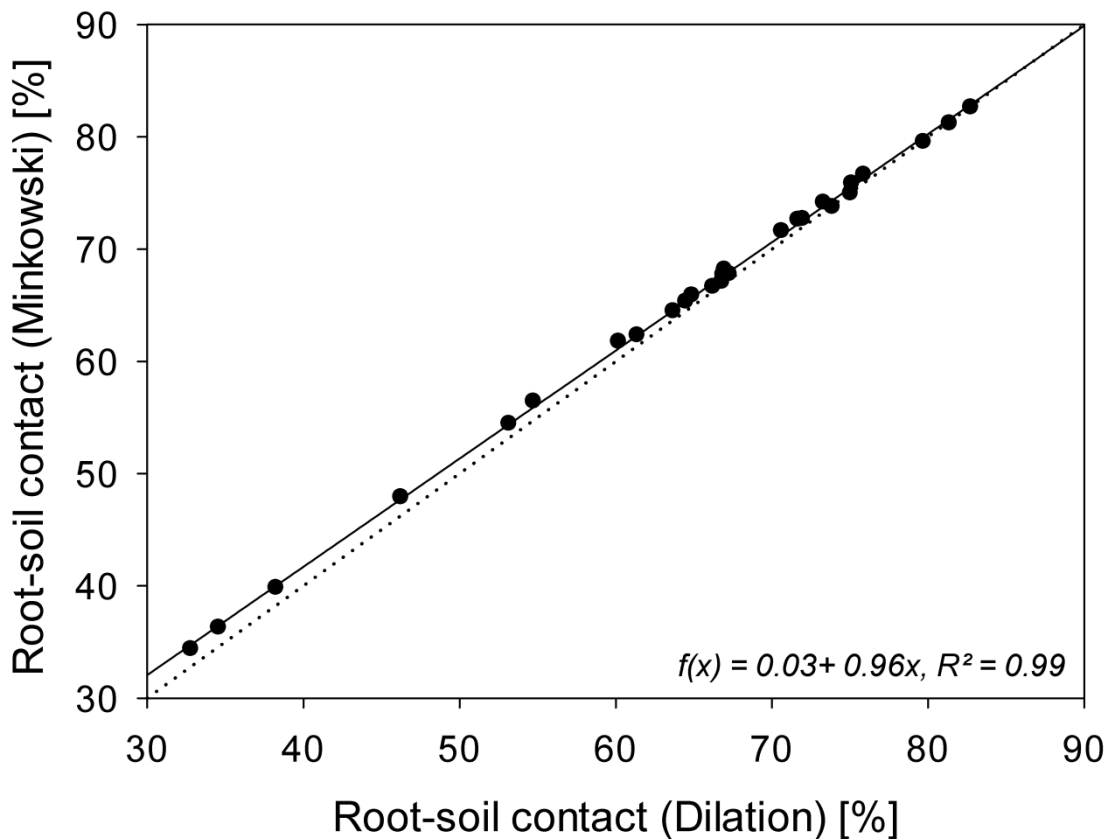

Figure 4.10: Comparison of the two different methods to quantify root-soil contact. The straight line represents the linear regression. The dotted line represents the 1:1 relationship

4.5   Discussion

Determination of root-soil contact

The Minkowski method to determine root-soil contact showed good agreement with the dilation method. The latter is similar to the procedure used by Schmidt et al. (2012), who determined that the accuracy of their method in measuring the contact area of defined phantoms was 3 %. We note that the Minkowski method is much faster because it can be directly applied to the segmented images. The accuracy of any method is obviously affected by image quality, most notably resolution, signal to noise ratio and contrast. The threshold to segment roots from air is a particularly sensitive parameter, as our sensitivity analysis for T_{air} has shown. Assuming an accuracy of 10 % in finding the "true" threshold, we determined an error of 11.5 % in root-soil contact. This highlights the need for an automated threshold detection to avoid user bias. The effect of changing T_{root} was not tested, as it is a less sensitive parameter than T_{air}. The contrast between roots and soil matrix is much higher than the contrast between roots and air. Changing T_{root} would lead to a change of the total volume of roots within the region of interest. It would therefore affect relative shrinkage, but it would not affect root-soil contact. Initial root-soil contact of the lateral roots was on average 87.5 ± 1.8 %. Calculation of root-soil contact with Equation 4.1, using a porosity of 38 % (derived from bulk density) and the average initial water content of 26 % (estimated from sample weight), results in a very similar root-soil contact of 88 % (Figure 4.8). At the initial matric potential of -5 kPa, the mean diameter of drained pores calculated with the Young-Laplace equation will be approximately 60 μm, which is exactly the resolution of the scans. In other words, all visible pores in the vicinity of lateral roots will be drained whereas all pores below the resolution limit will still be water filled at this matric potential. Hence the good agreement between estimated and image-derived root-soil contact indicates that macroporosity around laterals is very similar to bulk soil. Root-soil contact of taproots was significantly lower (40-60%) than expected from Eq. 4.1. Thus taproots have altered their immediate vicinity towards higher macroporosity than in the bulk soil.

For all data points in Figure 4.8 during drying, i.e. when soil matric potential decreases beneath -5 kPa, we observe very different dynamics of estimated and image-derived root-soil contact. This is because both metrics are sensitive to completely different processes. The estimated root-soil contact captures the reduction of water saturation in the rigid soil matrix which cannot be detected by imaging due to limited resolution. In turn, the reduction of image-derived root-soil contact is truly a function of root shrinkage, for which again only gaps bigger than the image resolution can be detected. From this we conclude that Eq. 4.1 should only be used to estimate root-soil contact in a saturation range in which all

unresolved porosity is fully saturated. In this case it is an excellent means to test how representative bulk soil properties are for soil around roots.

Relation between root shrinkage and transpiration

Root shrinkage was observed long after stomatal conductance decreased, showing that air gaps were not the cause of water stress. The early decrease of stomatal conductance and relative transpiration at relatively high soil matric potentials is explained by the coarse texture of the soil substrate and the resulting drop in soil hydraulic conductivity. This is in agreement with previous work on *Lupinus* using the same substrate (Carminati et al., 2013). We measured stomatal conductance on the youngest unfolded leaves, which explains the steeper reduction of stomatal conductance compared to relative transpiration rate. As the responsiveness of stomata to water stress tends to decrease with leaf age (Blackman and Davies, 1984; Willmer et al., 1988) we hypothesized that stomata in older leaves retained higher aperture at moderate stress levels and closed when stress was more severe. This was confirmed by single measurements on older leaves (data not shown). When roots started to shrink at matric potentials below -30 kPa no further decrease of stomatal conductance of the young leaves could be observed, yet, relative transpiration rate was still decreasing. It can therefore not be excluded that the additional resistance to water flow caused by reduced root-soil contact contributed to water stress at this point. We can again only state that gap formation was clearly not the initial cause of stress, confirming the conceptual model postulated in Carminati et al. (2013).

Dynamics of root shrinkage

The different dynamics of root shrinkage in the replications are explained by the duration of the drying cycle. In samples I and II, which were overall bigger, transpiration rate was higher than in the remaining samples. Sample I had a maximum transpiration rate of 28.5 g water per day and plant, sample II 19.5 g d^{-1}, and samples III and IV transpired 17 g d^{-1} on maximum. Sample I and II also had the highest degree of root shrinkage, which can be explained by a higher (residual) transpirational demand. The link between root shrinkage and soil matric potential is only an indirect one: Shrinkage of cortex cells is triggered by root water potential, which is strongly affected by transpiration rate. Huck et al. (1970) put it more simple: "Shrinkage occurs when roots lose water faster than they absorb it". This also means that shrinkage will increase with vapor pressure deficit and net radiation for a given soil hydraulic conductivity. It is also expected that the extent of root shrinkage will change diurnally, as was observed by Huck et al. (1970). Additionally, plants could show differences in osmotic adjustment, i.e. plants experiencing slow development of drought stress have more time to adapt osmotically.

Gaps around roots closed within three hours after irrigation, while stomatal conductance had not recovered completely on the next day. Samples I and II showed some recovery, while samples III and IV kept their stomata closed. This hints to the accumulation of abscisic acid (ABA) in the leaves (Hsiao, 1973), as the latter endured the drought period for a longer time, and the fact that roots had swollen seems to discount plant water potential as a reason for stomatal closure. Yet, no measurements of plant water potential or ABA concentrations in the leaves are available to confirm this.

The comparison of our present results for *Vicia faba* with those of Carminati et al. (2013) for *Lupinus albus* shows that roots of both *Lupinus* and *Vicia* started to shrink at a similar soil matric potential between -10 to -30 kPa. In the present study the dynamics of gap formation can be seen more accurately due to technical improvements. Our results show that the shrinkage rate increased with the duration of the drying cycle and with decreasing soil matric potential. We stopped the drying period somewhat arbitrarily when gaps were clearly visible, because we wanted to observe the behavior upon re-watering. Further drying would likely have resulted in a typical s-shaped pressure-volume curve as in Cole and Alston (1974). It is apparent that the soil matric potentials measured here and in Carminati et al. (2013) are much higher than the root water potentials at which Cole and Alston observed root shrinkage (between -0.5 and -1 MPa), but also much higher than the soil water potentials at which Huck et al. (1970) observed diameter changes in cotton (between -0.1 and -0.7 MPa). Even more negative soil water potentials were reported by North and Nobel (1997a; 1997b) for desert succulents, but these values were measured when gaps were already present for a long time. Again, we explain this by the coarse texture of our soil substrate. The soil matric potentials were measured in bulk soil, no measurements of either root water potential or matric potential at the soil-root interface were available. While potential gradients at the soil-root interface are difficult to measure, simulation studies show that they have a high impact on the occurrence of water stress (Schröder et al., 2009) and that they are more important in coarse textured soils (Javaux et al., 2008). When roots start to shrink and the hydraulic pathway is reduced by decreasing root-soil contact, the gradient at the root-soil interface will become even larger. Even when roots retain partial contact, flux density will increase at a given volumetric flow rate leading to a larger water potential drop (Faiz and Weatherley, 1982; Tinker, 1976).

We conclude that the dynamics of root shrinkage are governed by soil water availability and transpirational demand. Major factors determining the dynamics of shrinkage include biotic factors like plant size and physiological adaptation to drought, as well as abiotic factors like soil type and weather conditions.

Taproots versus laterals

The most striking difference between *Vicia* and experiments with *Lupinus* in Carminati et al. (2013) was the different behavior of taproots and laterals. While in *Lupinus* the taproot shrank more than laterals, roots of *Vicia* showed the opposite behavior with much higher shrinkage of lateral roots. A major difference between both species is the thickness of lateral roots. While *Vicia* laterals in the present study had a diameter of over 1000 μm, *Lupinus* lateral roots were generally below 500 μm in diameter. If we calculate gap size for these diameters, relative shrinkage of 10% would result in a gap of 50-100 μm (depending on the eccentricity) in *Vicia* and 25-50 μm in *Lupinus*. Consequently, gaps around *Vicia* roots are easier to detect. Carminati et al. admitted that their spatial resolution (100μm) was limiting the detection of gaps around laterals. They suggested the use of a higher resolution to confirm these results, which we have done in the present study. As they have rightly pointed out, bigger gaps will be drained at higher matric potentials, meaning that thicker roots lose hydraulic contact earlier. We cannot exclude the possibility that there are other anatomical or physiological differences between the roots of both species, which further explain the observed differences.

Different resolution can certainly not explain the observed difference of taproot shrinkage. Taproots in the present study had only partial contact with the soil even under well-watered conditions. It would seem likely that the potential drop at their interface would therefore be larger and shrinkage would be more pronounced, as was suggested by Carminati et al. (2013). A possible explanation why taproots shrank less is a higher radial resistance to water flow due to the suberization of the taproot endodermis. This would isolate the xylem and reduce water depletion from the cortex. Typically, radial resistance of older roots tends to increase with the development of apoplastic barriers (Bramley et al., 2009; Frensch and Steudle, 1989). As a consequence, root-soil contact of the older taproot is less critical. This is in agreement with the notion that the main function of taproots or primary roots is long distance transport, while laterals are the main sites of water and nutrient uptake (McCully, 1999). An alternative explanation is that taproots of *Vicia* underwent more secondary growth than *Lupinus*, resulting in a larger share of the rigid stele versus cortex area.

Root-soil contact of the taproot – the role of lateral emergence

Initial restriction of root-soil contact of taproots had not been reported by Carminati et al. (2013), as the authors did not quantify root-soil contact, but width of the air gap and diameter of the roots, respectively. In the present study, low contact of the taproot coincided with the emergence of laterals. In many instances there was an obvious ring of air around the laterals, exactly where they emerged from the taproot (Figure 4.9A). As laterals emerge they have to rupture the cortex.

This is beautifully illustrated in Pond's drawing of a seedling (Pond, 1908), where the ruptures closely resemble the rings of air we observed. As laterals advance further they push away soil particles in their way, thereby increasing the size of these localized air gaps. A further cause of lower root-soil contact at the taproot could be the lower abundance of root hairs and mucilage, which are both thought to be critical for the establishment of good root-soil contact.

Lateral roots shrink more – but retain partial contact

Finally, we show that lateral roots retained partial contact with the soil, although they exhibited higher relative shrinkage than taproots. We cannot state with certainty, that partial contact with the soil would have been maintained during further drying. However, referring to our introduction, it is more likely that an additional contraction of the roots will lead to more shrinkage on the side where the surface is no longer in contact with the soil. Partial contact might even be crucial to maintain water and nutrient uptake under drought conditions, as elegant experiments have shown that re-establishment of root-soil contact by "squeezing" or vibrating the soil temporarily reduced water stress in *Helianthus annuus* (Faiz and Weatherley, 1982). While the squeezing treatment might have resulted in a change of the water retention curve, which could partly explain these results, other work has shown that water and nitrate uptake decreases with decreasing root-soil contact (Veen et al., 1992). In roots growing into pre-existing macropores, partial contact may even determine patterning of lateral roots. Bao et al. (, 2014) showed that lateral root production of roots with partial contact at one side was biased towards the contact side. This bias was not caused by contact per se but by the higher water availability at the contact side.

The occurrence of gaps further away from the root-soil interface, while soil particles adhered to the root surface, has also been reported by North and Nobel (North and Nobel, 1997a). Greenland (1979), who had suggested the possibility of such "divorced" gaps, attributed them to the presence of mucilage around roots. He stated that these gaps might be just as significant in limiting mass flow to roots as gaps at the immediate root surface. Even if gaps form immediately at the root surface there remains the possibility that root hairs bridge the gaps and they may be of exceeding importance for water uptake under these conditions (Tinker, 1976).

4.6   Conclusions

We have presented an efficient method of measuring the dynamics of root shrinkage and root-soil contact in a drying soil using X-ray CT scans of *Vicia faba* roots grown in a sandy soil substrate. The study confirms previous work with *Lupinus albus* in that root shrinkage and the formation of air gaps at the root-soil interface occurs when transpiration rate is already severely reduced. Both *Vicia* and *Lupinus* showed a similar reaction to water stress and root shrinkage was initiated at similar soil matric potentials. We therefore confirm that root shrinkage is a consequence and not the cause of water stress. When gaps appear, they will contribute to water stress by narrowing the hydraulic pathways and increasing the water potential drop at the root-soil interface.

A major difference between both species was the extent of shrinkage in the different root orders. While in *Lupinus* lateral roots shrank less than taproots, the present study shows that in *Vicia* the contrary was true. Whether the differences are merely a result from different image resolution or there are true anatomical and physiological differences remains uncertain. Clearly, more comparative studies are needed to answer this question, preferably involving more species from different plant families. We have shown that although they exhibit higher shrinkage, lateral roots retain partial contact with the soil, thus further enabling the uptake of nutrients and water. Retention of partial contact may be related to the abundance of root hairs and mucilage, but further studies involving plants differing in those traits are needed to confirm this.

As root shrinkage is closely related to root water potential, diurnal variation of root-soil contact is expected. Future studies should therefore include pre-dawn measurements to see if gaps close completely at night with the relaxation of plant water potential (and if the opposite is true in CAM plants, where stomates open at night).

The effect of gap formation on root water uptake has yet to be quantified. We propose the use of image based modeling, similar to the approach of Aravena et al. (2011; 2014) to study the effect of soil compaction around roots. Such studies could also determine the potential of root hairs to bridge the gap, as root hairs can now be visualized in-situ using synchrotron imaging (Keyes et al., 2013).

5   Final discussion and conclusions

Imaging and quantification of RSA with X-ray CT

The major obstacle for the analysis of the role of RSA in root water uptake is the difficulty to measure root traits in-situ. In *Chapter 2,* a methodological approach to quantify the distribution and growth of roots in soil was presented. Any quantification of root traits requires the isolation (or segmentation) of roots from the soil. In the present work a region-growing algorithm was used, which is now a standard approach for the segmentation of roots from CT scans (Flavel et al., 2012; Kaestner et al., 2006). The method was relatively time consuming and required user based decisions. To avoid user bias and to enable higher throughput, more automated methods are being developed. For example, Mairhofer et al. (2012) developed a tracking approach based on the level set method, which was later extended to enable the recovery of plagiotropic roots (Mairhofer et al., 2013). It remains unclear, whether the approach is applicable to all situations. In both semi-automated and automated approaches, successful segmentation of roots depends largely on image quality, most notably the contrast between roots and background, signal-to-noise ratio, and spatial resolution. Especially the contrast between roots and background is additionally affected by soil properties like soil water content (Flavel et al., 2012; Zappala et al., 2013b) or soil organic matter content. The method developed in this study was applicable to roots grown in a homogeneously packed sandy substrate. To be applicable to a range of different soil types, including heterogeneous soils with high soil organic matter contents and macropores, the method will likely need to be improved. Additionally, there is always a trade-off between sample size and image resolution, as well as between scan duration and signal-to-noise ratio. The X-ray parameters will have to be tailored to fit the specific research question, and the same is still true for the digital image processing.

Once the root system is successfully segmented, root architectural traits can be quantified. Since RSA is highly complex and cannot be easily described by a single metric, the question arises which are the relevant root architectural traits to quantify. In studies dealing with root water or nutrient uptake, the root system is typically characterized by the root length density over discrete soil depth increments. A method to quantify the root length was developed that is based on the calculation of the integral of mean curvature of an object's boundary. The integral of mean curvature corresponds to the third Minkowski functional (MF) of a binary structure in three dimensional Euclidean space. We have shown that the third MF of a cylindrical object is a measure for cylinder length. The same concept was previously used by Schladitz (2012) to measure the strut length of open foams. Assuming a cylindrical geometry of roots, we applied this approach to root systems. The method

was tested using virtual root systems which were created with the root growth module from the model R-SWMS. Comparison with the classical approach of measuring the length of the skeleton showed that the major difference between both approaches is the different sensitivity to root junctions. The mean curvature approach is additionally affected by the number of root tips and likely the degree of surface roughness. These sensitivities should be tested in future work by measuring the length of defined virtual objects differing in these properties. Still, the mean curvature approach is a promising alternative to skeletonization, as it has a similar accuracy but is computationally much more efficient. Higher spatial resolution will also allow the use of MFs to measure the volume and the surface area of the root system without additional computational costs (Vogel et al., 2010). This was exploited in *Chapter 4* to quantify the shrinkage of roots and the degree of root-soil contact. A major drawback of the MF based approach is that is does not permit the analysis of root system topology, which is possible when analyzing the skeleton. Another important aspect of RSA, the temporal dynamics, can be studied when using time-lapse CT data. Time-lapse data sets were used in all the studies in this work. Besides enabling the analysis of root growth in different depths or soil compartments, they allow the description of root demography, i.e. the classification of the root system based on root segment age. Many physiological properties of roots such as root respiration, P-uptake, and hydraulic conductivity depend on root age (Bouma et al., 2001; Bramley et al., 2009; Doussan et al., 1998b). In *Chapter 4*, root age was used to define age dependent hydraulic conductivities in the simulation of root water uptake. Root age also plays an important role in the formation of the rhizosphere, which shows age dependent differences in hydraulic properties and the composition of the microbial community (Carminati, 2013; Marschner et al., 2002). The potential of time-lapse CT scanning to analyze the dynamics of root growth was not fully exploited in this work. In *Chapter 3*, it was shown that the addition of paraffin layers suppressed root growth as well as shoot growth by generating drought stress. To verify this, drought experiments with well-watered control treatments would be needed. Time-lapse CT scanning would then enable to observe the response of the root system to the onset of drought. In principle, this is possible for any environmental cue, which underlines the potential for time-lapse CT in analyzing the ability of roots to respond to changing environmental conditions. This is also true for root-soil interactions, as was demonstrated in *Chapter 4* for the development of root-soil contact.

Given the enormous potential of X-ray CT to measure RSA and root-soil interactions, it is important to note major limitations of the technique. In the framework of this study the most apparent limitation of X-ray CT is the poor ability to image soil water content. Technically, it is possible to distinguish water and air phases by their different attenuation coefficients but to accurately measure soil

water content much higher resolutions than used in this work are required (Tracy et al. 2015). Preferred techniques for imaging soil water content are magnetic resonance imaging and neutron imaging (Downie et al., 2014). Metzner et al. (2015) stated, that the main advantage of X-ray CT for imaging root systems is the high achievable resolution, while at lower resolutions magnetic resonance imaging is more accurate due to higher contrast. The same should be true for neutron imaging, which is however limited to small sample sizes (Moradi et al, 2011).

Sample size is a general limitation for most non-invasive imaging techniques including X-ray CT. In the present work, relatively large sample sizes were used at the cost of a reduced resolution. While resolution is improving with technological development, X-ray CT will be limited to laboratory scale experiments for the foreseeable future. This has to be considered when extending conclusions to the field scale. Even at very small sample sizes, current industrial CT scanners are limited to a resolution of ca. 10 μm, which limits their application in respect to the detection of small-scale features such as root hairs or even internal root structure (Downie et al. 2014). Synchrotron imaging has been used recently to image root hairs in soil (Keyes et al., 2013) but the low accessibility of synchrotron beam lines limits its widespread use.

Since X-ray CT quantifies material (electron) density it is not suited to image the chemical or microbial composition in the soil. Combination of X-ray CT with other imaging techniques across different scales is needed to relate different spatial metrics and will be a major challenge for future work.

Root water uptake – experimental approach and simulations

In *Chapter 3*, a combined approach of experiments and simulation modeling for the analysis of the relationship between RSA and water uptake was presented. The goal was to quantify the distribution of root water uptake relative to RSA and how this relationship is affected by soil moisture availability and heterogeneity. The experimental approach to localize root water uptake was based on local measurements of soil matric potential in different soil depths. Two different experiments were conducted, where the main difference was the presence or absence of horizontal wax layers in the soil. The layers were placed in the soil to eliminate vertical redistribution of soil moisture and to allow the formation of strong soil moisture gradients. Virtual experiments, conducted with the model R-SWMS, were set up to reproduce the experimental conditions: the geometry of the domain, initial and boundary conditions, root system architecture and soil hydraulic properties were derived from experimental data. The observed responses to drought stress (stomatal closure, decrease of transpiration rate, growth reduction) were explained by simulating the plant water potential.

This was the first study, which implemented in-situ measurements of dynamic RSA into a three-dimensional root water uptake model. The implementation of the dynamic root architecture was based on previous work by Stingaciu et al. (2013) who used a reconstructed root system from a single MRI scan. Comparison between measurements and simulations shows that water flow in roots and soil was well represented, notwithstanding the uncertainties related to root hydraulic properties. The work highlighted the need to account for the redistribution of soil water when attempting to localize root water uptake. In the unrestricted soil without physical barriers to water flow it was impossible to measure local root water uptake. The soil matric potential in different soil depths remained essentially in hydrostatic equilibrium due to soil hydraulic redistribution. The placement of horizontal wax barriers in the soil failed to completely eliminate the vertical redistribution of soil water. Therefore, even in the presence of wax layers, it was impossible to derive local root water uptake from local matric potential measurements. Simulations showed that the discrepancy between local root water uptake and local change in soil water content was high even in the presence of wax layers with a low hydraulic conductivity. These results show that root water uptake cannot be localized using local changes of soil matric potential or water content. In the experiments, local water content in the different compartments was derived from point measurements of soil matric potential. It may be argued that spatially explicit imaging of soil water content would enable the measurement of local root water uptake. But this is clearly not the case, as the discrepancy was also seen in the simulation results, where water content is spatially resolved. Direct measurements of water flow are needed, since the measurement of water content is unable to disentangle the different flow paths (i.e. root water uptake and soil water flow). Neutron imaging of deuterated water flow into plant roots currently shows the greatest potential to quantify local root water uptake (Zarebanadkouki et al., 2012; Zarebanadkouki et al., 2013). The use of wax layers to eliminate vertical soil water redistribution can only be recommended after rigorous testing of their isolating properties.

The wax layers did however introduce an important resistance to the vertical redistribution of water and therefore enabled the development of persisting vertical gradients in soil matric potential. It was shown that the heterogeneity of soil water availability had a high impact on the development of plant water potential. Pre-dawn water potential at the root collar was more closely related to the dry regions of soil and the effective soil water potential was constantly more negative when restricted soil water movement led to heterogeneous soil drying. These simulation results were used to explain the earlier reduction of stomatal conductivity and growth in plants grown in a split-root setup compared to plants grown in a continuous soil. A causal relationship between plant water potential and stomatal conductance was assumed.

Indeed, by linking stomatal function to hydraulic and chemical signaling, a simulation study by Huber et al. (2014) showed that transpiration regulation under heterogeneous soil moisture distribution can be primarily explained by plant water potential. The authors used the same model as in the present work, exemplifying potential future applications for the combination of 3D imaging and simulation modeling. The simulation of plant responses to changing environmental conditions was clearly beyond the scope of the present work. Plant regulation of stomatal conductance and growth was implicitly included because measured transpiration rates were used as boundary conditions and CT scanned root architectures described the root hydraulic architecture.

A general problem of detailed root-soil models like R-SWMS is that they need a high number of parameters, which are sometimes difficult to measure and have to be assessed using literature values. This was most apparent for the parameterization of root hydraulic conductivities. The values were taken from Doussan et al. (Doussan et al., 2006), who had experimentally determined root conductivities for lupin plants. Their measured radial conductivity was uniform across the root system, while other studies have shown substantial variation of radial conductivity along roots (Bramley et al., 2009; Knipfer and Fricke, 2011). Figure 4.8 A shows that a different parameterization using a variable radial conductivity that decreases with age resulted in a significantly altered uptake pattern. Additionally, root hydraulic conductivity shows substantial short-term variations that are linked to aquaporin expression (Javot and Maurel, 2002; McElrone et al., 2007). Such variations enable plants to regulate hydraulic properties dynamically and to respond to changing water availability. Regulation of hydraulic properties can strongly modify water uptake dynamics and should be considered in future modeling approaches (Lobet et al., 2014). There is clearly a need for more data on root hydraulic properties, especially for mature roots grown in soil. Most measurements to date have used young root segments grown in hydroponic culture.

Soil hydraulic properties may be just as important in limiting root water uptake as root hydraulic properties (Draye et al., 2010). This was exemplified by the strong effect of paraffin layers on the development of plant water potential. While paraffin layers are an extreme example, they show the potential effect of soil heterogeneity on the hydrodynamics of the soil-plant continuum. The layers present discontinuities in the flow path, which may occur in natural soils due to heterogeneity, crack formation or biological activity. Root activity can alter the hydraulic properties of the rhizosphere significantly by compacting the soil around roots (Aravena et al., 2014), by the release of mucilage (Carminati et al., 2010; Read et al., 2003), or the formation of air gaps at the root-soil interface (Carminati et al., 2013). In the present study these alterations were not considered, while they may have important consequences for water flow into roots.

Root-soil contact dynamics

In *Chapter 4*, the development of root-soil contact during a drying period was studied in relation to plant and soil water status. Based on a previous study, which showed that roots shrink after transpiration rate decreases (Carminati et al., 2013), the study aimed to extend these results by using a different species and by refining the imaging approach to enable the measurement of root-soil contact. In the previous study, the focus was on the width of the resulting root-soil air gaps and no method for the quantification of root-soil contact was available. The present work showed that *Vicia faba* has similar dynamics as *Lupinus albus*. Shrinkage of roots occurred when stomatal conductance and transpiration rate was severely reduced, showing that the reduction of root-soil contact was not the initial cause of water stress. It was also shown that initial root-soil contact was not complete but it was closely related to air-filled porosity in the lateral roots and significantly lower in taproots. Contrary to the earlier study, lateral roots exhibited stronger shrinkage than taproots but they retained partial contact to the soil.

The fact that the taproot already showed severely reduced root-soil contact before root shrinkage seems to underline its negligible importance in root water uptake from the soil. Measurements were made at the basal part of the root system, where the main function of the taproot is the hydraulic connection to the shoot (McCully, 1999). Lateral roots instead retained partial contact to the soil matrix until the end of the drying period, which has not been shown in earlier work. It remains unclear if more severe drought would have led to a complete detachment of the laterals or to an increased eccentricity of the shrunken root. If roots lose contact completely or retain partial contact probably depends on the surface forces between root periphery and soil, which may change with the abundance of root hairs and mucilage. Retention of root-soil contact has important consequences for continued water and nutrient uptake under drought conditions. However, when roots keep contact at one side of their periphery the flux density will have to be increased locally to take up the same amount of water. This will lead to steeper potential gradients at the root-soil interface. Partial contact may even facilitate the efflux of water from the roots to the soil, known as hydraulic lift (Caldwell et al., 1998). It is still unclear, whether the gaps close at night, when transpiration stops. Diurnal variation of root shrinkage is certainly to be expected (Huck et al., 1970) and should be investigated in relation to the development of plant water potential. Knowledge of the link between plant water potential and root shrinkage will facilitate the implementation of this process into models of root water uptake. A recent simulation study that implemented gap dynamics in a root uptake model showed that gap formation has a significant effect on the development of plant water potential and actual transpiration (Couvreur et al., 2014). Gap dynamics were implemented in a simplified way as a linear decrease of radial root conductivity with

local soil water potential. The authors stated that a better quantitative understanding of the process is needed to represent these dynamics more realistically. Further, it should be investigated if root hairs are really able to bridge any gap, as was suggested by Tinker (1976). In-situ imaging of root hairs, as is now possible with synchrotron imaging (Keyes et al., 2013) may help to answer this question.

6   Summary

The potential of X-ray CT to investigate the dynamics of root system architecture (RSA) and the hydrodynamics in the soil-root system was explored. The impact of RSA on the spatio-temporal dynamics of root water uptake is still poorly understood. The complex hydrodynamics in the soil-plant-atmosphere continuum are increasingly analyzed using mechanistic models that couple water flow in roots and soil. These models use the explicit three-dimensional RSA to define root hydraulic properties as a tree-like system of hydraulic resistances. There is however a substantial lack of actual three-dimensional root system data to compare simulations with experimental observations. Root systems are highly complex and the difficulty to measure RSA in-situ has ignited an increasing interest in non-invasive techniques, particularly X-ray CT, to image root systems in soil. These techniques can also be used to image processes at the root-soil interface that alter hydraulic properties of the rhizosphere. These local alterations can significantly impact root water uptake, but are not fully understood until now.

The main objectives of this thesis were

i)   the development of methods to image and quantify RSA with X-ray CT

ii)   the investigation of the relationship of RSA and root water uptake dynamics

iii)   the investigation of the development of root-soil contact in drying soil

i) A novel set of methods to visualize roots in-situ and to quantify the RSA including its temporal dynamics was developed. It was applied to a temporal sequence of CT scans of a *Vicia faba* L. root system growing in a sandy soil substrate. Quantification of the RSA entailed two essential steps, the isolation or segmentation of roots from the background, and the quantification of the architecture of the isolated root system. In the first step, CT images were filtered and a region growing algorithm was used to distinguish roots from the soil substrate. In the second step, RSA was quantified by measuring the root length distribution over soil depth. To this end, a novel method to measure root length based on Minkowski functionals was developed and tested using virtual root systems of known length. The frequency distribution of Euclidean distances to the nearest root surface was used as a measure of soil exploration by roots. The temporal sequence of CT images enabled the quantification of the temporal dynamics of RSA. It also enabled the quantification of root age, which is inherently

linked to the physiological properties of roots. It was shown that X-ray CT and digital image analysis provide an excellent tool for the quantification of RSA dynamics and can be applied during running experiments with plants.

ii) An approach combining experiments, CT scanning, and numerical simulation was used to analyze the dynamics of root water uptake. Two pot experiments in continuous soil and in soil that was partitioned using horizontal paraffin layers were conducted. The coupled soil-root model R-SWMS was used to analyze water flow in numerical simulations, which were parameterized with experimental data. Dynamically growing RSA derived from temporal sequences of CT scans could be successfully implemented into the model. Numerical simulations were able to reproduce the observed dynamics of soil matric potential in different soil depths. Simulated plant water potentials indicated that plants grown in soil with paraffin layers were subjected to water stress earlier than in continuous soil. This matched the experimental observations, which showed an earlier reduction of stomatal conductance, plant transpiration, and growth in the plants grown with paraffin layers. It was shown that soil moisture heterogeneity has a high impact on the development of plant water potential. The study showed that local change of soil water content cannot be equated with root water uptake due to substantial soil hydraulic redistribution. Root hydraulic properties and their dependence on root age were identified as a major uncertainty with a strong impact on the pattern of root water extraction. Perturbation of root hydraulic properties did however not affect the qualitative results of the study.

iii) The development of root-soil contact during a drying cycle was investigated with X-ray CT. An efficient method for the quantification of root shrinkage and root-soil contact was developed. Measurements of soil and plant water status showed that root shrinkage is a result rather than a cause of drought stress. Once shrinkage is initiated it contributes to water stress and leads to an increased rate of root shrinkage. Taproots had reduced root-soil contact even under well-watered conditions, while lateral root-soil contact was related to air-filled macroporosity: Lateral roots showed more shrinkage than the taproots but they retained partial contact to the soil until the end of the drying period. Re-watering completely reversed root shrinkage and initial root-soil contact was recovered. The different behavior of taproots and laterals suggests that for taproots, root-soil contact is less critical than for lateral roots.

7   Zusammenfassung

Das Potential der Verwendung von Röntgen-Computertomographie (CT) zur Analyse der Dynamik der Wurzelarchitektur (WA) und der Hydrodynamik im System Boden-Wurzel wurde untersucht. Der Einfluss der WA auf die räumlich-zeitliche Dynamik der Wurzelwasseraufnahme ist bisher nicht ausreichend verstanden. Die komplexe Hydrodynamik im Boden-Pflanze-Atmosphäre Kontinuum wird vermehrt mit Hilfe von mechanistischen Modellen analysiert, die den Wasserfluss in Wurzeln und Boden gekoppelt beschreiben. Diese Modelle nutzen die genaue drei-dimensionale WA zur Darstellung der hydraulischen Eigenschaften in einem baumartigen Schaltkreis hydraulischer Widerstände. Es gibt jedoch einen erheblichen Mangel an tatsächlichen drei-dimensionalen Messdaten des Wurzelsystems, die zum Vergleich von Simulationen mit experimentellen Beobachtungen herangezogen werden können. Wurzelsysteme sind hochkomplex, und die Schwierigkeit der Messung der WA in-situ hat ein gesteigertes Interesse an nicht-destruktiven Verfahren zur Visualisierung des Wurzelsystems im Boden, insbesondere mittels CT, entfacht. Diese Verfahren können ebenfalls genutzt werden, um Prozesse an der Wurzel-Boden-Grenzfläche, die mit Modifikationen der hydraulischen Eigenschaften der Rhizosphäre einhergehen, zu untersuchen. Diese lokalen Modifikationen haben erheblichen Einfluss auf die Wurzelwasseraufnahme, sind aber bis heute nur unzureichend verstanden.

Die Haupziele dieser Arbeit waren

i)   die Entwicklung von Methoden zur Visualisierung und Quantifizierung der WA mit CT

ii)   die Untersuchung der Beziehung zwischen WA und der Dynamik der Wurzelwasseraufnahme

iii)   die Untersuchung der Entwicklung des Wurzel-Boden-Kontakts bei abnehmendem Bodenwassergehalt

i) Ein neuartiges Set von Methoden zur in-situ Visualisierung von Wurzeln und zur Quantifizierung der WA einschließlich ihrer zeitlichen Dynamik wurde entwickelt. Diese Methoden wurden auf eine Zeitreihe von CT Aufnahmen eines *Vicia faba* L. Wurzelsystems angewandt, das in einem sandigen Bodensubstrat wuchs. Die Quantifizierung der WA beinhaltete zwei essentielle Schritte: die Isolierung oder Segmentierung der Wurzeln vom Hintergrund und die Quantifizierung der Architektur des isolierten Wurzelsystems. Im ersten Schritt wurden die CT Aufnahmen gefiltert und ein 'Region Growing' Algorithmus zur Unterscheidung

von Wurzeln und Boden genutzt. Im zweiten Schritt wurde die WA durch die Messung der Wurzellängen-Verteilung über die Tiefe bestimmt. Zu diesem Zweck wurde eine neuartige Methode der Längenbestimmung mit Hilfe von Minkowski Funktionalen entwickelt. Die Methode wurde an virtuellen Wurzelsystemen bekannter Länge getestet. Die Häufigkeitsverteilung von euklidischen Distanzen zur nächstgelegenen Wurzeloberfläche wurde als Maß der Erschließung des Bodens durch die Wurzeln verwendet. Die zeitliche Sequenz der CT Aufnahmen ermöglichte die Quantifizierung der zeitlichen Dynamik der WA. Sie ermöglichte zudem die Bestimmung des Wurzelalters, welches eng mit den physiologischen Eigenschaften von Wurzeln zusammenhängt. Es konnte gezeigt werden, dass CT und die digitale Bildanalyse ein exzellentes Instrumentarium für die Quantifizierung der Dynamik der WA darstellen, dessen Anwendung während laufender Experimente mit Pflanzen möglich ist.

ii) Die Dynamik der Wurzelwasseraufnahme wurde durch die Kombination von Experimenten, CT Bildgebung und numerischer Simulationen analysiert. Es wurden zwei Gefäßexperimente durchgeführt, in einem kontinuierlichen Boden und in einem Boden, der mit horizontalen Paraffinschichten unterteilt worden war. Das gekoppelte Boden-Wurzel Modell R-SWMS wurde verwendet, um den Wasserfluss in numerischen Simulationen zu analysieren, welche mit experimentellen Daten parametrisiert wurden. Eine dynamisch wachsende WA, die aus der zeitlichen Abfolge der CT Aufnahmen erstellt wurde, konnte erfolgreich in das Modell implementiert werden. Die numerischen Simulationen konnten die beobachtete Dynamik des Bodenmatrixpotentials über die Tiefe erfolgreich reproduzieren. Simulierte Pflanzen-Wasserpotentiale deuteten darauf hin, dass die Pflanzen, die im Boden mit Paraffinschichten wuchsen, früher Trockenstress ausgesetzt waren, als die Pflanzen im kontinuierlichen Boden. Dies entsprach den experimentellen Beobachtungen, die eine frühere Abnahme der stomatären Leitfähigkeit, der Transpirationsrate und des Wachstums bei Pflanzen mit Paraffinschichten zeigten. Es konnte gezeigt werden, dass die Heterogenität der Bodenfeuchte einen erheblichen Einfluss auf die Entwicklung des Pflanzenwasserpotentials hat. Die Arbeit machte deutlich, dass eine lokale Veränderung des Bodenwassergehalts nicht mit Wurzelwasseraufnahme gleichgesetzt werden kann, da es erhebliche hydraulische Umverteilung innerhalb des Bodens gibt. Die hydraulischen Eigenschaften der Wurzeln und ihre Altersabhängigkeit wurden als wesentliche Fehlerquelle mit großem Einfluss auf die Verteilung der Wasseraufnahme identifiziert. Eine Sensitivitätsanalyse zeigte jedoch, dass die qualitativen Ergebnisse der Studie davon nicht beeinträchtigt wurden.

iii) Die Entwicklung des Wurzel-Boden-Kontakts während eines Trockenzyklus wurde mit Hilfe von CT Aufnahmen untersucht. Eine effiziente Methode zur Bestimmung der Kontraktion (Schrumpfung) von Wurzeln und des Wurzel-Boden-Kontakts wurde entwickelt. Messungen des Wasserstatus des Bodens und der Pflanzen zeigten, dass die Kontraktion der Wurzeln eine Folge, und nicht die Ursache von Trockenstress ist. Wenn die Kontraktion beginnt, trägt sie zum Trockenstress bei und verstärkt die Rate der Kontraktion. Die Pfahlwurzeln hatten bereits unter ausreichender Bewässerung einen verminderten Wurzel-Boden-Kontakt, während der Wurzel-Boden-Kontakt der Seitenwurzeln mit der luftgefüllten Porosität korrelierte. Die Seitenwurzeln zeigten eine stärkere Kontraktion als die Pfahlwurzeln, allerdings konnten sie bis zum Ende der Trockenperiode partiellen Kontakt zum Boden aufrechterhalten. Erneute Bewässerung machte die Wurzelkontraktion komplett rückgängig und der initiale Wurzel-Boden-Kontakt wurde wiederhergestellt. Das unterschiedliche Verhalten von Pfahl- und Seitenwurzeln weist darauf hin, dass der Wurzel-Boden-Kontakt für Pfahlwurzeln weniger kritisch ist als für Seitenwurzeln.

8   References

Ameglio T, Archer P, Cohen M, Valancogne C, Daudet FA, Dayau S and Cruiziat P (1999), Significance and limits in the use of predawn leaf water potential for tree irrigation. *Plant and Soil* **207**: 155-167.

Aravena JE, Berli M, Ghezzehei T and Tyler SW (2011), Effects of Root-Induced Compaction on Rhizosphere Hydraulic Properties - X-ray Microtomography Imaging and Numerical Simulations. *Environmental Science & Technology* **45**: 425-431.

Aravena JE, Berli M, Ruiz S, Suarez F, Ghezzehei T and Tyler SW (2014), Quantifying coupled deformation and water flow in the rhizosphere using X-ray microtomography and numerical simulations. *Plant and Soil* **376**: 95-110.

Arganda-Carreras I, Fernandez-Gonzalez R, Munoz-Barrutia A and Ortiz-De-Solorzano C (2010), 3D Reconstruction of Histological Sections: Application to Mammary Gland Tissue. *Microscopy Research and Technique* **73**: 1019-1029.

Bao Y, Aggarwal P, Robbins NE, Sturrock CJ, Thompson MC, Tan HQ, Tham C, Duan L, Rodriguez PL, Vernoux T, Mooney SJ, Bennett MJ and Dinneny JR (2014), Plant roots use a patterning mechanism to position lateral root branches toward available water. *Proceedings of the National Academy of Sciences* **111**: 9319-9324.

Bernstein L, Gardner WR and Richards LA (1959), Is There A Vapor Gap Around Plant Roots. *Science* **129**: 1750-&.

Blackman PG and Davies WJ (1984), Age-related Changes in Stomatal Response to Cytokinins and Abscisic Acid. *Annals of Botany* **54**: 121-126.

Bouma TJ, Yanai RD, Elkin AD, Hartmond U, Flores-Alva DE and Eissenstat DM (2001), Estimating age-dependent costs and benefits of roots with contrasting life span: comparing apples and oranges. *New Phytologist* **150**: 685-695.

Böhm J (1893), Capillarität und Saftsteigen. *Ber. Dtsch. Bot. Ges.* **11**: 203–212.

Bramley H, Turner NC, Turner DW and Tyerman SD (2009), Roles of Morphology, Anatomy, and Aquaporins in Determining Contrasting Hydraulic Behavior of Roots. *Plant Physiology* **150**: 348-364.

Bruand A, Cousin I, Nicoullaud B, Duval O and Begon JC (1996), Backscattered electron scanning images of soil porosity for analyzing soil compaction around roots. *Soil Science Society of America Journal* **60**: 895-901.

Caldwell MM, Dawson TE and Richards JH (1998), Hydraulic lift: consequences of water efflux from the roots of plants. *Oecologia* **113**: 151-161.

Carminati A, Moradi AB, Vetterlein D, Vontobel P, Lehmann E, Weller U, Vogel HJ and Oswald SE (2010), Dynamics of soil water content in the rhizosphere. *Plant and Soil* **332**: 163-176.

Carminati A, Schneider CL, Moradi AB, Zarebanadkouki M, Vetterlein D, Vogel HJ, Hildebrandt A, Weller U, Schuler L and Oswald SE (2011), How the Rhizosphere May Favor Water Availability to Roots. *Vadose Zone Journal* **10**: 988-998.

Carminati A, Vetterlein D, Koebernick N, Blaser S, Weller U and Vogel HJ (2013), Do roots mind the gap? *Plant and Soil* **367**: 651-661.

Carminati A (2013), Rhizosphere wettability decreases with root age: A problem or a strategy to increase water uptake of young roots? *Frontiers in Plant Science* **4**. doi:10.3389/fpls.2013.00298

Carminati A and Vetterlein D (2013), Plasticity of rhizosphere hydraulic properties as a key for efficient utilization of scarce resources. *Annals of Botany* **112**: 277-290.

Clausnitzer V and Hopmans JW (1994), Simultaneous modeling of transient three-dimensional root growth and soil water flow. *Plant and Soil* **164**: 299-314.

Cole PJ and Alston AM (1974), Effect of Transient Dehydration on Absorption of Chloride by Wheat Roots. *Plant and Soil* **40**: 243-247.

Couvreur V, Vanderborght J and Javaux M (2012), A simple three-dimensional macroscopic root water uptake model based on the hydraulic architecture approach. *Hydrology and Earth System Sciences* **16**: 2957-2971.

Couvreur V, Vanderborght J, Draye X and Javaux M (2014), Dynamic aspects of soil water availability for isohydric plants: Focus on root hydraulic resistances. *Water Resources Research* **50**: 8891-8906.

Donovan LA, Richards JH and Linton MJ (2003), Magnitude and Mechanisms of Disequilibrium between Predawn Plant and Soil Water Potentials. *Ecology* **84**: 463-470.

Doussan C, Pages L and Vercambre G. (1998a), Modelling of the hydraulic architecture of root systems: An integrated approach to water absorption - Model description. *Annals of Botany* **81**: 213-223.

Doussan C, Vercambre G and Pages L (1998b), Modelling of the hydraulic architecture of root systems: An integrated approach to water absorption - Distribution of axial and radial conductances in maize. *Annals of Botany* **81**: 225-232.

Doussan C, Pierret A, Garrigues E and Pages L (2006), Water uptake by plant roots: II - Modelling of water transfer in the soil root-system with explicit account of flow within the root system - Comparison with experiments. *Plant and Soil* **283**: 99-117.

Downie HF, Adu MO, Schmidt S, Otten W, Dupuy LX, White PJ and Valentine TA (2014), Challenges and opportunities for quantifying roots and rhizosphere interactions through imaging and image analysis. *Plant, Cell & Environment* **38**: 1213–1232.

Downie H, Holden N, Otten W, Spiers AJ, Valentine TA and Dupuy LX. (2012), Transparent Soil for Imaging the Rhizosphere. *PLoS ONE* **7**: e44276.

Draye X, Kim Y, Lobet G and Javaux M (2010), Model-assisted integration of physiological and environmental constraints affecting the dynamic and spatial patterns of root water uptake from soils. *Journal of Experimental Botany* **61**: 2145-2155.

Drew MC (1975), Comparison of the Effects of a Localized Supply of Phosphate, Nitrate, Ammonium and Potassium on the Growth of the Seminal Root System, and the Shoot, in Barley. *New Phytologist* **75**: 479-490.

Dunbabin VM, McDermott S and Bengough AG (2006), Upscaling from rhizosphere to whole root system: Modelling the effects of phospholipid surfactants on water and nutrient uptake. *Plant and Soil* **283**: 57-72.

Dunbabin V, Postma J, Schnepf A, Pagès L, Javaux M, Wu L, Leitner D, Chen Y, Rengel Z and Diggle A (2013), Modelling root-soil interactions using three-dimensional models of root growth, architecture and function. *Plant Soil* **372**: 93-124.

Durner W (1994), Hydraulic conductivity estimation for soils with heterogeneous pore structure. *Water Resources Research* **30**: 211-223.

Dutilleul P, Lontoc-Roy M and Prasher SO. (2005), Branching out with a CT scanner. *Trends in plant science* **10**: 411-412.

El Nadi AH, Brouwer R and Locher JT (1969), Some responses of the root and the shoot of Vicia faba plants to water stress. *Netherlands Journal of Agricultural Science* **17,** 133-142.

Enstone D, Peterson C and Ma F (2002), Root Endodermis and Exodermis: Structure, Function, and Responses to the Environment. *J Plant Growth Regul* **21**: 335-351.

Eshel A and Beeckman T (eds.) (2013), *Plant roots : the hidden half.* 4th ed., CRC Press, Boca Raton, 848 pp.

Faiz SMA and Weatherley PE (1982), Root contraction in transpiring plants. *New Phytologist* **92**: 333-343.

Fan M, Zhu J, Richards C, BROWN KM and Lynch JP (2003), Physiological roles for aerenchyma in phosphorus-stressed roots. *Functional Plant Biology* **30**: 493-506.

FAO (2009), The State of Food Insecurity in the World 2009. Economic crises – Impacts and lessons learned. *FAO*, Rome, 2009

FAO, WFP and IFAD (2012), The State of Food Insecurity in the World 2012. Economic growth is necessary but not sufficient to accelerate reduction of hunger and malnutrition. *FAO*, Rome, 2012.

Flavel RJ, Guppy CN, Tighe M, Watt M, McNeill A and Young IM (2012), Non-destructive quantification of cereal roots in soil using high-resolution X-ray tomography. *Journal of Experimental Botany* **63**: 2503-2511.

Foley JA, DeFries R, Asner GP, Barford C, Bonan G, Carpenter SR, Chapin FS, Coe MT, Daily GC, Gibbs HK, Helkowski JH, Holloway T, Howard EA, Kucharik CJ, Monfreda C, Patz JA, Prentice IC, Ramankutty N and Snyder PK (2005), Global Consequences of Land Use. *Science* **309**: 570-574.

Frensch J and Steudle E (1989), Axial and Radial Hydraulic Resistance to Roots of Maize (Zea mays L.). *Plant Physiology* **91**: 719-726.

Gardner WR (1960), Dynamic Aspects of Water Availability to Plants. *Soil Science* **89**: 63-73.

Garrigues E, Doussan C and Pierret A (2006), Water uptake by plant roots: I - Formation and propagation of a water extraction front in mature root systems as evidenced by 2D light transmission imaging. *Plant and Soil* **283**: 83-98.

Gradmann H (1928),Untersuchungen über die Wasserverhältnisse des Bodens als Grundlage des Pflanzenwachstums, *I. Jahrb.* Wiss. Bot. **69**, 1–100.

Green SR, Kirkham MB and Clothier BE (2006), Root uptake and transpiration: From measurements and models to sustainable irrigation. *Agricultural Water Management* **86**: 165-176.

Greenland DJ, Harley JL, and Scott-Russel R (1979), The physics and chemistry of the soil-root interface: some comments. In: *The Soil-Root Interface.* Harley JL and Scott-Russel R (eds.) Academic Press, London*, 83–89.*

Gregory PJ, Hutchison DJ, Read DB, Jenneson PM, Gilboy WB and Morton EJ (2003), Non-invasive imaging of roots with high resolution X-ray micro-tomography. In: *Roots: The Dynamic Interface between Plants and the Earth.* Abe J (ed.) Springer, Dordrecht, 351-359.

Hainsworth JM and Aylmore LAG (1986), Water Extraction by Single Plant-Roots. *Soil Science Society of America Journal* **50**: 841-848.

Hallett PD, Gordon DC and Bengough AG (2003), Plant influence on rhizosphere hydraulic properties: direct measurements using a miniaturized infiltrometer. *New Phytologist* **157**: 597-603.

Han L, Dutilleul P, Prasher SO, Beaulieu C and Smith DL (2008), Assessment of common scab-inducing pathogen effects on potato underground organs via computed tomography scanning. *Phytopathology* **98**: 1118-1125.

Hargreaves C, Gregory P and Bengough AG (2009), Measuring root traits in barley (Hordeum vulgare ssp. vulgare and ssp. spontaneum) seedlings using gel chambers, soil sacs and X-ray microtomography. *Plant and Soil* **316**: 285-297.

Heeraman DA, Hopmans JW and Clausnitzer V (1997), Three dimensional imaging of plant roots in situ with x-ray computed tomography. *Plant and Soil* **189**: 167-179.

Herkelrath WN, Miller EE and Gardner WR (1977a), Water-Uptake by Plants .1. Divided Root Experiments. *Soil Science Society of America Journal* **41**: 1033-1038.

Herkelrath WN, Miller EE and Gardner WR (1977b), Water-Uptake by Plants .2. Root Contact Model. *Soil Science Society of America Journal* **41**: 1039-1043.

Hillel, D (ed.) (1998), *Environmental Soil Physics.* Academic Press, New York, 771 pp

Hinckley TM and Bruckerhoff DN (1975), Effects of Drought on Water Relations and Stem Shrinkage of Quercus-Alba. *Canadian Journal of Botany-Revue Canadienne de Botanique* **53**: 62-72.

Hinsinger P, Bengough AG, Vetterlein D and Young I (2009), Rhizosphere: biophysics, biogeochemistry and ecological relevance. *Plant Soil* **321**: 117-152.

Hodge A, Berta G, Doussan C, Merchan F and Crespi M (2009), Plant root growth, architecture and function. *Plant Soil* **321**: 153-187.

Hsiao TC (1973), Plant responses to water stress. *Annual Review of Plant Physiology* **24**: 519-570.

Huber K, Vanderborght J, Javaux M, Schr+Âder N, Dodd I and Vereecken H (2014), Modelling the impact of heterogeneous rootzone water distribution on the regulation of transpiration by hormone transport and/or hydraulic pressures. *Plant and Soil* **384**: 93-112.

Huck MG, Klepper B and Taylor HM (1970), Diurnal Variations in Root Diameter. *Plant Physiology* **45**: 529-530.

Jassogne L. (2009), *Characterisation of porosity and root growth in a sodic texture-contrast soil,* PhD-Thesis. University of Western Australia. School of Plant Biology, Perth, Australia.

Javaux M, Schroder T, Vanderborght J and Vereecken H (2008), Use of a three-dimensional detailed modeling approach for predicting root water uptake. *Vadose Zone Journal* **7**: 1079-1088.

Javaux M, Couvreur V, Vanderborght J and Vereecken H (2013), Root Water Uptake: From Three-Dimensional Biophysical Processes to Macroscopic Modeling Approaches. **12**. doi:10.2136/vzj2013.02.0042

Javot H and Maurel CHRI (2002), The Role of Aquaporins in Root Water Uptake. *Annals of Botany* **90**: 301-313.

Jenneson PM, Gilboy WB, Morton EJ, Luggar RD, Gragory PJ and Hutchinson D (1999), Optimisation of X-ray micro-tomography for the in situ study of the development of plant roots. *IEEE Nuclear Science Symposium Conference Record* **1-3**, 429-432. doi: 10.1109/NSSMIC.1999.842521

Kaestner A, Schneebeli M and Graf F (2006), Visualizing three-dimensional root networks using computed tomography. *Geoderma* **136**: 459-469.

Keyes SD, Daly KR, Gostling NJ, Jones DL, Talboys P, Pinzer BR, Boardman R, Sinclair I, Marchant A and Roose T (2013), High resolution synchrotron imaging of wheat root hairs growing in soil and image based modelling of phosphate uptake. *New Phytologist* **198**: 1023-1029.

Kim H, Rao PS and Annable MD (1997), Determination of effective air-water interfacial area in partially saturated porous media using surfactant adsorption. *Water Resources Research* **33**: 2705-2711.

Knipfer T and Fricke W (2011), Water uptake by seminal and adventitious roots in relation to whole-plant water flow in barley (Hordeum vulgare L.). *Journal of Experimental Botany* **62**: 717-733.

Koebernick N, Weller U, Huber K, Schlüter S, Vogel HJ, Jahn R, Vereecken H and Vetterlein D (2014), In Situ Visualization and Quantification of Three-Dimensional Root System Architecture and Growth Using X-Ray Computed Tomography. *Vadose Zone Journal* **13**. doi:10.2136/vzj2014.03.0024

Kooistra MJ, Schoonderbeek D, Boone FR, Veen BW and Van Noordwijk M (1992), Root-Soil Contact of Maize, As Measured by A Thin-Section Technique .2. Effects of Soil Compaction. *Plant and Soil* **139**: 119-129.

Kutschera L, Lichtenegger E and Sobotik M (2009), *Wurzelatlas der Kulturpflanzen gemäßigter Gebiete mit Arten des Feldgemüsebaues.* DLG Verlag, Frankfurt am Main.

Landsberg JJ and Fowkes ND (1978), Water Movement Through Plant Roots. *Annals of Botany* **42**: 493-508.

Leitner D, Felderer B, Vontobel P and Schnepf A (2014), Recovering Root System Traits Using Image Analysis Exemplified by Two-Dimensional Neutron Radiography Images of Lupine. *Plant Physiology* **164**: 24-35.

Leitner D, Klepsch S, Bodner G and Schnepf A (2010a), A dynamic root system growth model based on L-Systems. *Plant and Soil* **332**: 177-192.

Leitner D, Klepsch S, Ptashnyk M, Marchant A, Kirk GJD, Schnepf A and Roose T (2010b), A dynamic model of nutrient uptake by root hairs. *New Phytologist* **185**: 792-802.

Lobet G, Pagès L and Draye X (2014), A modeling approach to determine the importance of dynamic regulation of plant hydraulic conductivities on the water uptake dynamics in the soil-plant-atmosphere system. *Ecological Modelling* **290**: 65-75.

Lontoc-Roy M, Dutilleul P, Prasher SO, Han L, Brouillet T and Smith DL (2006), Advances in the acquisition and analysis of CT scan data to isolate a crop root system from the soil medium and quantify root system complexity in 3-D space. *Geoderma* **137**: 231-241.

Lontoc-Roy M, Dutilleul P, Prasher SO, Han L and Smith DL (2005), Computed tomography scanning for three-dimensional imaging and complexity analysis of developing root systems. *Canadian Journal of Botany* **83**: 1434-1442.

Lynch JP (1995), Root Architecture and Plant Productivity. *Plant Physiology* **109**: 7-13.

Lynch JP, Nielsen KL, Davis RD ad Jablokow AG (1997), SimRoot: Modelling and visualization of root systems. *Plant and Soil* **188**: 139-151.

Lynch JP (2007), Turner review no. 14. Roots of the second green revolution. *Australian Journal of Botany* **55**: 493-512.

Mairhofer S, Zappala S, Tracy SR, Sturrock C, Bennett M, Mooney SJ and Pridmore T (2012), RooTrak: Automated Recovery of Three-Dimensional Plant Root Architecture in Soil from X-Ray Microcomputed Tomography Images Using Visual Tracking. *Plant Physiology* **158**: 561-569.

Mairhofer S, Zappala S, Tracy S, Sturrock C, Bennett M, Mooney S and Pridmore T (2013), Recovering complete plant root system architectures from soil via X-ray µ-Computed Tomography. *Plant Methods* **9**. doi:10.1186/1746-4811-9-8

Marschner P, Neumann G, Kania A, Weiskopf L and Lieberei R (2002), Spatial and temporal dynamics of the microbial community structure in the rhizosphere of cluster roots of white lupin (Lupinus albus L.). *Plant and Soil* **246**: 167-174.

McCully ME (1999), Roots in soil: unearthing the complexities of roots and their rhizospheres. *Annual Review of Plant Biology* **50**: 695-718.

McGinnis R (2002–2009), Rad Pro X-ray Device Dose-Rate Calculator Online. Massachusetts Institute of Technology.

McElrone AJ, Bichler JU, Pockman WT, Addington RN, Linder CR and Jackson RB (2007), Aquaporin-mediated changes in hydraulic conductivity of deep tree roots accessed via caves. *Plant, Cell & Environment* **30**: 1411-1421.

Metzner R, Eggert A, van Dusschoten D, Pflugfelder D, Gerth S, Schurr U, Uhlmann N and Jahnke S (2015), Direct comparison of MRI and X-ray CT technologies for 3D imaging of root systems in soil: potential and challenges for root trait quantification. *Plant Methods* **11**. doi:10.1186/s13007-015-0060-z

Mooney SJ, Pridmore TP, Helliwell J and Bennett MJ (2012), Developing X-ray Computed Tomography to non-invasively image 3-D root systems architecture in soil. *Plant and Soil* **352**: 1-22.

Moradi AB, Carminati A, Vetterlein D, Vontobel P, Lehmann E, Weller U, Hopmans JW, Vogel HJ and Oswald SE (2011), Three-dimensional visualization and quantification of water content in the rhizosphere. *New Phytologist* **192**: 653-663.

Neumann G, George TS and Plassard C (2009), Strategies and methods for studying the rhizosphere-the plant science toolbox. *Plant and Soil* **321**: 431-456.

Neumann RB and Cardon ZG (2012), The magnitude of hydraulic redistribution by plant roots: a review and synthesis of empirical and modeling studies. *New Phytologist* **194**: 337-352.

Newman EI (1969), Resistance to Water Flow in Soil and Plant .I. Soil Resistance in Relation to Amounts of Root - Theoretical Estimates. *Journal of Applied Ecology* **6**: 1-&.

North GB and Nobel PS (1997a), Root-soil contact for the desert succulent Agave deserti in wet and drying soil. *New Phytologist* **135**: 21-29.

North GB and Nobel PS (1997b), Drought-induced changes in soil contact and hydraulic conductivity for roots of Opuntia ficus-indica with and without rhizosheaths. *Plant and Soil* **191**: 249-258.

Nye PH (1994), The Effect of Root Shrinkage on Soil-Water Inflow. *Philosophical Transactions of the Royal Society of London Series B-Biological Sciences* **345**: 395-402.

Ohser J and Schladitz K (eds.) (2009), *3D Images of Materials Structures - Processing and Analysis*. Wiley VCH, Weinheim, 341 pp.

Oswald SE, Menon M, Carminati A, Vontobel P, Lehmann E and Schulin R (2008), Quantitative Imaging of Infiltration, Root Growth, and Root Water Uptake via Neutron Radiography. *Vadose Zone Journal* **7**: 1035-1047.

Pages L, Vercambre G, Drouet JL, Lecompte F, Collet C and Le Bot J (2004), Root Typ: a generic model to depict and analyse the root system architecture. *Plant and Soil* **258**: 103-119.

Passioura JB (1980), The Transport of Water from Soil to Shoot in Wheat Seedlings. *Journal of Experimental Botany* **31**: 333-345.

Peksen E (2007), Non-destructive leaf area estimation model for faba bean (Vicia faba L.). *Scientia Horticulturae* **113**: 322-328.

Perret JS, Al-Belushi ME and Deadman M (2007), Non-destructive visualization and quantification of roots using computed tomography. *Soil Biology & Biochemistry* **39**: 391-399.

Peters A and Durner W (2008), Simplified evaporation method for determining soil hydraulic properties. *Journal of Hydrology* **356**: 147-162.

Philip JR (1957), The physical principles of soil water movement during the irrigation cycle. *Proc Int Congr Comm Irrig Drain*. 8125-8154.

Pierret A, Capowiez Y, Belzunces L, and Moran CJ (2002), 3D reconstruction and quantification of macropores using X-ray computed tomography and image analysis. *Geoderma* **106**: 247-271.

Pierret A, Doussan C, Capowiez Y, Bastardie F and Pages L (2007), Root functional architecture: A framework for modeling the interplay between roots and soil. *Vadose Zone Journal* **6**: 269-281.

Pierret A, Kirby M and Moran C (2003), Simultaneous X-ray imaging of plant root growth and water uptake in thin-slab systems. *Plant and Soil* **255**: 361-373.

Pierret A, Capowiez Y, Moran CJ and Kretzschmar A (1999), X-ray computed tomography to quantify tree rooting spatial distributions. *Geoderma* **90**: 307-326.

Pierret A, Moran CJ and Doussan C (2005), Conventional detection methodology is limiting our ability to understand the roles and functions of fine roots. *New Phytologist* **166**: 967-980.

Pohlmeier A, Oros-Peusquens A, Javaux M, Menzel MI, Vanderborght J, Kaffanke J, Romanzetti S, Lindenmair J, Vereecken H and Shah NJ (2008), Changes in Soil Water Content Resulting from Ricinus Root Uptake Monitored by Magnetic Resonance Imaging. *Vadose Zone Journal* **7**: 1010-1017.

Pond RH (1908), Emergence of Lateral Roots. *Botanical Gazette* **46**: 410-421.

Pratt WK (ed.) (2007), *Digital Image Processing,* 4th ed. John Wiley & Sons, New York, 808 pp.

Pregitzer KS (2002), Fine Roots of Trees: A New Perspective. *New Phytologist* **154**: 267-270.

Röhmheld V and Marschner H (1990), Genotypical differences among graminaceous species in release of phytosiderophores and uptake of iron phytosiderophores. *Plant and Soil* **123**: 147-153.

Read DB, Bengough AG, Gregory PJ, Crawford JW, Robinson D, Scrimgeour CM, Young IM, Zhang K, and Zhang X (2003), Plant roots release phospholipid surfactants that modify the physical and chemical properties of soil. *New Phytologist* **157**: 315-326.

Richards LA (1931), Capillary conduction of liquids through porous mediums. *Physics-a Journal of General and Applied Physics* **1,** 318-333.

Rosin PL (2001), Unimodal thresholding. *Pattern recognition* **34**: 2083-2096.

Rudin LI, Osher S and Fatemi E (1992), Nonlinear Total Variation Based Noise Removal Algorithms. *Physica D* **60**: 259-268.

Schaap MG, Leij FJ and Van Genuchten MT (2001), ROSETTA: a computer program for estimating soil hydraulic parameters with hierarchical pedotransfer functions. *Journal of Hydrology* **251**: 163-176.

Schlüter S, Sheppard A, Brown K and Wildenschild D (2014), Image processing of multiphase images obtained via X-ray microtomography: A review. *Water Resources Research* **50**: 3615-3639.

Schladitz K, Redenbach C, Sych T and Godehardt M (2012), Model Based Estimation of Geometric Characteristics of Open Foams. *Methodol Comput Appl Probab* **14**: 1011-1032.

Schmidt S, Bengough AG, Gregory PJ, Grinev DV and Otten W (2012), Estimating root-soil contact from 3D X-ray microtomographs. *European Journal of Soil Science* **63**: 776-786.

Schnepf A, Leitner D and Klepsch S (2012), Modeling Phosphorus Uptake by a Growing and Exuding Root System. *Vadose Zone Journal* **11**.

Scholander PF, Bradstreet ED, Hemmingsen EA and Hammel HT (1965), Sap Pressure in Vascular Plants: Negative hydrostatic pressure can be measured in plants. *Science* **148**: 339-346.

Schröder N, Lazarovitch N, Vanderborght J, Vereecken H and Javaux M (2014), Linking transpiration reduction to rhizosphere salinity using a 3D coupled soil-plant model. *Plant and Soil* **377**: 277-293.

Schröder T, Javaux M, Vanderborght J, Körfgen B and Vereecken H (2009), Implementation of a Microscopic Soil-Root Hydraulic Conductivity Drop Function in a Three-Dimensional Soil-Root Architecture Water Transfer Model. *Vadose Zone J* 783-792.

Simunek J, Huang K and Van Genuchten MT (1995), The SWMS-3D code for simulating water flow and solute transport in three-dimensional variably-saturated media. US Salinity Laboratory. *Agricultural Research Service, US Department of Agriculture, Riverside, California.*

Smit AL, Bengough AG, Engels C, Noordwijk Mv, Pellerin S and Geijn S (eds.) (2000), *Root methods: A handbook.*Springer-Verlag, Berlin, 567 pp.

Somma F, Hopmans JW and Clausnitzer V (1998), Transient three-dimensional modeling of soil water and solute transport with simultaneous root growth, root water and nutrient uptake. *Plant and Soil* **202**: 281-293.

Steudle E (2000), Water uptake by plant roots: an integration of views. *Plant and Soil* **226**: 45-56.

Stingaciu L, Schulz H, Pohlmeier A, Behnke S, Zilken H, Javaux M and Vereecken H (2013), In Situ Root System Architecture Extraction from Magnetic Resonance Imaging for Water Uptake Modeling. *Vadose Zone Journal* **12**. doi:10.2136/vzj2012.0019

Tardieu F (1988), Analysis of the Spatial Variability of Maize Root Density .2. Distances Between Roots. *Plant and Soil* **107**: 267-272.

Taylor HM, Roberson GM and Parker JJJ (1966), Soil strength-root penetration relations for medium- to coarse-textured soil materials. *Soil Science* **102**: 18-22.

Tilman D, Balzer C, Hill J and Befort BL (2011), Global food demand and the sustainable intensification of agriculture. *Proceedings of the National Academy of Sciences* **108**: 20260-20264.

Tinker PB (1976), Transport of Water to Plant Roots in Soil. *Philosophical Transactions of the Royal Society of London B: Biological Sciences* **273**: 445-461.

Tracy SR, Black CR, Roberts JA, Sturrock C, Mairhofer S, Craigon J and Mooney SJ (2012), Quantifying the impact of soil compaction on root system architecture in tomato (Solanum lycopersicum) by X-ray micro-computed tomography. *Annals of Botany* **110**: 511-519.

Tracy SR, Daly KR, Sturrock CJ, Crout NMJ, Mooney SJ and Roose T (2015), Three-dimensional quantification of soil hydraulic properties using X-ray Computed Tomography and image-based modeling. *Water Resources Research* **51**: 1006-1022.

Tracy SR, Roberts JA, Black CR, McNeill A, Davidson R and Mooney SJ (2010), The X-factor: visualizing undisturbed root architecture in soils using X-ray computed tomography. *Journal of Experimental Botany* **61**: 311-313.

van den Honert TH (1948), Water transport in plants as a catenary process. *Discussions of the Faraday Society* **3**: 146-153.

Van Genuchten MT (1980), A Closed-Form Equation for Predicting the Hydraulic Conductivity of Unsaturated Soils. *Soil Science Society of America Journal* **44**: 892-898.

Van Noordwijk M, Brouwer G and Harmanny K (1993), Concepts and Methods for Studying Interactions of Roots and Soil Structure .47. *Geoderma* **56**: 351-375.

Van Noordwijk M, Kooistra MJ, Boone FR, Veen BW and Schoonderbeek D (1992), Root-soil contact of maize, as measured by a thin-section technique. *Plant and Soil* **139**: 109-118.

Veen BW, Van Noordwijk M, De Willigen P, Boone FR and Kooistra MJ (1992), Root-soil contact of maize, as measured by a thin-section technique. *Plant and Soil* **139**: 131-138.

Vetterlein D, Marschner H and Horn R (1993), Microtensiometer Technique for Insitu Measurement of Soil Matric Potential and Root Water Extraction from A Sandy Soil. *Plant and Soil* **149**: 263-273.

Vetterlein D, Szegedi K, Ackermann J, Mattusch J, Neue HU, Tanneberg H and Jahn R (2007), Competitive Mobilization of Phosphate and Arsenate Associated with Goethite by Root Activity. *Journal of Environmental Quality* **36**: 1811-1820.

Vogel HJ, Weller U and Schlüter S (2010), Quantification of soil structure based on Minkowski functions. *Computers & Geosciences* **36**: 1236-1245.

Vollsnes AV, Futsaether CM and Bengough AG (2010), Quantifying rhizosphere particle movement around mutant maize roots using time-lapse imaging and particle image velocimetry. *European Journal of Soil Science* **61**: 926-939.

White PJ, George TS, Gregory PJ, Bengough AG, Hallett PD and McKenzie BM (2013), Matching roots to their environment. *Annals of Botany* **112**: 207-222.

Willmer CM, Wilson AB and Jones HG (1988), Changing Responses of Stomata to Abscisic Acid and CO2 as Leaves and Plants Age. *Journal of Experimental Botany* **39**: 401-410.

Zappala S, Helliwell JR, Tracy SR, Mairhofer S, Sturrock CJ, Pridmore T, Bennett M and Mooney SJ (2013a), Effects of X-Ray Dose On Rhizosphere Studies Using X-Ray Computed Tomography. *PLoS ONE* **8**. doi: 10.1371/journal.pone.0067250

Zappala S, Mairhofer S, Tracy S, Sturrock C, Bennett M, Pridmore T and Mooney S (2013b), Quantifying the effect of soil moisture content on segmenting root system architecture in X-ray computed tomography images. *Plant and Soil* **370**: 35-45.

Zarebanadkouki M, Kim YX and Carminati A (2013), Where do roots take up water? Neutron radiography of water flow into the roots of transpiring plants growing in soil. *New Phytologist* **199**: 1034-1044.

Zarebanadkouki M, Kim YX, Moradi AB, Vogel HJ, Kaestner A and Carminati A (2012), Quantification and Modeling of Local Root Water Uptake Using Neutron Radiography and Deuterated Water. *Vadose Zone Journal* **11**. doi:10.2136/vzj2011.0196

Zhuang J, Yu GR and Nakayama K (2014), A Series RCL Circuit Theory for Analyzing Non-Steady-State Water Uptake of Maize Plants. *Sci Rep* **4**. doi:10.1038/srep06720

Zwieniecki MA, Thompson MV and Holbrook NM (2002), Understanding the hydraulics of porous pipes: Tradeoffs between water uptake and root length utilization. *Journal of Plant Growth Regulation* **21**: 315-323.

9   List of Abbreviations

1D	one-dimensional
2D	two-dimensional
3D	three-dimensional
ABA	abscisic acid
CAM	crassulacean acid metabolism
CT	computed tomography / Computertomographie
DAP	days after planting
h	height
HMD	half mean distance
K^*_r	radial root hydraulic conductivity
K_{root}	equivalent hydraulic conductivity of the root system
K^*_x	axial root hydraulic conductance
L.	botanical author citation of Carl Linnaeus
MF	Minkowski functional
MRI	magnetic resonance imaging
P	probability of obtaining a test statistic
θ	soil water content / soil moisture content
ρ	root-soil contact
RSA	root system architecture
RWU	root water uptake
SUF	standard uptake fraction
T_{air}	threshold for the segmentation of the air phase
T_{root}	threshold for the segmentation of the root phase
WA	Wurzelarchitektur
ψ_{collar}	water potential at the root collar
ψ_m	soil matric potential
ψ_{pd}	pre-dawn water potential
$\psi_{s,eff}$	effective soil water potential
Z	atomic number
Ø	diameter

Variables and constants in equations are explained below the equations.

10   List of Figures

118

11   List of Tables

120

Danksagung

Hier steht zwar mein Name als Autor – aber so viele Menschen haben zu der Arbeit beigetragen, sei es durch Ideen und Diskussionen, Hilfe im Labor, ein offenes Ohr und Hilfsbereitschaft bei meinen zahlreichen Fragen. Freunden und Familie danke ich für ihr schlichtes aber unverzichtbares Dasein. Nicht alle können hier erwähnt werden.

Zuallererst möchte ich mich bei meiner Betreuerin Doris Vetterlein dafür bedanken, dass sie mich in ihre Gruppe aufgenommen hat und mir ihre Begeisterung für dieses spannende Thema vermitteln konnte. Danke für all die Diskussionen und die stetige Ermutigung, am Ball zu bleiben. Doris, danke, dass Du mir gezeigt hast, dass wissenschaftliches Arbeiten Sorgfalt bei Methoden und Begrifflichkeiten voraussetzt, und dass Du mir das Vertrauen zur eigenständigen Entwicklung von Fragestellungen und ihrer Bearbeitung entgegengebracht hast.

Andrea Carminati danke ich für seine Bereitschaft, als Zweitgutachter zur Verfügung zu stehen und für die immer leidenschaftlichen und erhellenden Diskussionen auf Tagungen und Workshops. Grazie, capo!

Reinhold Jahn gilt mein Dank, da er zunächst mein „offizieller" Betreuer war und mir immer unkompliziert die Hürden der Bürokratie zu meistern half.

Ich danke allen Koautoren meiner Papers für ihre Hilfe, gute Ideen und konstruktive Kritik.

Ulrich Weller, Steffen Schlüter und Hans-Jörg Vogel danke ich dafür, dass sie mir ihr schier unendliches Wissen über CT und Bildbearbeitung weitergegeben haben.

Katrin Huber, Mathieu Javaux und Jan Vanderborght danke ich für die Zusammenarbeit und die Einführung in die Welt der Modelle. Besonders Katrin für das gemeinsame Design und Auswertung der Simulationen, geteilte Ratlosigkeit und Aha-Momente. Jan danke ich für die Aufnahme in seine Gruppe während meines Gastaufenthaltes in Jülich.

Die Kickerpausen mit Sebastian, Olli, Björn, Steffen und Ulf (Stulf) waren der Work-Life-Balance sehr zuträglich. Sabine danke ich dafür, dass sie mir die Stelle vermittelt hat! Claudia danke für die Hilfe im Labor und Bestellungen, und für ihr offenes Ohr.

Den vielen hier unerwähnten Kollegen und Freunden vom UFZ danke ich für die tolle Arbeitsatmosphäre und ihre Hilfsbereitschaft.

Wurzeln waren das Thema dieser Arbeit. Meine eigenen Wurzeln sollen nicht unerwähnt bleiben: Papa, Mama, Ihr habt immer zu mir gehalten und mir das Studium und die Dissertation ermöglicht. Ich danke Euch für alles.
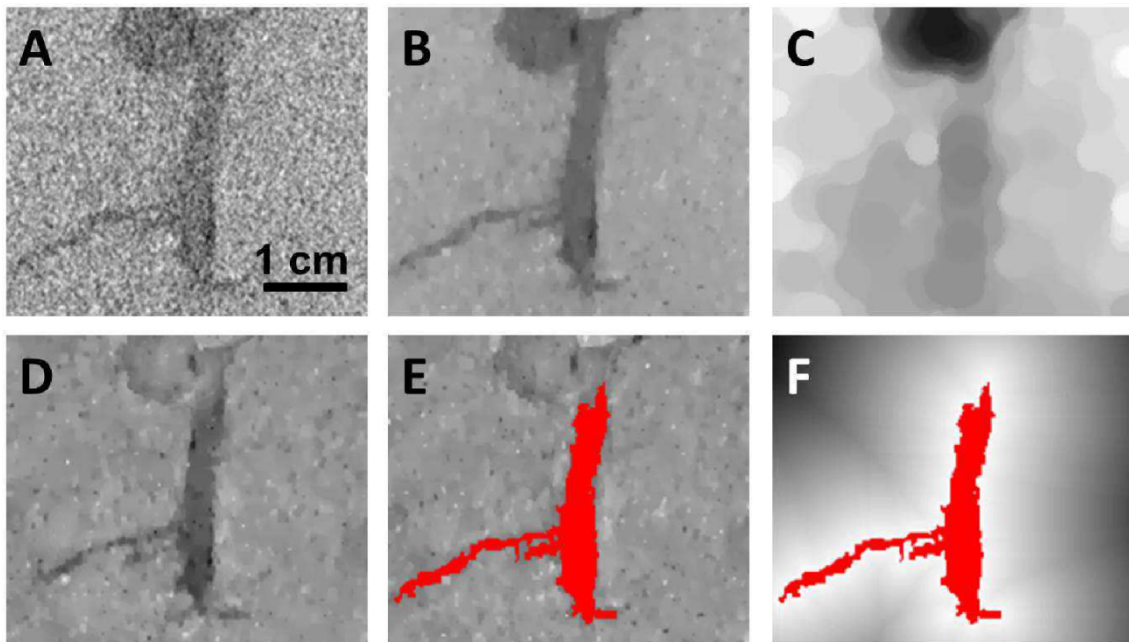
Figure A1.1: Detail of a vertical cross section of the tomographic image at 22 DAP showing different image processing steps. The base of the taproot, the seed, and three lateral roots are visible. A) raw image B) result of the total variation filter C) result of the pseudomedian filter D) difference image of C and B used for region growing E) segmented root after region growing F) distance transform, gray value decreases with distance from root surface
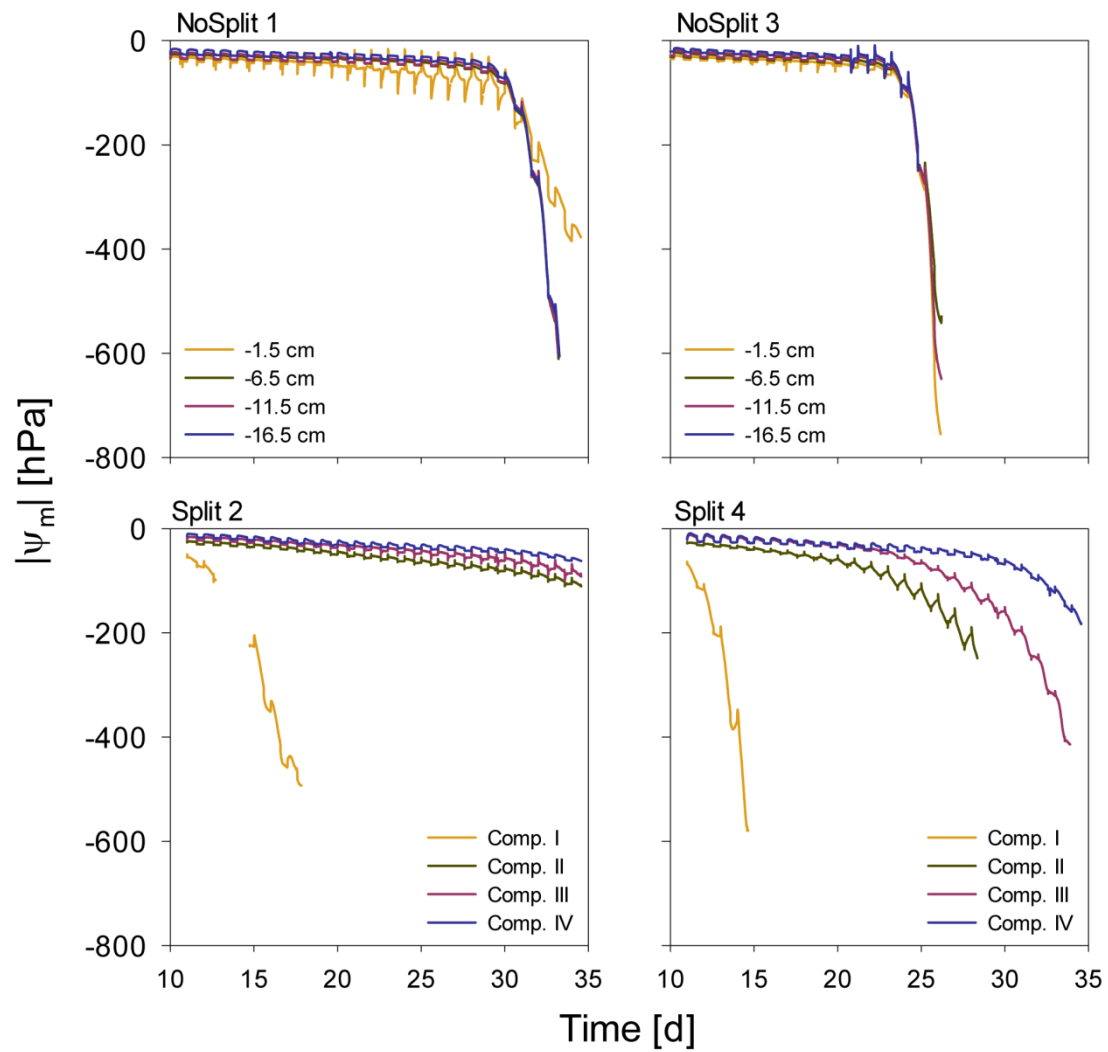
Figure A2.1: Development of soil matric potential ψ_m *over time of the samples not used for modeling. Different colors represent measurements in different depths / compartments*
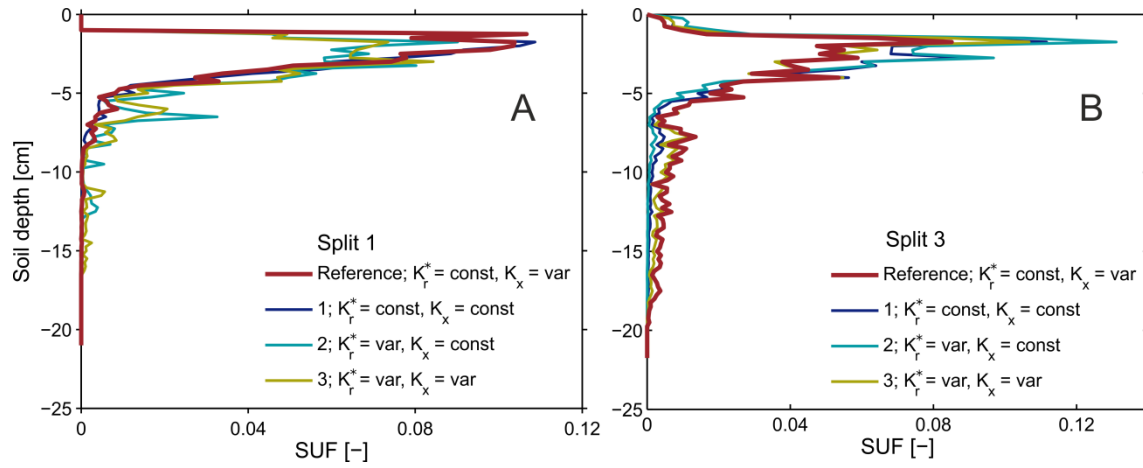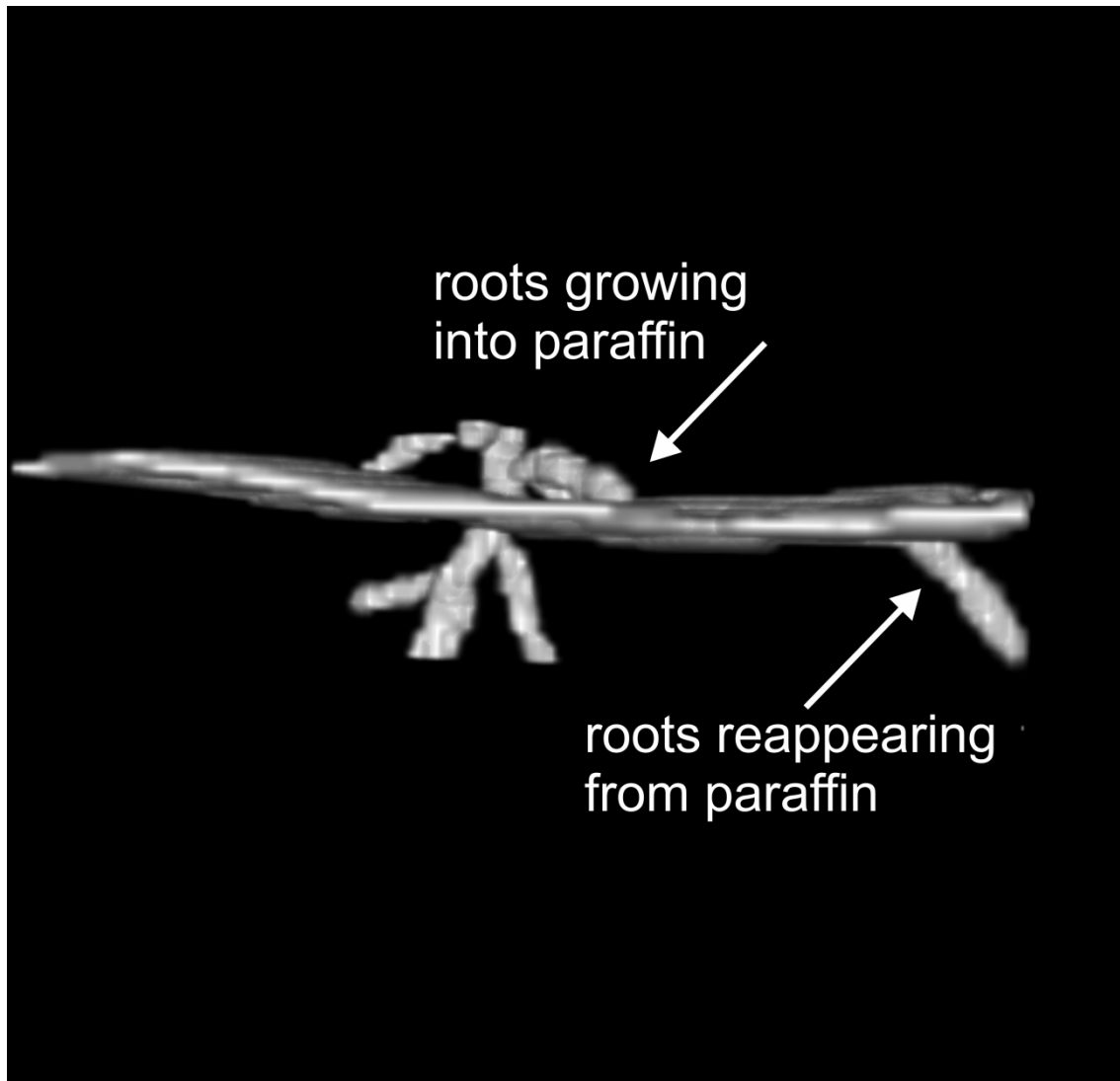
Figure A2.2: Sums of the standard uptake fraction over soil depth increments of 0.25 cm for (A) the Split 1 root system at t = 30 days and (B) the Split 3 root system at t = 34 days solved for different parameterizations of radial and axial root hydraulic conductivities

Figure A2.3: Influence of paraffin layer on root growth: roots grow either unimpeded (left), but can also be deflected within the soft paraffin and later re-penetrate the soil. Split 1, Day 12, Layer at -5 cm, Height of image section: 13.5 mm
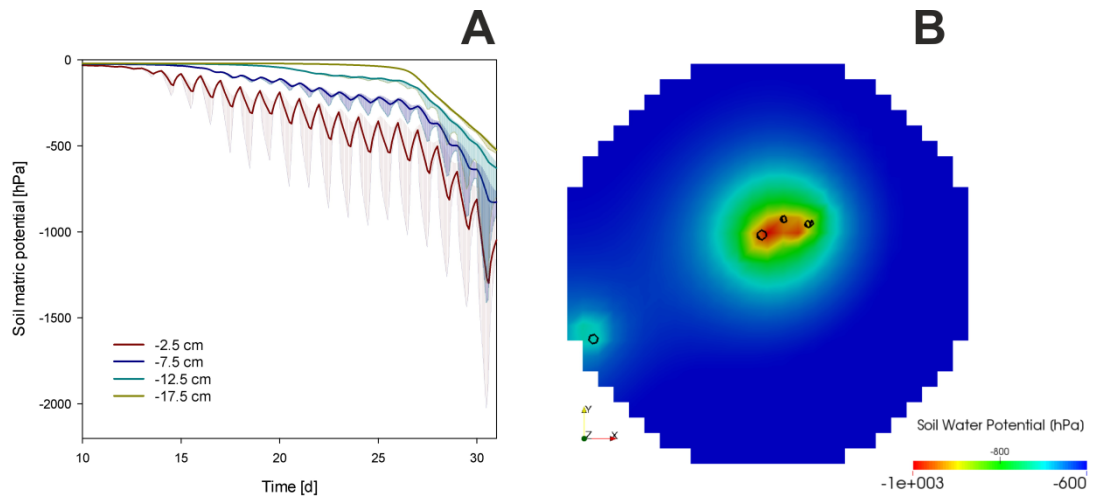
Figure A2.4: Split 1 scenario SC: A) line shows the mean and shaded areas the range (min - max) of soil water potential within each of the four soil compartments, B) single slice at z=-12 cm showing gradients of soil water potential around the roots (black circles)

Publikationsliste / *List of Publications*

Andrea Carminati, Doris Vetterlein, Nicolai Koebernick, Sebastian Blaser, Ulrich Weller and Hans-Jörg Vogel (2013). Do roots mind the gap? *Plant and Soil* **367**: 651-661.

Nicolai Koebernick, Ulrich Weller, Katrin Huber, Steffen Schlüter, Hans-Jörg Vogel, Reinhold Jahn, Harry Vereecken and Doris Vetterlein (2014). In situ visualization and quantification of 3D root system architecture and growth using X-ray CT. *Vadose Zone Journal* **13**, doi:10.2136/vzj2014.03.0024

Nicolai Koebernick, Katrin Huber, Elien Kerkhofs, Jan Vanderborght, Mathieu Javaux, Harry Vereecken and Doris Vetterlein (2015). Unraveling the hydrodynamics of split root water uptake experiments using CT scanned root architectures and three dimensional flow simulations. *Frontiers in Plant Science* **6**, doi: doi:10.3389/fpls.2015.00370

Lebenslauf / *Curriculum vitae*

Name	Nicolai Paul Koebernick
geboren am	25.09.1978 in Wuppertal
Staatsangehörigkeit	deutsch
Eltern	Helga Koebernick, geb. Lettau
	Wolfgang Koebernick

Schulausbildung

10/1985 – 07/1989	GGS Birkenhöhe, Wuppertal
08/1989 – 07/1998	Gymnasium Bayreuther Straße, Wuppertal
09.06.1998	Allgemeine Hochschulreife, Note 2,4

Zivildienst

09/1998 – 10/1999	Individuelle Schwerstbehindertenbetreuung beim Verein zur Betreuung und Integration von Senioren und behinderten Menschen e.V., Wuppertal

Studium

10/1999 – 03/2001	Studium der Biologie an der Georg-August-Universität Göttingen
18.10.2001	Diplom-Vorprüfung, Note: „gut"
10/2001 – 07/2002	Studium der Biologie an der Université Aix-Marseille
10/2002 – 02/2007	Studium der Biologie an der Universität Leipzig
	Thema der Diplomarbeit: „Aspekte des Wasserhaushaltes epiphytischer Orchideen und Farne im Nationalpark Yanachaga-Chemillén, Peru", Note: „sehr gut" (1,3)
02.01.2007	Diplom, Note: „gut" (1,8)

Berufstätigkeit

09/2008 – 02/2009	Praktikum bei PRODA - Programa de Desarollo Agroalimentario, Neuquén, Argentinien

Promotionsstudium

01.03.2010	Beginn der Dissertation am Institut für Agrar- und Ernährungswissenschaften
	Unter der Betreuung von Prof. Dr. Doris Vetterlein

Halle (Saale), den 24.6.2015

Nicolai Koebernick

Eidesstattliche Erklärung / *Declaration under oath*

Ich erkläre an Eides statt, dass ich die Arbeit selbständig und ohne fremde Hilfe verfasst, keine anderen als die von mir angegebenen Quellen und Hilfsmittel benutzt und die den benutzten Werken wörtlich oder inhaltlich entnommenen Stellen als solche kenntlich gemacht habe.

I declare under penalty of perjury that this thesis is my own work entirely and has been written without any help from other people. I used only the sources mentioned and included all the citations correctly both in word and content.

Halle (Saale), den 24.6.2015

Nicolai Koebernick